

# Accelerator Based Magnetic Monopole Search Experiments (Overview)

Vasily Dzhordzhadze, Praveen Chaudhari\*, Peter Cameron, Nicholas D'Imperio, Veljko Radeka, Pavel Rehak, Margareta Rehak, Sergio Rescia, Yannis Semertzidis, John Sondericker, and Peter Thieberger.

Brookhaven National Laboratory

## **ABSTRACT**

We present an overview of accelerator-based searches for magnetic monopoles and we show why such searches are important for modern particle physics. Possible properties of monopoles are reviewed as well as experimental methods used in the search for them at accelerators. Two types of experimental methods, direct and indirect are discussed. Finally, we describe proposed magnetic monopole search experiments at RHIC and LHC.

## Content

1. Magnetic Monopole characteristics
2. Experimental techniques
3. Monopole Search experiments
4. Magnetic Monopoles in virtual processes
5. Future experiments
6. Summary

1. Magnetic Monopole characteristics

The magnetic monopole puzzle remains one of the fundamental and unsolved problems in physics. This problem has a long history. The military engineer Pierre de Maricourt [1] in 1269 was breaking magnets, trying to separate their poles. P. Curie assumed the existence of single magnetic poles [2]. A real breakthrough happened after P. Dirac's approach to the solution of the electron charge quantization problem [3]. Before Dirac, J. Maxwell postulated his fundamental laws of electrodynamics [4], which represent a complete description of all known classical electromagnetic phenomena. Together with the Lorentz force law and the Newton equations of motion, they describe all the classical dynamics of interacting charged particles and electromagnetic fields. In analogy to electrostatics one can add a magnetic charge, by introducing a magnetic charge density, thus magnetic fields are no longer due solely to the motion of an electric charge and in Maxwell equation a magnetic current will appear in analogy to the electric current. The complete set of symmetrized Maxwell equations will have the form:

---

\* Spokesperson

$$\begin{aligned}\vec{\nabla} \cdot \vec{D} &= \rho_e \\ \vec{\nabla} \cdot \vec{B} &= \rho_m \\ -\vec{\nabla} \times \vec{E} &= \frac{\partial}{\partial t} \vec{B} + \vec{j}_m \\ \vec{\nabla} \times \vec{H} &= \frac{\partial}{\partial t} \vec{D} + \vec{j}_e\end{aligned}$$

where indices m and e label electric and magnetic quantities. These modification of the Maxwell equations do not necessarily imply physics beyond the standard electrodynamics, because symmetrized Maxwell equations are invariant under a duality transformation ( $\xi \in \mathbb{R}$ ):

$$\begin{aligned}\vec{E} &= \vec{E}' \cos \xi + \vec{H}' \sin \xi & \vec{D} &= \vec{D}' \cos \xi + \vec{B}' \sin \xi \\ \vec{H} &= -\vec{E}' \sin \xi + \vec{H}' \cos \xi & \vec{B} &= -\vec{D}' \sin \xi + \vec{B}' \cos \xi \\ \rho_e &= \rho'_e \cos \xi + \rho'_m \sin \xi & \vec{j}_e &= \vec{j}'_e \cos \xi + \vec{j}'_m \sin \xi \\ \rho_m &= -\rho'_e \sin \xi + \rho'_m \cos \xi & \vec{j}_m &= -\vec{j}'_e \sin \xi + \vec{j}'_m \cos \xi.\end{aligned}$$

The original Maxwell equations are recovered if all particles have the same ratio of magnetic charge to electric charge, which can be set to zero by the appropriate choice of the angle  $\xi$ . A special case which is useful for the duality transformations is when  $\xi = \pi/2$ . The extended Maxwell equations are invariant under the transformation:

$$\begin{aligned}\rho_e &\rightarrow \rho_m & \vec{j}_e &\rightarrow \vec{j}_m & \vec{E} &\rightarrow \vec{H} & \vec{D} &\rightarrow \vec{B} \\ \rho_m &\rightarrow -\rho_e & \vec{j}_m &\rightarrow -\vec{j}_e & \vec{B} &\rightarrow -\vec{D} & \vec{H} &\rightarrow -\vec{E}\end{aligned}$$

which switches electric and magnetic quantities. The extended Maxwell equations can be used to derive monopole versions of formulas, which are familiar from standard classical electrodynamics. The symmetry suggests a generalized Lorentz force for a particle with electric charge  $e$  and magnetic charge  $g$ :

$$\vec{F} = e \left( \vec{E} + \vec{v} \times \vec{B} \right) + g \left( \vec{B} - \vec{v} \times \vec{E} \right)$$

The symmetries of  $\rho_m$  under both spatial inversion and time reversal are opposite of those of  $\rho_e$ . As a consequence, if dyons, particles with both electric and magnetic charge exists, then space inversion and time reversal are no longer valid symmetries. Symmetry always played a key role in physics and it is therefore a motivation for “inventing” the magnetic charge.

In 1909, Robert Milliken discovered the quantization of electric charge by carrying out his famous oil drop experiment. Today the experimental accuracy of the electric charge quantization is [5]:  $|Q_{e^+} + Q_{e^-}|/e < 4 \times 10^{-8}$ ,  $|Q_{p^+} + Q_{p^-}|/e < 1 \times 10^{-8}$  and  $|Q_{p^+} + Q_{e^-}|/e < 1 \times 10^{-21}$ . This fact of

electric charge quantization remains mysterious even today. Its explanation is one of the nature's best kept secrets. In 1931, P. Dirac proposed that particles carrying a magnetic charge, or magnetic monopoles should exist. Dirac showed that the phase unobservability in quantum mechanics, permitted singularities, which manifest themselves as a sources of magnetic fields, just as point electric monopoles were sources of electric fields. This was only possible if the product of electric and magnetic charges is quantized. Dirac established the basic relation between the elementary electric charge  $e$  and basic magnetic charge  $g$ :

$$eg = n\hbar c/2, \text{ where } n = \pm 1, \pm 2, \pm 3, \dots$$

From this equation it follows that the magnetic charge

$$g = n\hbar c/2e = ne/2\alpha = (137/2) ne = 68.5en = g_D n, \quad g_D = 68.5e, \quad |n| = 1, 2, 3, \dots$$

The minimum value of the quantization number is  $n = 1$  according to Dirac or  $n = 2$  according to Schwinger [6]. However, if quarks charge are considered as elementary electric charge, then this magnitude become  $n = 3, 6$  respectively. Within this approach, for  $n = 1$  and the basic electron charge of the electron, the theoretical minimum magnetic charge is  $g_D = 68.5e$ , which is known as a Dirac magnetic charge. It is assumed that magnetic charge, like electric charge, is absolutely conserved, so the lightest magnetically charged particle is stable, unless annihilated by its antiparticle and magnetic monopoles are always produced in pairs, monopole and antimonopole. The quantization of electric charge in nature is well established fact, but it remains still mysterious. The discovery of just a single monopole will explain the quantization of electric charge. At the same time, as we mentioned above, the existence of magnetic charge and magnetic current will make Maxwell's equations symmetric, which is not forbidden by any known principles of physics. We should admit, that this symmetry is not exact, because of differences of electric and magnetic charges.

The coupling constant, related to the magnetic monopole interaction is

$$g^2/\hbar c = e^2/\hbar c [g/e]^2 = 1/137 [137/2]^2 = 34.25 .$$

For a minimal magnetic charge, this value is  $\gg 1$ . This means that theoretical consideration of magnetic monopoles has serious difficulties. We will discuss this problem in more detail in chapter 5.

The possible existence of magnetic monopoles received a strong boost in 1974 in works of t'Hooft and Polyakov [7,8] related to the Grand Unification Theories (GUT). They independently discovered monopole solutions in the SO(3) Georgi-Glashow model. It was demonstrated that any scheme of Grand Unification with an electromagnetic U(1) subgroup embedded into a semi-simple gauge-group, which becomes spontaneously broken by the Higgs mechanism, possessed a monopole solution. The monopole's mass  $m_M$  of standard GUT is related to the mass of the carriers X, Y of the unified interactions:  $m_M \geq m_X/G$ , where G is the dimensionless coupling constant at energies  $E \approx m_X$ . In GUTs with  $m_X \approx 10^{14} - 10^{15}$  GeV and  $G \approx 0.025$ ,  $m_M \geq 10^{16} - 10^{17}$  GeV. This is a very big mass and can never be produced at any man-made accelerators existing or future. They could only have been produced in the first moments of the Universe creation and should be searched for in the penetrating cosmic radiation. The most recent search for GUT monopoles in the cosmic radiation was performed by the MACRO detector, which uses three type of detectors (liquid scintillators, limited streamer tubes and nuclear track detectors).

At the same time some authors showed [9, 10], that the unification scale can be significantly lowered (even to the TeV scale) through the appearance of the extra dimensions. This means that magnetic monopoles can be searched for at modern future accelerators like LHC and

ILC. For the mass prediction of the magnetic monopoles there exists other estimation, based on equality of classical radii of electron and magnetic monopoles  $r_e = e^2/m_e c^2 = r_M = g^2/m_M c^2$  and  $m_M = 2.4 \text{ GeV}/c^2$ . In addition to the monopole masses we considered above, there are superstring model related magnetic monopoles [11], masses of which are predicted at the 1 TeV level. The Table 1 below shows expected magnetic monopole masses in different theoretical models and assumptions.

Table 1. Magnetic monopole mass prediction in different theoretical models.

Theory	Mass GeV	Reference
e radius	= 2.4	12
Electroweak	$50 - 10^4$	9, 10
Super String	$\sim 10^3$	11
GUT	$10^{16} - 10^{17}$	7, 8, 12

In conclusion, Dirac predicted only electromagnetic properties of the magnetic monopoles but not physical properties, thus any mass region for magnetic monopoles remains open. Dirac's idea of explanation of the electron charge quantization via monopole remains a most attractive concept and stimulates further experimental searches for the magnetic monopoles.

Considering experiments to search for magnetic monopoles it is important to notice how they behave in a magnetic field. In contrast to ordinary charged particles, which spiral in a solenoid and moving in the  $r-\phi$  plane, magnetic monopoles move along parabola-shaped curves in the  $r-z$  plane. Moving in a magnetic field, monopoles are gain an energy:  $W = ng_D B l$ , where  $ng_D$  is the monopole charge,  $B$  is the magnetic field and  $l$  is a length of the magnet. In modern experimental magnets monopoles can be easily accelerated by many GeV since the energy gain for a minimum charge monopoles is  $\sim 20 \text{ GeV/Tm}$ .

The behavior of the magnetic monopoles, when moving inside a material depends on the velocity  $\beta$  of the monopole. For slow monopoles ( $10^{-4} < \beta < 10^{-2}$ ) it is important to distinguish the energy loss to ionization or excitation of atoms and molecules of the medium ("electronic" energy loss) from the loss to yield kinetic energy of recoiling atoms or nuclei ("atomic" or "nuclear" energy loss). Electronic energy loss dominates for both electrically or magnetically charged particles with  $\beta > 10^{-3}$ . The energy loss with  $10^{-4} < \beta < 10^{-3}$  is dominated by the excitation of atoms. In ionization detectors, using noble gases there would be an additional energy loss due to atomic energy level mixing (Drell effect). For a fast moving monopole with a charge of  $g_D$  and velocity  $v = \beta c$ , the behavior in the material is equivalent to the behavior of a charged particle with an effective charge of  $(ze)_{eq} = g_D \beta$ . This means that energy losses of magnetic monopoles are very large.

## 2. Experimental techniques

Detectors used in magnetic monopole search experiments are based either on induction or on ionization. The induction method is based on the long-range electromagnetic interaction between the magnetic charge and the macroscopic quantum state of a superconducting loop. A Magnetic monopole, moving through the loop, induces an electromotive force and a current ( $\Delta i$ ). If the coil has  $N$  turns and its inductivity is  $L$ , the current is  $\Delta i = 4\pi N g_D / L = 2 \Delta \phi$ , where  $\Delta \phi$  is the current change corresponding to a change of one unit of the flux quantum of superconductivity. A

superconducting induction detector consists of the detection coil, which is coupled to a SQUID (Superconducting Quantum Interference Device). If magnetic monopole passes through a superconducting loop there will be a magnetic flux change of  $\phi_B = 2\pi\hbar c/e$ , which is independent of the monopole velocity. This type of detector is sensitive to any type of magnetic monopole and to any velocity of the magnetic monopole.

Ionization detectors used for magnetic monopole detection use the excitation loss technique. A Magnetic Monopole moving with a velocity of  $\beta \sim 10^{-4}$  in the scintillating material will cause a signal, which is higher than a signal from the minimum ionizing particle. For velocities  $10^{-3} < \beta < 10^{-1}$ , there is a saturation effect and for  $\beta > 10^{-1}$ , the light yield increases because of the production of many  $\delta$  rays.

The figure 1 shows the energy losses of a magnetic monopole with a charge  $g_D$  versus its velocity  $\beta$  [12] in liquid hydrogen. Curve a) corresponds to elastic monopole-hydrogen atom scattering; curve b) corresponds to interactions with level crossing and curve c) describes the ionization energy loss.

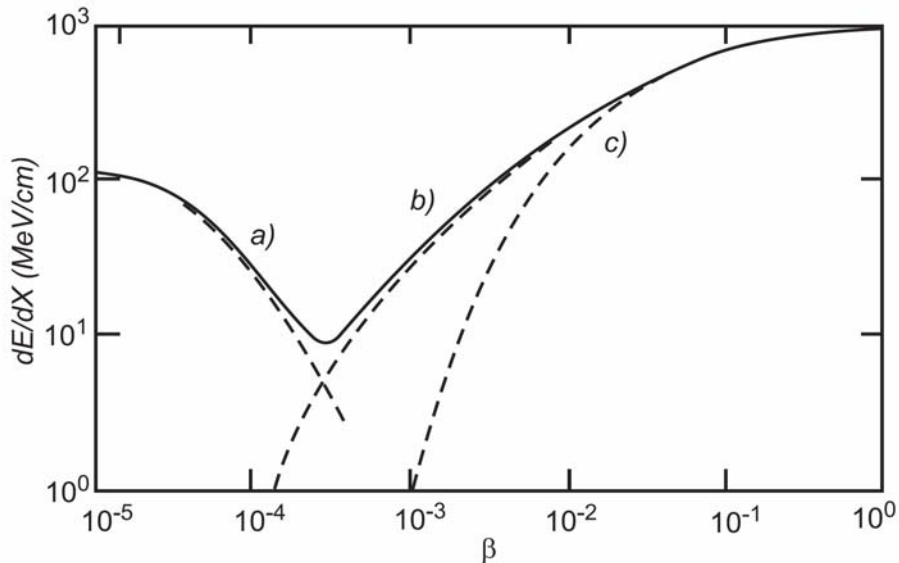


Figure 1. The energy loss of a magnetic monopole with a magnetic charge  $g = g_D$  in liquid hydrogen as a function of  $\beta$  [12].

Next figure 2 compares energy losses of proton and monopole at relatively high  $\beta$  values in air.

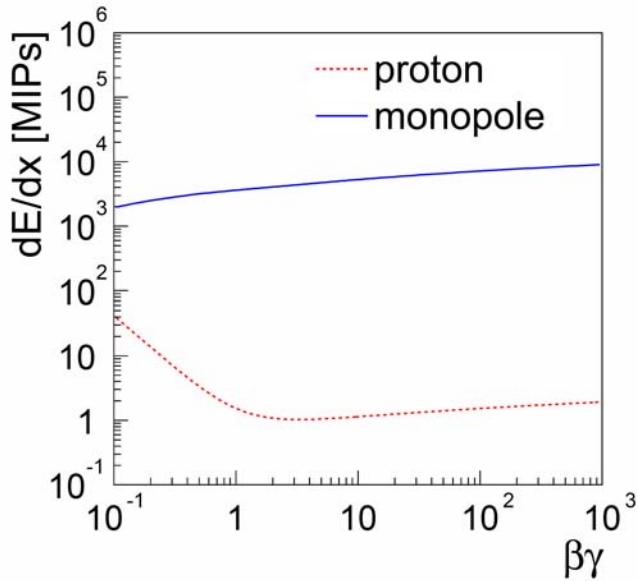


Figure 2. The energy loss of monopoles and protons in air [34a].

The figure shows that the magnetic monopole energy losses are higher than for protons by many orders of magnitude. Thus different materials like emulsions, scintillation counters, gaseous detectors and any other detectors, where  $dE/dx$  measurements are possible, can be used as monopole detectors.

The next type of magnetic monopole detection systems are a Nuclear Track Detectors (NTD) [13]. The NTDs are able to record the passage of heavily ionizing particles. The principle of the NTD is based in a fact that when a highly ionizing particle moves inside the NTD, it leaves an invisible damage zone along the trajectory. The damage zone is revealed as a cone shaped etch-pit, when the surface of the plastic detector is etched in a controlled manner using a hot sodium hydroxide (NaOH) solution. The depth of the etch-pit is an increasing function of the  $Z/\beta$  of the particle, where  $Z$  is a particle charge and  $\beta$  is velocity. A schematic picture of the etching process is shown in figure 3.

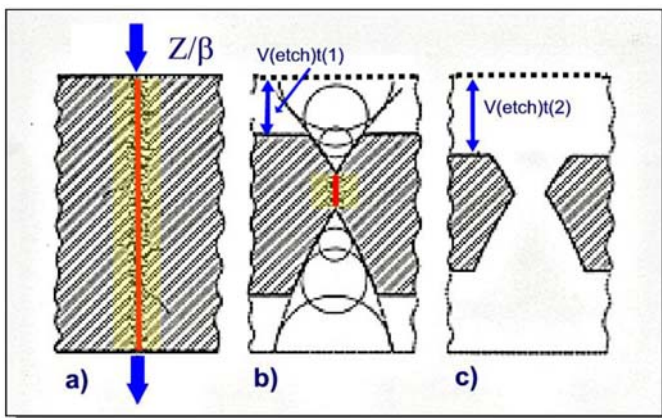


Figure 3. Principle of the etchable NTDs [53].

In figure 3a passage of a particle in the NTD is shown. The moving particle creates a zone of Restricted Energy Loss around the trajectory with a radius of  $\sim 10$  nm. In Figure 3b and 3c results of the etching are shown that depend on  $Z/\beta$  of the moving particle. The damage caused by the moving particle depends only on the dose inside the 10 nm radius and is independent on a dose rate. It is possible to make precise measurement of  $Z/\beta$  of the particle

out to large values of  $Z/\beta$ , which is shown in Figure 4.

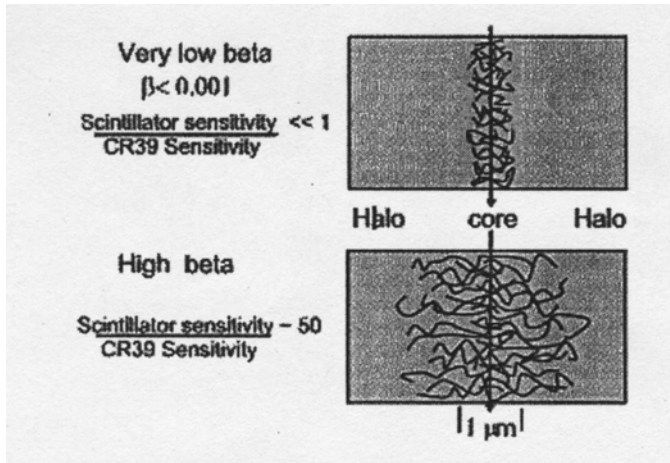


Figure 4. Comparison of very low  $\beta$  and high  $\beta$  particle-damages in NTDs [53].

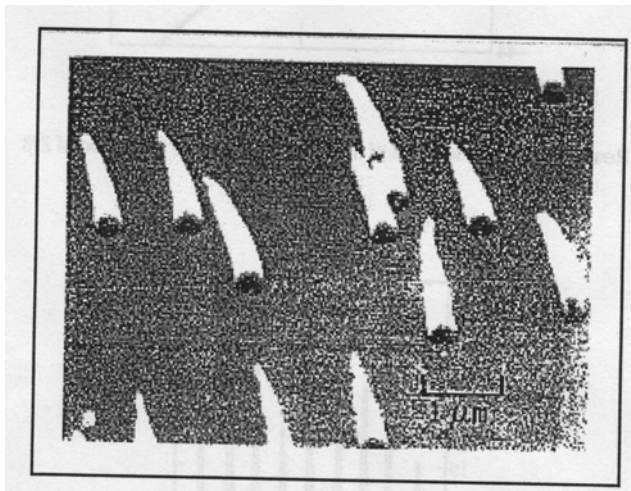


Figure 5. A scanning Electronic Micrograph of etch pits made by 26 keV/u  $^{56}\text{Fe}$  ions with  $\beta=0.007$  [53].

Because of radiation quenching in the dense core region near a monopole trajectory, NTDs is more sensitive to energy deposited in the halo by  $\delta$  rays. After the etching, the NTDs are scanned on electron Micrographs. There are special markers on NTDs, which allow to determine hole position accuracy less than  $100 \mu\text{m}$  in several layers of the NTDs used in the experiments. The etchable NTDs are calibrated using heavy ion beams (see Figure 5).

### 3. Magnetic monopole search experiments

No magnetic monopole has found in the experiments performed so far. Below we will analyze accelerator based monopole search experiments, from the first one performed in 1959 [14] up to the latest published one in 2006 [34] to get an idea of what can be achieved at a RHIC search experiment [55] in comparison to the previous monopole search experiments. A compilation [5] of accelerator based experiments is presented in Table 1. In the table following parameters are shown: the accelerator name or location, reaction type, incident particle momentum (energy),

corresponding center of mass energy, monopole mass limit achieved, cross section limit, value of magnetic charge, experimental technique used, year of publication, and references .

In between the first [14] and the last [34] experiments there were many accelerator-based experiments, which are presented in a table 1. Monopole search was performed practically at all new accelerators, having a new energy domain to explore. Below we will consider the first two experiments at the LBL and at the BNL AGS. Later we will compare experiments within a group with best results in cross section limits and mass coverage achieved.

Table II. Compilation of the accelerator based experiments from PDG [5].

Accele-Rator	Reaction	Beam Energy Gev	$\sqrt{s}$ GeV	Mass limit GeV	Cross Section $\text{cm}^2$	MM Charge	TECN	Year	Ref.
LBL	pA	6.2	3.76	<1	1.e-40	1	EMUL	1959	14
CERN	pA	28.0	7.6	<3	1.e-35	<4	CNTR	1961	15a
AGS	pA	30.0	7.86	<3	2.e-40	<2	CNTR	1963	15
CERN	pA	28.0	7.6	<3	1.e-40	<2	EMUL	1963	15b
IHEP	pA	70.0	11.9	<5	1.e-41		EMUL	1972	16
FNAL	pA	400	28.3	<13	5.e-42	<24	CNTR	1974	17a
ISR	pp	60	60	<30	1.e-36	<3	PLAS	1975	25
FNAL	pA	400	28.3	<12	5.e-43	<10	INDU	1975	17
FNAL	pA	300	24.5		2.e-30		OSPK	1975	17b
IHEP	pA	70	11.9	<5	1.e-40	<2	CNTR	1976	17c
CERN	pp	56	56	<30	1.e-37	<3	PLAS	1978	26
CERN	pp	63	63	<20	1.e-37	<24	CNTR	1978	17d
SLAC	e+e-	29	29	<30	4.e-38	<3	PLAS	1982	27
CERN	pp	52	52	<20	8.e-36		CNTR	1982	24
CERN	e+e-	34	34	10	4.e-38	<6	PLAS	1983	29
CERN	pp	540	540		1.e-31	1,3	PLAS	1983	18
SLAC	e+e-	29	29		3.e-38	<3	PLAS	1984	28
FNAL	pap	1800	1800	<800	3.e-38	$\geq 1$	PLAS	1987	18a
CLEO	e+e-	10.6	10.6	<4	9.e-37	<0.15	CLEO	1987	18b
CERN	e+e-	50-52	50-52	<24	8.e-37	1	PLAS	1988	18c
DESY	e+e-	35	35	<17	1.e-38	<1	CNTR	1988	30
KEK	e+e-	50-61	50-61	<29	1.e-37	1	PLAS	1989	31
FNAL	pp	1800	1800	<850	2.e-34	$\geq 0.5$	PLAS	1990	23
CERN	e+e-	88-94	88-94	<45	3.e-37	1	PLAS	1992	32
CERN	e+e-	88-94	88-94				PLAS	1993	33
CERN	PbA	160A	17.9	<8.1	1.9e-33	$\geq 2$	PLAS	1997	18d
AGS	AuAu	11A	4.87	<3.3	0.65e-33	$\geq 2$	PLAS	1997	18d
FNAL	pap	1800	1800	260-420	7.8e-36	2-6	INDU	2000	19
FNAL	pap	1800	1800	265-410	0.2e-36	1-6	INDU	2004	20
HERA	e+p	300	300		0.5e-37	1-6	INDU	2005	22
FNAL	pap	1800	1800	369	0.2e-36	$\geq 1$	CNTR	2006	34

The first experiment [14] was done at the LBL Bevatron with a proton momentum of 6.2 GeV/c. Nuclear emulsions were used to search for Dirac magnetic monopoles. Different targets were used in the experiment: A 0.005" Aluminum, 0.5" copper and 3mm polyethylene targets were placed in the 14.2 kilogauss magnetic field alternatively. Emulsions were later placed behind the target to detect magnetic monopole, which would have gained ~ 4 GeV energy, when moving in the magnetic field. It was expected that such monopole would deposit their entire 4 GeV energy in the emulsion, when traversing black paper wrapping and 1000  $\mu$  of emulsion. Monopoles with masses between the  $\pi$  meson and the proton were expected to be detected by these emulsions, which were sensitive to highly ionizing particles. The response was checked by observation of a natural  $\alpha$  particle background in the emulsion and by observation of  $\alpha$  particles and fission fragments from  $CF^{252}$ , which had been soaked into several spots of the emulsion. No signal characteristic of monopole passage in the emulsion was found. Different targets used in the experiment used different integrated luminosities. For Aluminum the cross section limit of  $2 \times 10^{-35} \text{ cm}^2$  was achieved and for copper corresponding limit was  $1.5 \times 10^{-37} \text{ cm}^2$ . A polyethylene target was bombarded by an integrated flux of  $10^{17}$  protons and later placed 2.5 cm from nuclear emulsions and was exposed to a 200 kilo-oersted field. No Monopoles were found. The authors concluded, that the cross section is less than  $1 \times 10^{-37} \text{ cm}^2$  per nucleon for the production of Dirac Monopoles with binding energy between 3 and 20 eV in polyethylene.

The next experiments to search for magnetic monopoles were conducted at BNL AGS and at CERN in the early 60s with incident proton momenta of 30.0 and 28.0 GeV/c, respectively.

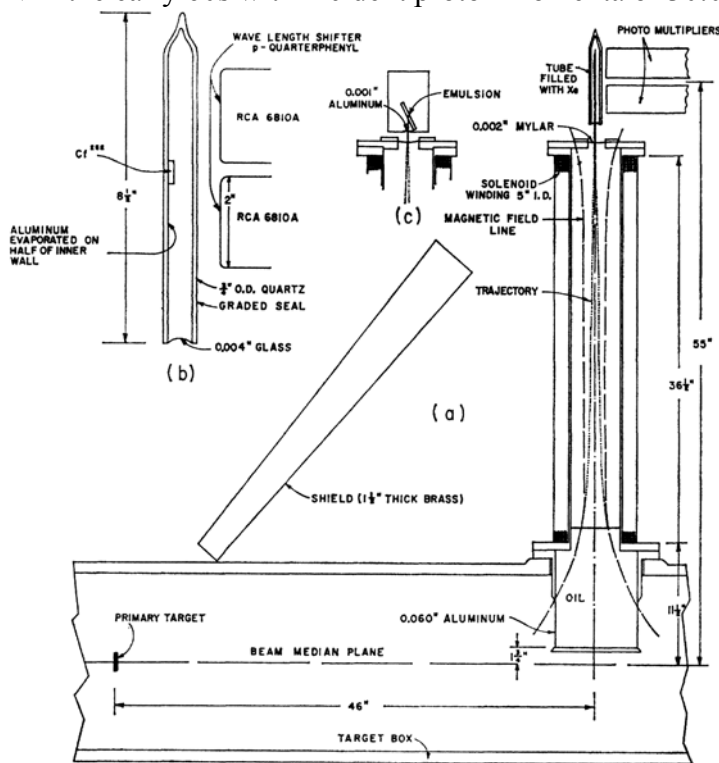


Fig.6. a) Elevation view of the BNL AGS apparatus; b) Details of counter arrangement; c)Upper end of focusing solenoid [15].

We will start with the BNL AGS experiment, where a search was made for a magnetic monopoles produced either in collisions of 30 GeV protons with light nuclei, or produced by  $\gamma$  rays, secondary to these protons in the Coulomb field of protons or of carbon nuclei. Light targets (Be, C, CH<sub>2</sub>, Al) ~0.06" thick were used in the experiment. It was assumed that magnetic monopoles with a 2.4 GeV Rest mass would have a kinetic energy of 7.4 GeV, which is the energy expected for forward projected particles with a velocity comparable to the proton-nucleon center of mass system. Such a monopole will penetrate easily the aluminum wall of the well (0.06" thick) located in the path of the monopole and filled with oil (box on the right of fig.6), and will stop in the liquid oil. The liquid also serves as a target for possible electromagnetic production of monopole pairs by the energetic photons which traverse the well. The oil converter was about a half radiation length thick. Mounted vertically above the well was a long solenoid by means of which a monopole can be accelerated to high energies for detection. A monopole of the appropriate sign, stopping in the oil, is drawn to the free surface of the oil by the field from the end of the solenoid. It is assumed that a bare monopole is accelerated in the evacuated region, arriving at the top of the solenoid with a kinetic energy ~1.1 GeV, number which depends on the monopole charge and the field of solenoid, which was 500 to 700 G, and the effective length of the solenoid, which was 90 cm. The non-uniform field near the lower end of the solenoid is used to focus monopole trajectories into a small aperture at the detector-end, where monopoles were passing through a Mylar window and a few centimeters of the air before entering the detector. Two methods of detection were used: a xenon scintillator, consisting of quartz tube filled with pure xenon and viewed by two photo-multipliers and nuclear emulsions (see Fig.6). Both detection methods relied on the high specific ionization of the magnetic monopole to distinguish it from the copious background of relativistic charged particles. Two runs with the different detection methods were conducted. No tracks that could be attributed to the magnetic monopoles were found. The total number of circulating protons included in counter and emulsion runs was  $5.7 \times 10^{15}$ . Thus the number of entering poles  $N_m$  was calculated by the equation:  $N_m = f N_p t N \sigma_n$ , where  $N_p$  = number of circulating protons,  $t$  – target thickness in  $\text{g/cm}^2$  times average number of target traversals per proton,  $N$  number of nucleons per gram of target =  $6 \times 10^{23}$  and  $f$  = geometrical factor representing the fraction of monopoles which enter the oil and  $\sigma_n$  is monopole production cross section in nucleon-nucleon interactions. The authors found that  $f=0.2$  and  $\sigma_{n, \max} = 2 / (0.2 \times 5.7 \times 10^{15} \times 20 \times 6.0 \times 10^{23}) = 1.4 \times 10^{-40} \text{ cm}^2/\text{nucleon}$  for a monopole mass range from 2.0 to 2.9 GeV range. For lower monopole masses from 1.0 to 2.0 GeV, the  $f$  value is smaller, roughly  $f=0.1$ , and authors obtained  $\sigma_{n, \max} = 3 \times 10^{-40} \text{ cm}^2/\text{nucleon}$ . All the following monopole search experiments were done at higher energy accelerators. Figure 7 shows a compilation of achieved cross sections and mass limits, taken from reference [12]. We will consider these searches in detail in the following pages. In the Figure 7 the authors [12] distinguish two major types of the magnetic search experiments: indirect and direct. According to the authors, in indirect search experiments, beam particles interacted with targets made of ferromagnetic materials. Later the targets were placed in front of pulsed solenoids, to extract and accelerate magnetic monopoles, to be detected by different detection techniques, by SQUIDS or by NTS, emulsions or other track detectors. In direct search experiments magnetic monopole search was performed with different track detection methods, without using pulsed magnets, assuming magnetic monopoles high ionization abilities.

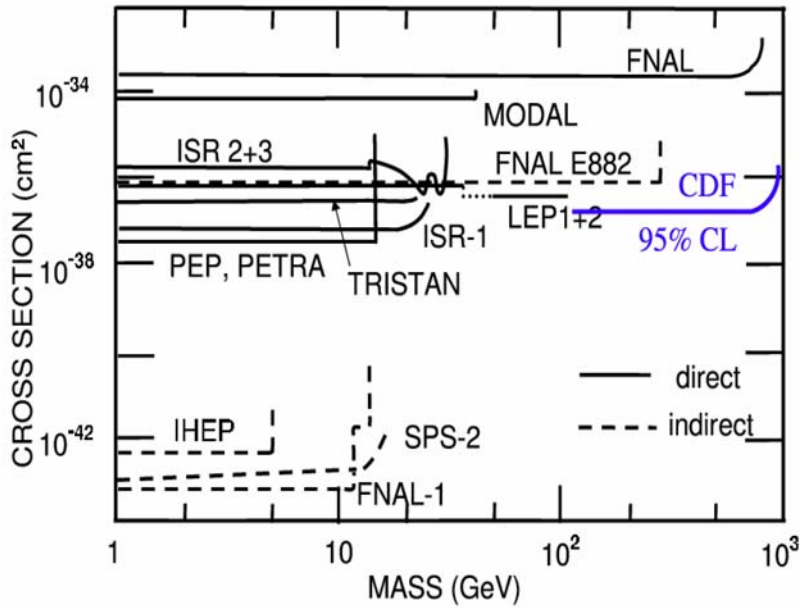


Figure 7. Classical Dirac magnetic monopole cross section upper limits vs magnetic monopole mass obtained from direct accelerator searches (solid lines) and indirect searches (dashed lines) [12].

We will consider experiments in chronological order, starting with indirect search experiments. Indirect search experiments showing the lowest cross section limits were obtained in experiments [16], [17] and [18] with mass limits  $\sim 10\text{-}13$  GeV, while other experiments [19,20,33] get higher cross section, but model dependent higher mass coverage.

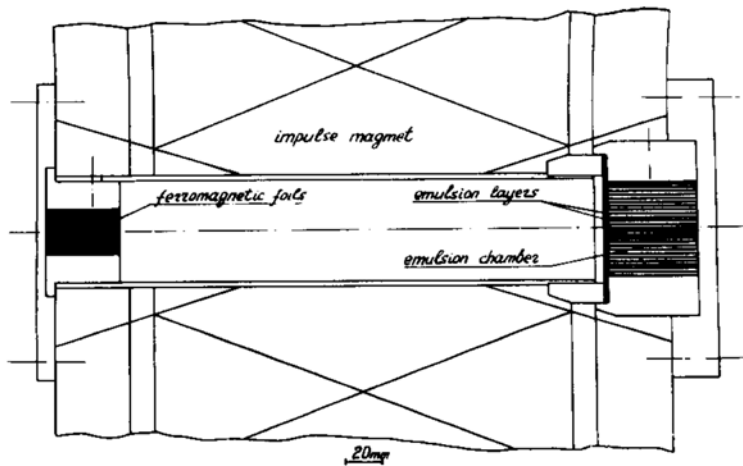


Figure 8. IHEP magnetic monopole search experimental set-up [16].

The first indirect search, we consider, is the IHEP experiment at the 70 GeV proton synchrotron in Serpukhov, Russia [16]. The proton beam interacted with a ferromagnetic

material located inside the vacuum pipe at the edge of the magnet at a distance of 13 cm from the center. At the opposite edge of the magnet two transverse layers of emulsion, 88 mm in diameter were installed. Just behind it was the emulsion chamber of  $55 \times 45 \times 30 \text{ mm}^3$ . This system can detect only negative magnetic charges. Knowing the field distribution along z axis, and the properties of ferromagnetic foils, it is possible to calculate the energies, which monopole with a charge  $g=68.5e$  will reach on the 26 cm path in the magnet. These energies were found to be 21 GeV, 41 GeV and 58 GeV for experiments with permalloy 79 HM, permalloy 50 H, and permendure, respectively. The monopoles will lose this energy in 1-3 cm of nuclear emulsion. This means that tracks of very high ionization ( $\sim 5000$  more than relativistic proton) might be observed not only inside the two transverse layers of emulsion but also inside those layers of the emulsion chamber for which the trajectory of the monopoles lies in the plane of the field of vision of the microscope. To cover the possibility of an anomalous interaction of the monopoles with material, the irradiated samples were placed in a pulsed magnet with a field of  $\sim 800$  kG. In this experiment the detector consists of two layers of nuclear emulsion placed near the ferromagnetic foils (see Figure 9). It was assumed that monopole can be trapped in ferromagnetic material with a 100% efficiency. The assumptions were based on publications [16a, 16b]. According to these publications a force binding the monopole to the ferromagnetic medium is:  $F(Z_0) = 2\pi M_0 g \ln(R/Z_0)$ , where  $M_0$  is the saturation magnetization in the solid,  $R = (g/4\pi M_0)^{0.5}$  is the radius of the sphere of saturation surrounding a monopole of strength  $g$  in a ferromagnetic medium,  $Z_0$  is a cut-off distance, which should not be less than substance inter atomic spacing ( $1\text{\AA}$ ). The magnetic field to extract a monopole from the ferromagnetic material is defined as  $gH_0 > F(Z_0)$ , or  $H_0 > \pi M_0 \ln(g/4\pi M_0 Z_0^2)$ . The minimal magnetic field to extract monopole is  $H = 53$  kG for iron and  $H = 54$  kG for Permendur. The authors also refer to calculations [16c] of forces of attraction in a monopole-electron and monopole-nucleus systems, if the monopole is a Fermi particle and has an electric dipole moment. Attraction potentials are of 4.6 MeV for aluminum and 5.8 MeV for copper.

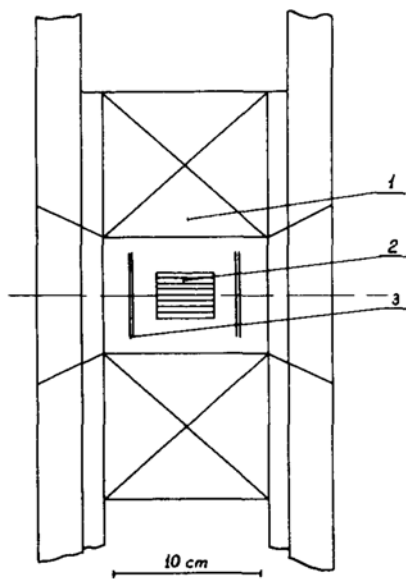


Figure 9. Monopole detection set-up: 1.Pulsed magnet; 2.Packet of samples 3.Nuclear emulsion layers [16a].

In scanning the emulsion layers no tracks were found crossing both transverse layers with ionization noticeably greater than that of relativistic protons. Then the upper limit for the magnetic monopole production cross section in the reaction  $p + N \rightarrow p + N + g^+ + g^-$  is  $\sigma(95\% \text{ CL}) < 1.4 \times 10^{-43} \text{ cm}^2$  if full transparency of the Aluminum target is assumed. If transparency is not assumed and the effective number of nucleons in the nucleus will be  $A^{2/3}=9$  then  $\sigma(95\% \text{ CL}) < 4.2 \times 10^{-43} \text{ cm}^2$ .

Next, experiments were done at FermiLab's proton beam, SLAC's electron-positron collider and and at the CERN ISR in pp interactions [17]. The most significant irradiation was at Fermilab with 300 GeV protons, producing  $2.5 \times 10^{18}$  proton-aluminum interactions. The aluminum targets had various lengths from 16.5 cm to 45 cm in different exposures. In order to search monopoles, that could be produced in pairs in the interactions and trapped in the targets, the target material was first ground into thin chips to separate the north and south poles of a pair, using a milling machine, advancing  $10\mu\text{m}$  between successive cuts (the cut was  $100\mu\text{m}$  deep and 12 mm wide). Then, the chips were placed in a hollow rotating sphere to be randomized. They were divided into 30 samples and the magnetic charge of each sample was measured in an electromagnetic detector, schematically shown in Figure 10. The sample was carried several times around a path that traversed a sensing coil. This coil was a part of a superconducting circuit containing two other coils (field coils), each one wound around a sensitive magnetometer (SQUID). If a sample has a non-zero magnetic charge, it will induce a change of current in the superconducting circuit and a change  $\Delta F1$  and  $\Delta F2$  in the flux measured by SQUIDS 1 and 2. For each SQUID,  $\Delta\Phi/\Phi_0 = v_s N_p/f$ , where  $v_s$  is the ratio of the sample magnetic charge  $g_s$  to the Dirac unit  $g_0 = e/2\alpha = 137/2 \times e$  (in

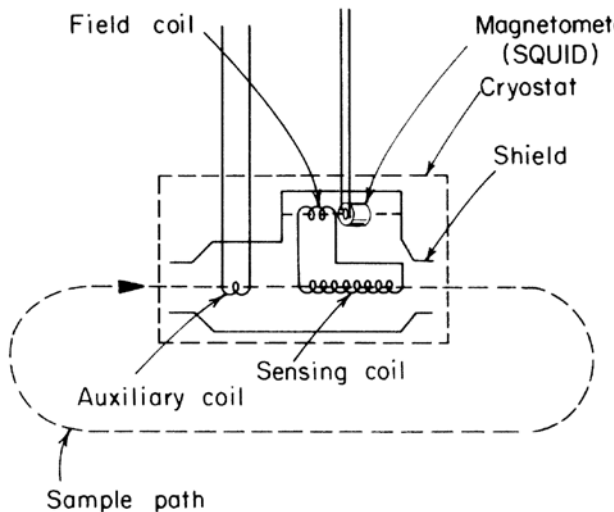


Figure 10. Schematic view of the FNAL monopole detector. Samples are moved along the dashed curve labeled as sample path. The superconducting circuit is shown with the sensing coil and field coil connected in series. The magnetometer and auxiliary coil are also shown inside the cryostat [17].

Gaussian units),  $\Phi_0$  is the flux quantum number of superconductivity ( $2.07 \times 10^{-7} \text{ G cm}^2$ ),  $N_p$  is the number of passes through the sensing coil and  $f$  is a constant, depending on the various inductance values of the circuit. For SQUID1  $f=34$ , for SQUID2  $f= 290$ . The magnetic charge measurement was done by taking magnetometer readings after 1, 3, 9, 27 and 81 passes. This procedure provided

an accuracy of 0.03 for the value of  $v_s$ . The magnetic charges  $v_s$  of all the samples were measured to be consistent with zero and incompatible with any value larger than 0.1. From this result a maximum value of  $R_{\max}$  for the ratio of the number of monopole pairs to the number of interactions and the cross sections was computed at a 95% confidence level. Those calculations were done under the following assumptions: (1) All monopoles are produced with a typical velocity equal to the velocity of the proton-nucleon center of mass system and that they lose  $\frac{1}{2}$  of their energy every time they collide with an aluminum nucleus, as do protons at high energy when they collide with nuclei. (2) North and South poles of a pair with large magnetic charge may stop close enough so that the attractive force between them drives them together toward annihilation. Separation due to multiple Coulomb scattering is sufficient to avoid this effect for  $v < 20$ . For  $10 < v < 60$ , large scale Coulomb scattering, and for  $v > 60$ , nuclear scattering with half energy loss are used to estimate a correction (3). A probability is assumed for the monopoles of a pair to end up in the same chip. (4) If monopoles had charges  $v < 0.1$ , but there were many of them, the statistical fluctuations would generate some measurable charges for the samples. Therefore the experiment allows computation of upper limits for the density of such monopoles with a reduced sensitivity.

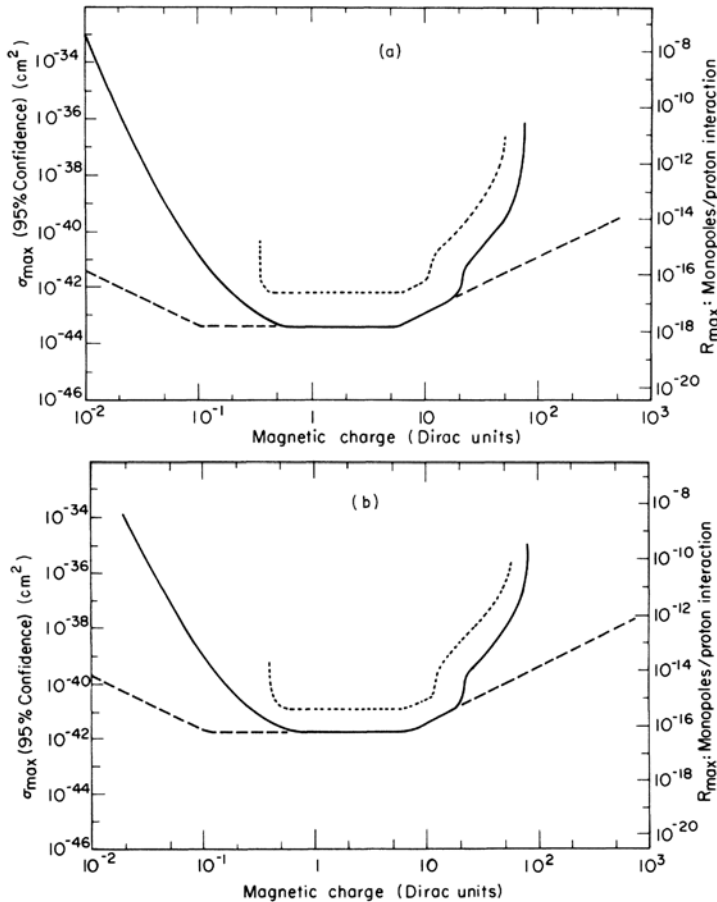


Figure 11. Upper limit (95% confidence level) for monopole pair production cross section in proton-nucleus collisions as a function of magnetic charge. (a) 300 GeV/c protons on aluminum (b) 400 GeV/c protons on aluminum. The solid line curve corresponds to the corrections 1 to 4 described in the text and the dashed curve to corrections 1 and 2 set equal to 1. The dotted curve has been computed using only a 41 cm long target, with a most pessimistic view of the sensitivity of the experiment [17].

Next, experiment [18] was performed with the CERN 400 GeV proton beam. The magnetic monopoles were searched for in a series of ferromagnetic collectors of W-Fe powder exposed to the 400 GeV/c proton beam in an experiment at the CERN SPS. The monopole target was made of tungsten-iron (5%) powder compound with 2-3  $\mu\text{m}$  grain size. The material has a density of  $\sim 12\text{g/cm}^2$ . The energy loss of a fast monopole with ( $n=1$ ) in this material should be 75 GeV/cm. The highly developed ferromagnetic surface in such a target would exclude completely the possibility of bulk diffusion of monopoles and anti-monopoles, thus preventing their annihilation. The W-Fe target was 3 cm in diameter, 31 cm long, and was made of 11 pieces, of which the first five were 1.75 cm long and the last six pieces were 3.5 cm long. They were placed in a metal box (see Figure 12) and were cooled by running water.

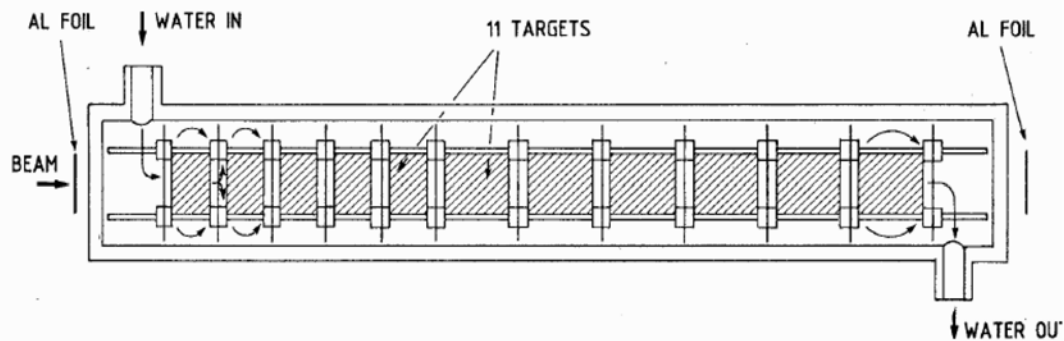


Figure 12. Layout of the monopole target in the CERN SPS 400 GeV proton beam experiment [18].

The total exposure was  $3 \times 10^{17}$  protons on the target. The proton flux was determined by radiochemical methods via thin aluminum foils placed in front of the target. Since the monopole targets were placed after the (anti)neutrino target, it was estimated that they received approximately  $10^{18}$  pions of  $\sim 100$  GeV average energy.

After the exposure the monopole targets were brought to the Kurchatov Institute in Moscow, where monopole extraction was attempted with a strong pulsed magnetic field (see Figure 13).

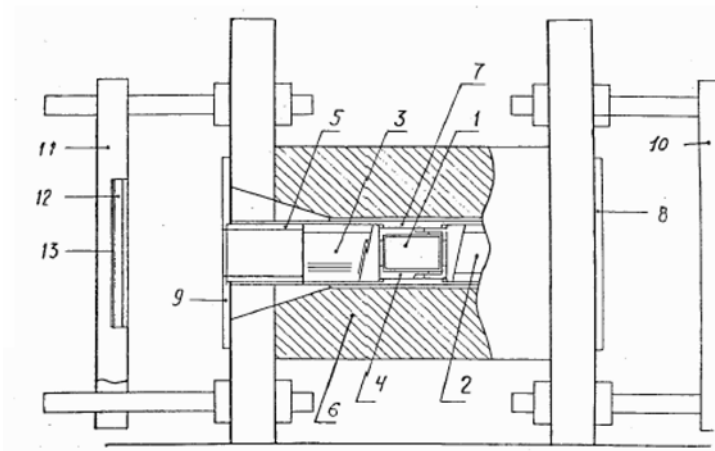


Figure 13. Sketch of the Kurchatov Institute monopole detector system [18].

The detector consisted, on each side, of two nuclear emulsions Br<sub>2</sub> of 400 μ thickness, of two nitrocellulose sheets of 50 μ thickness and of an emulsion chamber. Monopoles of both signs would be detected. Each of the pieces of the monopole target was placed at the center of the magnet. The pulsed magnet has a field  $B_{\max} = 300$  kG, that lasted 7 ms FWHM. The extraction energy of monopoles from the ferromagnetic powder compound corresponds to 50 kG. Monopoles would be extracted at the time the field reached 50 kG. And would be accelerated at the same field (the rise time of field is slow compared to the transit time of the monopoles). In the 3 cm between the end of the target piece and front-end of the nuclear emulsion the poles will gain 3 GeV. Poles with this energy would traverse the 2 nuclear emulsions, the 2 nitrocellulose sheets and the emulsion chambers, where they would lose energy at the rate of  $\sim 100$  KeV/μm with  $n=1$ . Afterwards, they would have the same energy loss rate, they would gain from the magnetic field ( $\sim 1$  GeV/cm). The nuclear emulsions later were scanned with a standard optical microscope. Similarly, the first nitrocellulose sheet on each side was developed and scanned for holes. This system and method of detection should have a global efficiency of 100%.

No magnetic monopoles were found. The upper limits on the monopole production cross-section in reaction of:  $p + N \rightarrow p + N + G^+ + G^- + X$  at the 95% confidence level are  $\sigma < 3 \times 10^{-43}$  cm<sup>2</sup> in 400 GeV pN collisions and  $\sigma < 1 \times 10^{-43}$  cm<sup>2</sup> in 100 GeV πN collisions. The experiment was sensitive to monopoles of different magnetic charges, from a value of 0.1 to  $\sim 20$  Dirac charges. Figure 14 illustrates the cross section limits obtained by various experiments as a function of the monopole mass.

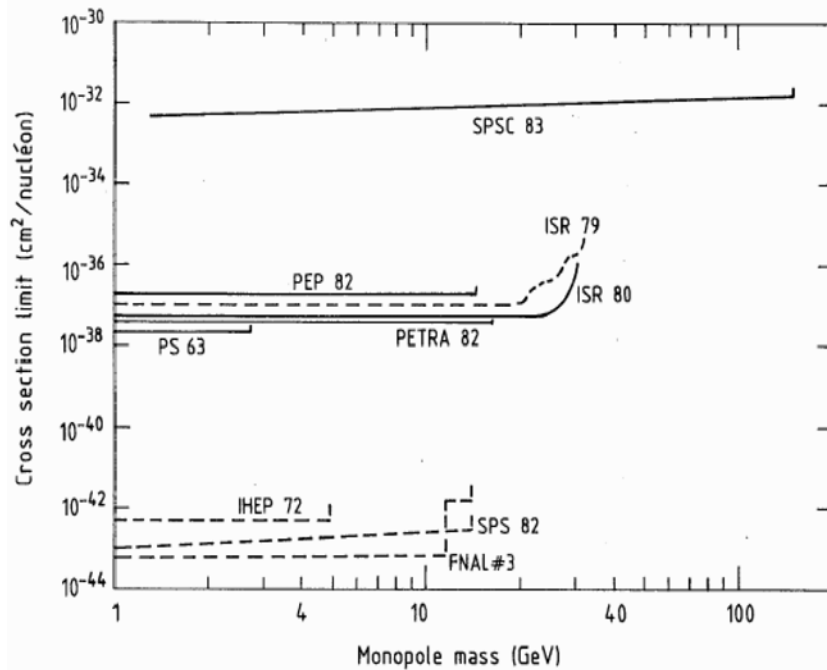


Figure 14 . Compilation of upper limits for Dirac Monopole production in pN, πN, proton anti proton and e+e- collisions. Solid and dashed lines refer to direct and indirect experiments [18].

Next, experiments of this type of search were performed at the FNAL Tevatron in proton-antiproton collisions at 1800 GeV energy. Two experiments conducted by the Oklahoma University group were published in 2000 [19] and 2004 [20]. The first experiment known as FNAL E882 assumed that monopoles are trapped and bound in matter surrounding the D0 collision region

of the FNAL Tevatron. A large warm bore cryogenic detector was constructed and operated at the University of Oklahoma. The active elements of the detector are two 19 cm diameter superconducting loops each connected to a dc SQUID. The Meisner effect prevents a change in the net flux through the loops, resulting in a change, or “step”, in current flowing in the loops

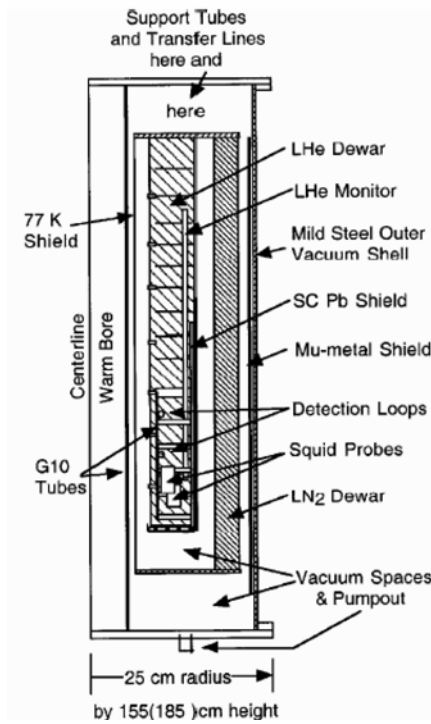


Figure 15. Radial cross section of the monopole detector at the University of Oklahoma [20].

whenever a magnetic charge passes through them. Samples of a size less than 7.5 cm in diameter by 7.5 cm in length are repeatedly passed through the 10 cm diameter warm bore centered on- and perpendicular to the loops, traveling some 108 cm about the position of the superconducting loops. In a central 64 cm region this allows for the magnetic effects of induced and permanent dipoles to

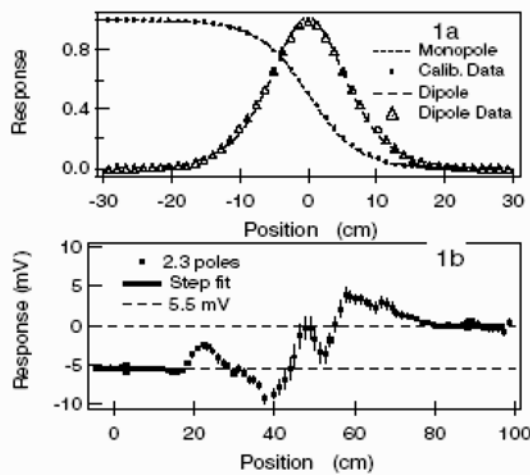


Figure 16. “Pseudopole” curves: (a) Comparison of theoretical monopole response to an experimental calibration and of a simple point dipole of one sample with that calculated from the theoretical response curve. (b) The observed “step” for a pseudopole current, corresponding to 2.3 Dirac poles embedded in

an Aluminum sample [19].

return to zero on each up and each down traversals of the sample. The SQUIDS are tuned and their transfer functions measured periodically according to the manufacturer's specifications in order to keep them operating with constant sensitivity. The absolute calibration of the expected signal from the Dirac monopole was made using a "pseudopole". A long thin magnetic solenoid (1.5 cm diameter by 100 cm length with 4710 turns per meter) carrying a calibrated small current gives a calculable pseudopole at either end. The pseudopole can either be passed through the warm bore of the detector in a way similar to samples or it can be placed in a given position with one end fully extended through the SQUID loops and the solenoid currents repeatedly switched on and off. The shape of observed pseudopole signal is compared to that of theoretical calculations in Figure 16a and the response to a point magnetic dipole is compared to one extracted from the experimental data. Figure 16b shows the step of 5.5 mV (2.3 Dirac poles signal) from a run of a pseudopole embedded in an aluminum sample.

There were 222 Al and 6 Be samples from the experiment. All samples were passed through the detector.

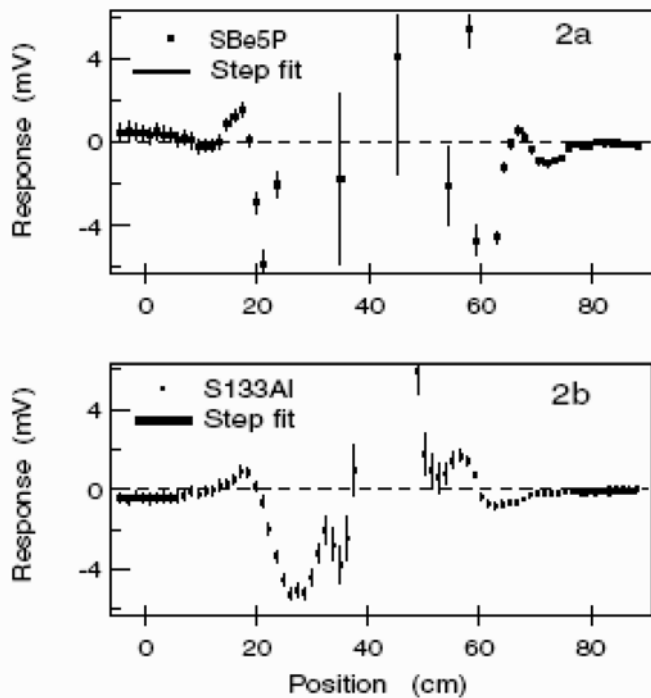


Figure 17. Sample spectra. (a) Beryllium sample and (b) Aluminum sample. The observed steps are -0.8 mV in (a) and +0.4 mV in (b). The dipole signals are off scale in the middle regions of the plot [19].

Figure 17 shows examples of the responses from the detector for Be (a) and Al (b) samples "Sbe5P" and "S133Al" respectively. The steps from various samples are plotted in Figure 18. The distribution of steps for data has a mean value of 0.16 mV and spread (sigma) of 0.73 mV. A 90% confidence limits for monopole charges of  $n = 1$  or  $-1$  can be obtained by considering the number samples that are within 1.28 sigma of the  $n = \pm 1$  positions, corresponding to samples outside of the central region of  $\pm 1.47$  around zero. Eight samples were found outside this central

region, where 10.4 were to be expected from Gaussian error. The 90% confidence upper limit is 4.2 signal events for 8 events observed when ten were expected. In order to be sure that none of the 8

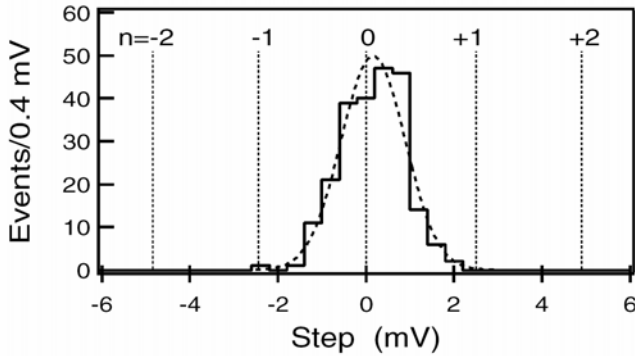


Figure 18. Histogram steps. Vertical dashed lines define the expected positions of signals for various  $n$ . The Gaussian curve (dashed) corresponds to 228 measurements having an average value of 0.16 mV and rms 0.73 mV [19].

outlying samples were monopole candidates, the authors measured again the samples that fell within  $\pm 1.47$  mV of  $n = 0$ . No samples are within a 1.28 sigma of the  $|n| > 2$  positions, the closest being 3.08 sigma away from  $n = -2$ . The 90% confidence upper limit is 2.4 signal events for zero events observed and zero expected. The upper limit numbers (4.2 and 2.4) are used to derive cross section upper limits for  $|n|=1$  and  $|n| \geq 2$ , respectively. Further it is assumed that monopoles are ranged out and stopped and that they bind to the magnetic dipole moments of the appropriate nuclei  ${}^9\text{Be}$  or  ${}^{27}\text{Al}$  and thus are trapped. It is assumed that the interaction of the monopoles with magnetic moments of nuclei and electrons can be strong enough to produce bound states under certain conditions causing the monopoles to be trapped, having a very long lifetime in such bound states [21]. The trapping efficiency is very high. The theoretical modeling that has been done assumes “rigid” extended nuclei with or without repulsive barriers, and some calculations have also been carried out. Electrons can bind to monopoles in a total energy zero state; this probably produces a small mobile system, which will attach to a nuclear magnetic moment leaving it bound to a fixed nuclear site and permanently trapped. Thus these authors assume that all monopoles bind to appropriate nuclei, i.e., those whose nuclear gyro-magnetic ratio is sufficiently large (anomalous). These models predict, as summarized in Ref. [21], that binding should occur for  ${}^{27}\text{Al}$  (100% natural abundance) and  ${}^{207}\text{Pb}$  (22% natural) but not for  ${}^9\text{Be}$  (100% natural). However, the estimated binding energies, e.g., 0.5–2.5 MeV for aluminum, are large and comparable to shell model splitting, so the authors believe that in the presence of the monopole the nucleus will undergo nuclear rearrangement and binding should in general result, even for  ${}^9\text{Be}$ . Even an unreasonably small estimate for the binding energy of 1 eV would give a lifetime of 10 yr [21]. According to these assumptions, the authors claim that there are a good reasons to believe that stopped monopoles will be trapped by the magnetic moments of nuclei.

The monopole production is assumed to derive from a Drell-Yan process: quark-antiquark annihilation to monopole-antimonopole pair via an intermediate high mass virtual photon. The shape of the energy distribution follows from a dimensional argument that is basic to Drell-Yan:  $M^3 ds/dM$  is dimensionless, where  $M$  is the invariant mass of the pair of monopoles. This  $pp$  cross section must include a threshold phase space factor and the velocity dependence of the monopole interaction. The threshold factor is  $\beta$ , the velocity of the monopole in the c.m. system. We take the interaction factor to be  $\beta^2$ , since the Lorentz force for magnetic charges  $g$  is  $\mathbf{F} = g(\mathbf{H} - \mathbf{v} \times \mathbf{D})$ . Thus

the energy shape of  $d\sigma/dM$  is  $(\beta/M)^3$ , convoluted with the momentum distributions of the quarks in the colliding proton and antiproton. The total cross section for the monopole production after

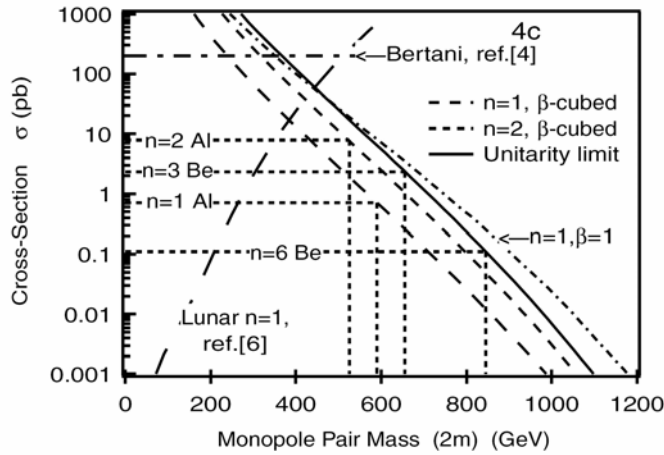


Figure 19. Monopole production cross section plot measured in the E882 FNAL experiment [19].

renormalization by  $n^2 \times 68.5^2$  and  $\beta^3$  convolution is shown in Figure 19. Using the total luminosity delivered to D0,  $172 \pm 8 \text{ pb}^{-1}$ , the number limit of monopoles, the (model dependent) acceptance, and the solid angle coverage, the authors get the  $pp^-$  cross section limits shown in Table III. These limits are of order 100 times better than the Tevatron limit [23] of 200 pb. One can further interpret these limits as mass limits using the scaled Drell-Yan cross sections. Here the cross section is taken to be  $n^2 \times 68.5^2$  larger than the Drell-Yan muon pair cross section, modified by  $\beta^3$ , for  $pp^-$  interactions measured by CDF [19a] and by D0 [19b]. For such large cross sections a unitarity limit appears at an equivalent  $n^2=9$ . The authors use the  $n=1$  or 2 scalings for the cases  $n=1$  or 2, and the unitarity limit for higher  $n$  values in converting cross section limits into mass limits.

TABLE III. Acceptances, upper cross section limits, and lower mass limits as determined in this reference [19] (at 90% C.L.).

Magnetic charge	$ n =1$	$ n =2$	$ n =3$	$ n =6$
Sample	Al	Al	Be	Be
$\Omega/4\pi$ acceptance	0.12	0.12	0.95	0.95
Mass acceptance	0.29	0.015	0.0065	0.13
Number of poles	<4.2	<2.4	<2.4	<2.4
Upper limit on cross section	0.70 pb	7.8 pb	2.3 pb	0.11 pb
Monopole mass limit	>295 GeV	>260 GeV	>325 GeV	>420 GeV

The University of Oklahoma group performed a second search of magnetic monopoles with increased statistics including data from CDF and D0 detectors each exposed to a proton-antiproton luminosity of  $\sim 175 \text{ pb}^{-1}$  [20]. The method of measurement was the same as in the previous experiment [19]. There were three sets of samples obtained from discarded material from the upgrading of the D0 [20b] and CDF [20c] detectors: (1) Be beam pipe and Al “extension” cylinders from D0, (2) Pb from the forward/backward “FEM” forward electromagnetic calorimeters of CDF, and (3) half of the Al cylinder (“CTC” support) from CDF sample. Set 1 and 3 were published [20], and set 2 was reported in a PhD thesis [20a]. All three sets are reported according to a final consistent analysis. Here we present a plot of the

step functions obtained for 240 Aluminum samples extracted from the CDF experiment (See Figure 20). Similar step functions were obtained also for other sets of data.

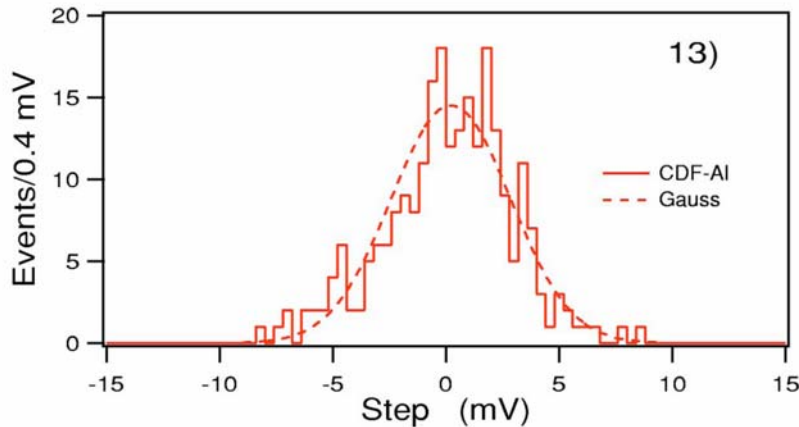


Figure 20. Histogram of the steps from 240 aluminum samples from the CDF experiment, with an rms dispersion of 2.7 mV compared to the appropriate Gaussian. These data are used for obtaining limits for the three magnetic charge values  $|n| = 2, 3, \text{ and } 6$  [20].

A number of parameters need to be taken from these plots and interpreted to yield the cross sections and mass limits desired. Each plot determines an upper limit on the number ( $N_{ul}$ ) of monopoles of a given magnetic charge ( $n = 1, 2, 3, 6$ ) for each sample set, which in turn determines an upper limit to the corresponding cross section  $\sigma < N_{ul} / \epsilon \epsilon AL$ , where  $\epsilon$  is the efficiency for the chosen signal (a monopole with charge  $n$ ) to lie outside a cut excluding smaller values of  $|n|$ ,  $\epsilon$  is the efficiency of the sample set to cover the solid-angle region chosen and to correct for cuts used.  $L$  is the total luminosity for the  $pp^-$  exposure delivered ( $172 \pm 8 \text{ pb}^{-1}$  for D0 and  $180 \text{ pb}^{-1} \pm 5\%$  for CDF). A Drell-Yann model is used for the production cross section estimation. Figure 21 shows observed cross sections versus the monopole mass for the different center of mass monopole angular distributions. These cross-section limits are some 250–2500 times smaller and the mass limits are 2–3 times larger than those of reference [23].

The last experiment for indirect magnetic monopole search was performed at the DESY HERA  $e+p$  collider at center of mass energy of 300 GeV [22]. The beam pipe surrounding the interaction region in 1995–1997 was investigated using a SQUID magnetometer to look for stopped magnetic monopoles. During this time an integrated luminosity of  $62 \text{ pb}^{-1}$  was delivered. For the search reported here the fact is used that heavily ionizing magnetic monopoles produced in  $e+p$  collisions may stop in the beam pipe surrounding the H1 interaction point at HERA. The binding energy of monopoles which stop in the material of the pipe (aluminum in the years 1995–1997) is expected to be large [21] and so they should remain permanently trapped, provided that they are stable. The beam pipe was cut into long thin strips which were each passed through a superconducting coil coupled to a SQUID. Figure 22 shows a schematic diagram illustrating the principle of the method used. Trapped magnetic monopoles in a strip will cause a persistent current induced in the superconducting coil by the magnetic field of the monopole, after complete passage of the strip through the coil. In contrast, the induced currents from the magnetic fields of the ubiquitous permanent magnetic dipole moments in the material, which can be pictured as a series of equal and opposite magnetic charges, cancel so that the current due to dipoles returns to zero after passage of the strip.

TABLE IV. Alternative interpretations for different production angular distributions of the monopoles, comparing  $1$  and  $1-\cos^2\theta$  to the  $1+\cos^2\theta$  limits. Here the acceptance  $A_a$  corresponds to the distribution  $1+\cos^2\theta$ , and similarly for the cross section and mass limits (all at 90% confidence level).

Set	n	$\sigma_{+1}^{\text{ul}}$ (pb)	$m_{+1}^{\text{LL}}$ (GeV/c <sup>2</sup> )	$A_0$	$\sigma_0^{\text{ul}}$ (pb)	$m_0^{\text{LL}}$ (GeV/c <sup>2</sup> )	$A_{-1}$	$\sigma_{-1}^{\text{ul}}$ (pb)	$m_{-1}^{\text{LL}}$ (GeV/c <sup>2</sup> )
1 Al	1	1.2	250	0.024	1.2	240	0.021	1.4	220
1A1 RM	1	0.6	275	0.024	0.6	265	0.021	0.7	245
2Pb	1	9.9	180	0.011	12	165	0.0055	23	135
2Pb RM	1	2.4	225	0.009	2.9	210	0.0045	5.9	175
1 A1	2	2.1	280	0.0068	2.2	270	0.0060	2.5	250
2Pb	2	1.0	305	0.018	0.9	295	0.016	1.1	280
3 A1	2	0.2	365	0.10	0.2	355	0.096	0.2	340
1 Be	3	3.9	285	0.0025	5.6	265	0.0003	47	180
2Pb	3	0.5	350	0.029	0.5	345	0.031	0.5	330
3 A1	3	0.07	420	0.20	0.07	410	0.24	0.06	405
1 Be	6	1.1	330	0.008	1.7	305	0.0008	18	210
3 al	6	0.2	380	0.066	0.2	375	0.082	0.2	370

The beam pipe around the interaction point had a diameter of 9.0 cm and a thickness of 1.7mm in the range  $-0.3 < z < 0.5\text{m}$  and a diameter of 11.0 cm and thickness 2mm in the range  $-0.3 < z < 0.5\text{m}$  and a diameter of 11.0 cm and thickness 2mm in the range  $0.5 < z < 2.0\text{m}$ . During HERA operations it was immersed in a 1.15 T solenoidal magnetic field which was directed parallel to the beam pipe, along the  $+z$  direction. This length of the pipe, covering  $-0.3 < z < +2.0\text{m}$ , was cut into 45 longitudinal strips each of an average length of 573mm ( $\sim 2$  mm was lost at each cut). The central region ( $-0.3 < z < 0.3\text{m}$ ) was cut into 15 long strips of width  $\sim 18$  mm, two of which were further divided into 32 short segments varying in length from 1 to 10 cm. The downstream region ( $0.3 < z < 2.0\text{m}$ ) was divided into 3 longitudinal sections each of which was cut into 10 long strips of  $\sim 32$  mm width. The long strips and short segments were each passed along the axis of the 2G Enterprises type 760 magnetometer [22a] at the Southampton Oceanography Centre, UK. This is a warm bore device with high sensitivity and a low noise level which is normally used to measure the residual magnetism in rock samples. It consists of three superconducting coils of diameter 8.1 cm diameter, one with its axis parallel to the conveyor belt which carried the sample (the axial coil, see Fig. 22) and one oriented in each transverse direction. The data from the transverse coils showed only a small sensitivity to the passage of a calibration pseudo-monopole. Hence only the data from the axial coil were used in the measurements presented by the authors. The samples of strips and segments were passed through the magnetometer in steps, pausing after each step, after which the current in the superconducting loop was measured. The residual persistent current after the complete traversal of a sample through the loop was measured by taking the difference in the measured current after and before passage. The readings for each sample were repeated several times. This allowed the reproducibility of the results to be studied so that random flux jumps and base line drifts could be identified. Any real monopole trapped in the pipe would give a consistent and reproducible current step. Figure 23 shows an example of current measurements.

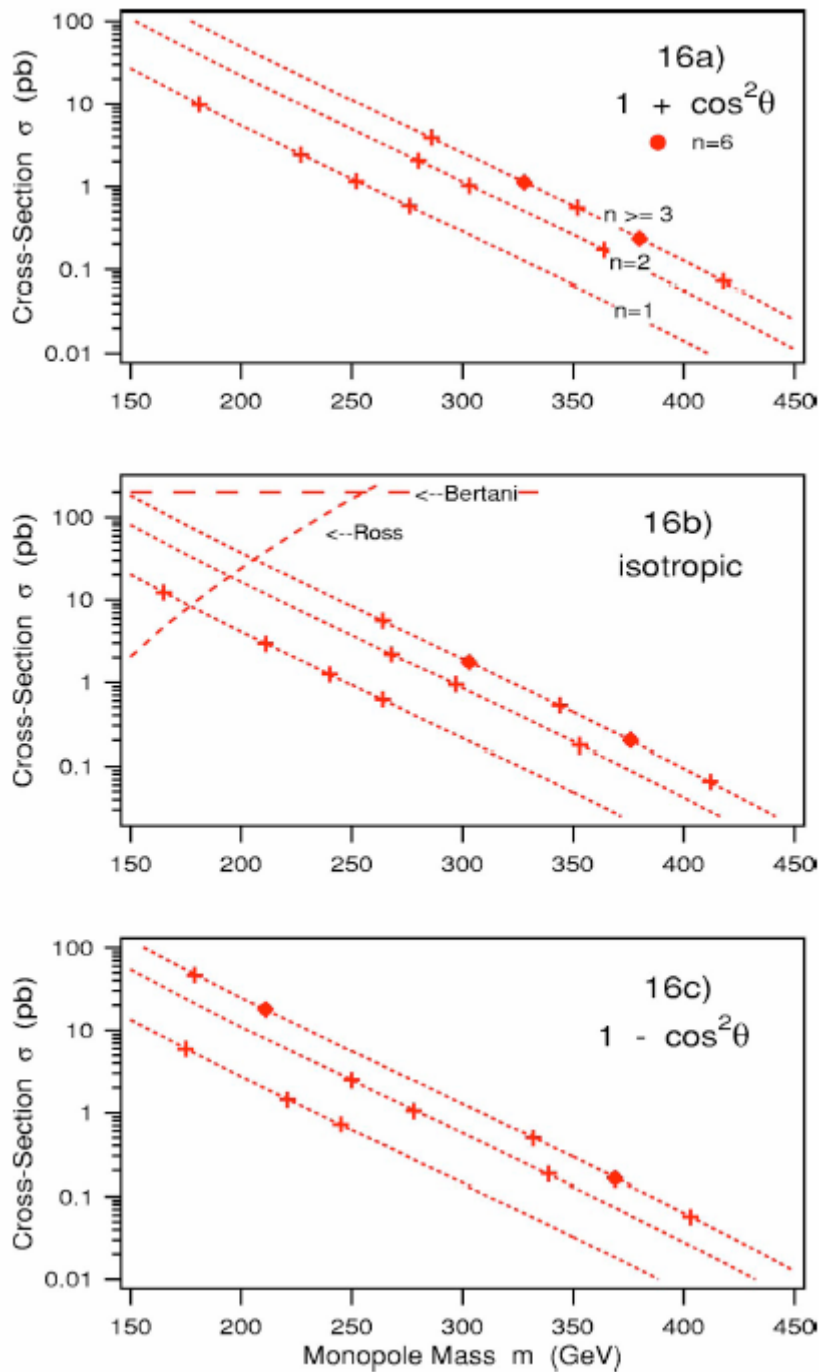


Figure 21. The curves are Drell-Yan cross sections versus monopole mass with cross-section upper limits (90% CL) interpreted as mass limits (cross-section upper limit intersects the Drell-Yan curve at an estimated lower limit of mass as shown by + and point markers). Three possible center-of-mass angular distributions are considered, of form  $1 + a \cos^2 \theta$  with  $a = 1, 0,$  and  $-1,$  respectively. Shown also in (b) are the lunar limit from Ref. [20e], and the accelerator limit from Ref. [23].

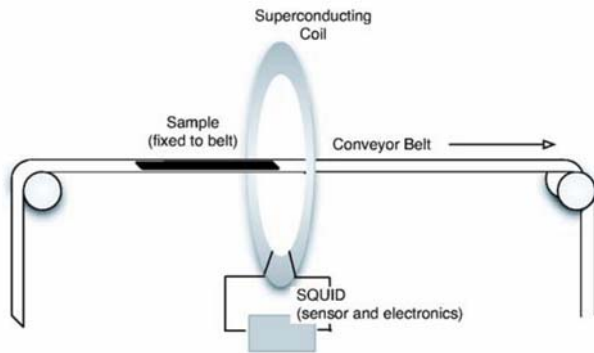


Figure 22. The schematic diagram shows the principle of the method. The conveyor belt moved in steps of typically 5 cm until the sample traversed completely the superconducting coil. At each step the conveyor belt stopped for 1 s before the current in the superconducting coil was read to avoid the effects of eddy currents. The time for each step was typically 3 s [22].

It can be seen that none of the fluctuations observed in single readings occurred consistently in other readings on the same sample showing that no trapped monopole was present.

To derive an upper limit on the measured cross section it is necessary to compute the acceptance, i.e. the fraction of the monopoles produced which would have been detected. A model of the production process is therefore needed. Two models were used to compute the acceptance by Monte Carlo technique. In each of these a monopole- antimonopole ( $MM\bar{}$ ) pair was assumed to be produced by a photon-photon interaction. The first model (model A) assumed spin 0 monopole pair production by the elastic process  $e+p \rightarrow e+MM\bar{p}$  through the interactions of a photon radiated from each, the electron and the proton. The proton was assumed to have the simple dipole form factor  $1/(1 + Q^2/0.71\text{GeV}^2)$ , where  $Q^2$  is the negative square of the four momentum transferred to the proton. The second model (model B) assumed spin 1/2 monopole pair production by the inelastic process  $e+p \rightarrow e+MMX$  (where X is any state) through a photon-photon fusion interaction with a photon radiated from the electron and one radiated from a quark in the proton. The photon is radiated with a simple distribution given by  $(1-\eta)^5/\eta$ , with  $\eta$  the fraction of the proton's energy carried by the photon. While the models implement the cinematic correlations in each event, it should be noted that they depend on

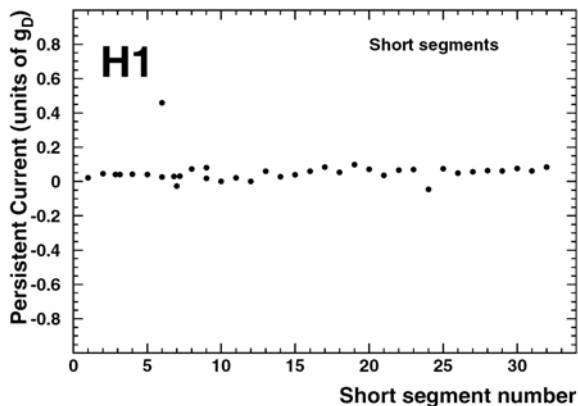


Figure 23. The measured persistent currents (in units of  $g_D$ ), after passage through the magnetometer, plotted against sample number for the two strips of the central beam pipe which were cut into short segments [22].

perturbation theory and therefore the predicted cross sections are unreliable. Events were generated according to model A using the program CompHEP [22b] and using a dedicated program for model B. The generated final state particles were tracked through the H1 magnetic field to the beam pipe. If the thickness of beam pipe traversed was greater than the calculated range of the monopole in aluminum, it was assumed to stop. In this way the fraction of monopoles, which were detected by stopping in the beam pipe, was computed. Figure 24 shows obtained cross section limits for the two models.

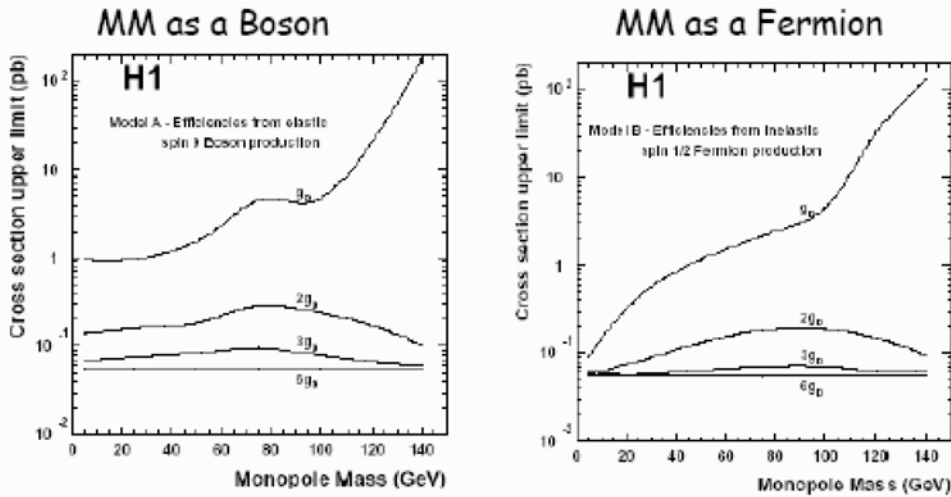


Figure 24. Upper limits on the cross section, determined within the context of model A (left) and model B (right), for monopole-antimonopole pair production in  $e+p$  collisions as a function of monopole mass for monopoles of strength  $g_D$ ,  $2g_D$ ,  $3g_D$  and  $6g_D$  or more [22].

The failure to observe a monopole candidate means that there is an upper limit of 3 monopole pair events produced at the 95% confidence level. The cross section upper limit is then calculated from this, taking into account the uncertainties in the measured integrated luminosity and in the fraction of the pipe surviving the cutting procedure, and the statistical uncertainty in the acceptance computed from the models described above. Here the acceptance is the fraction of the monopole pairs which produce either one or both monopoles which stop in the beam pipe. Figure 24 (left plot) shows the upper limit on the cross section at 95% confidence level for monopoles of strength 1, 2, 3 and  $6g_D$  using acceptances determined from model A. Figure 24 (right plot) shows the upper limits determined using the acceptances from model B. Thus, the upper limits on the monopole pair production cross section have been set for monopoles with magnetic charges from 1 to  $6g_D$  or more and up to a mass of 140 GeV within the context of the models described.

We have discussed above indirect experimental methods of magnetic monopole detection. All these experiments assume that produced magnetic monopoles can stop, be trapped and be bound in the material surrounding a collision region. There are several assumptions made here [21] based on estimated binding energies of  $\sim 0.5$ - $2.5$  MeV, comparable with a shell model splitting, achievable when magnetic monopole is trapped in ferromagnetic materials. These assumptions were criticized in publication [12] claiming that it is difficult to establish the validity of the hypotheses made, to interpret the indirect experimental results. We here also

agree with the conclusion made in [12], that it currently seems impossible to check assumptions presented in reference [21].

Now we will consider the direct search experiments presented in Figure 7. We start with the FNAL 1800 GeV center of mass energy proton-antiproton experiment at the FNAL Tevatron [23]. The search was based on the plastic track detector techniques, using CR-39 NTDs. Twenty-two stacks of  $7 \times 13 \text{ cm}^2$  foils were placed around the 10 cm diameter, 0.16 mm thick, stainless-steel beam pipe at the E0 interaction point. 14 stacks were exposed for 4 months, 6 stacks were exposed for 6.5 months and remaining ones were exposed for  $\sim 2$  months. Each stack consists of 4 layers of CR39, each 1.4 mm thick, and 4 layers of Lexan, 0.35 mm thick, in 4 stacks also included 2 layers of nitrocellulose, 0.3 mm thick. The stacks covered a solid angle ranging between 0.7 to 0.3 of  $4\pi$  in the different running periods. The first layer of CR39 was etched in a NAOH solution 8N at  $80^\circ\text{C}$  for 80 to 100 hours. This strong etching procedure reduces the thickness of the sheet from 1.4 mm to about (0.5-0.2) mm. A monopole that traversed a sheet would result in a hole after etching and thus would be easily detectable. The etched CR39 plates were scanned with a stereoscopic microscope type Wild-M4 using low magnification  $\times 6$  and  $\times 40$ . Only 3 holes were found in the strongly etched sheets. For this case, in order to look for a coincidence, the authors etched the second CR39 sheets of the stack using a more conventional etching technique, in NAOH, 6N, at  $60^\circ\text{C}$  for 30 hours. No tracks were found at the place anticipated from the holes in the first plate.

In order to measure the effective threshold of the used CR39 when heavily etched, as well as for normal etching, the authors exposed stacks of CR39 to relativistic sulfur ions of 200 GeV/nucleon at the CERN-SPS (see Figure 25) and to 0.6 GeV/nucleon neon ions at the Bevalac at Berkley. They found a threshold of  $Z/\beta=8$  for both normal and heavy etching. Thus, the efficiency of monopole detection is almost 100% with  $\beta > 0.2$  and  $n > 0.5$ . Taking into account the integrated luminosity, the solid-angle coverage and the detection efficiency the authors obtained an upper limit of monopole production cross section  $\sigma < 2 \times 10^{-34} \text{ cm}^2$  (95% confidence level) with  $n > 0.5$  and mass less than 850 GeV. For the masses smaller than 50 GeV the detection efficiency decreases and the limit increases slightly.

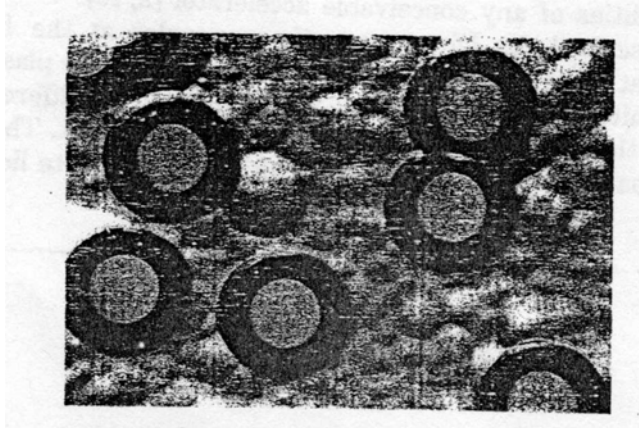


Figure 25. Micro photograph of CR-39 exposed to 200 GeV/nucleon sulfur ions. Holes are due to the sulphur nuclei [23].

The plot of monopole production cross section versus the monopole mass was published in the conference materials of the NATO Advanced Study Institute in 1983 [24] and is shown in Figure 26 corresponding to  $5 \times 10^{-38} \text{ cm}^2$  and a mass limit up to 20 GeV.

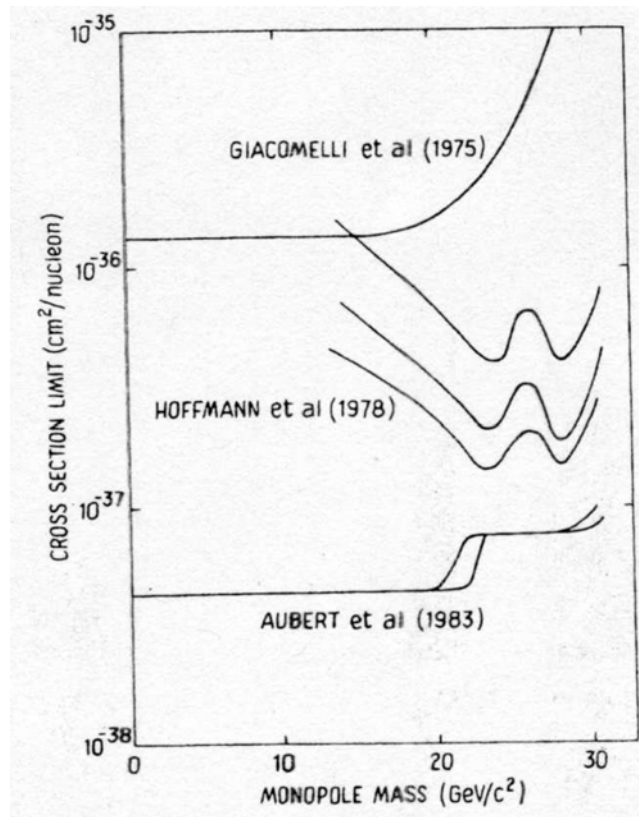


Figure 26. The 95% confidence level limits on monopole production cross section as a function of monopole mass in the ISR experiment [24].

The next two experiments [25] and [26] continued a search for magnetic monopoles at the CERN ISR complex. In experiment [25] most of the exposure was done at the pp cms energy of 45 and 53.2 GeV and also at 62.8 GeV. 12 stacks of plastic sheets were placed around the interaction region I1 of the ISR. Each stack consisted of 10 plastic sheets, each 200  $\mu\text{m}$  thick, with a surface of  $(9 \times 12) \text{ cm}^2$ . The 3<sup>rd</sup> and 5<sup>th</sup> sheets of each stack were of Makrofol-E, and the 8 others nitrocellulose. The 10 sheets of each stack were positioned on supports by means of 3 pins. This references made it possible to follow tracks from one sheet to another with an uncertainty of (20-30)  $\mu\text{m}$ . The experimental layout is shown in Figure 27 and Figure 28 shows

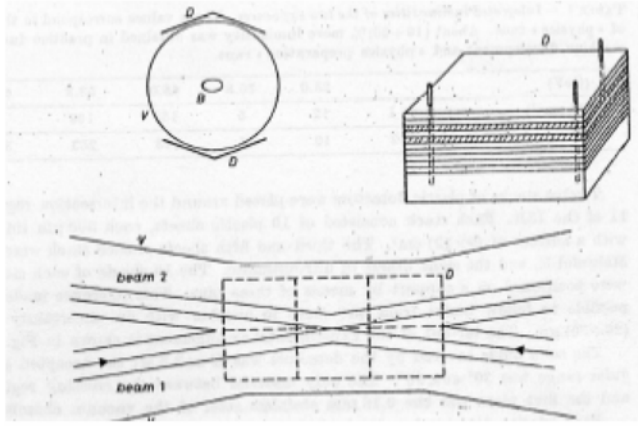


Figure 27. Experimental layout of the CEERN ISR experiment. B – beam, V – vacuum chamber, D – detector [25].

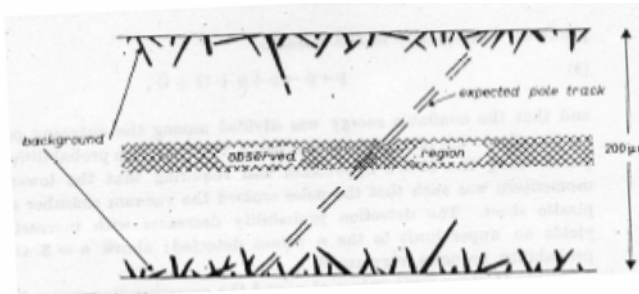


Figure 28. Illustration of the scanning procedure of the nitrocellulose sheets. Several background tracks, a monopole candidate and the scanning region are shown [25].

an illustration of the scanning procedure. The solid angle covered by the detector was 3.5 sr. The only material between the crossing region and the first plate was the 0.18 mm stainless steel of the vacuum chamber. Tracks were developed by the etching process. The nitrocellulose sheets were etched in a NaOH 5N solution at 50 C<sup>0</sup> for 60 minutes. The etch was long enough to ensure that the track left by a monopole traversing the 0.2 mm thickness of the sheet would be completely visible for any geometrically possible angle of incidence. A monopole candidate is expected to produce a signal at least in the first nitrocellulose sheet (see Figure 28). The background limit is given by nuclear fragments of low energy with  $Z > 2$ , produced in the interactions. The measurements show, that  $10^5$  protons were needed to produce one visible track at the surface of the nitrocellulose sheets. The corresponding figure for Makrofol-E is about  $10^7$  protons. In the etched plates these fragments yield a general background which shows up as randomly oriented tracks. The background tracks appear only at the two surfaces of the sheet. On the average these tracks do not penetrate farther than 15  $\mu\text{m}$ , and only a few tracks penetrate up to (40-50)  $\mu\text{m}$ . Consequently, the scanning was performed by focusing in a region between the two surfaces of the sheet and looking for tracks crossing the whole thickness (see Figure 28). A standard optical microscope with magnification of 26x, 10x was used.

No monopoles were found. The authors estimated upper limits at 95% confidence level. The Table V shows obtained limits for the different center-of-mass energies and monopole masses and charges ( $n=1,2$ ).

Table V. Upper limits for the production cross section for free monopoles (95% CL) [25].

	$m_g/m_p$	Ecm GeV			$\sigma$ ( $10^{-36}$ cm $^2$ )
		45.0	53.2	62.8	
n = 1	5	94	96	98	1.5
	10	94	96	98	1.5
	20	56	85	94	1.9
	25	0	57	90	1.5
	30	0	0	61	54
n = 2	5	76	84	89	1.8
	10	68	79	87	1.9
	20	0	23	68	8.8
	25	0	0	40	83

Figure 29 shows a comparison of the obtained results (line 7) to the other experiments.

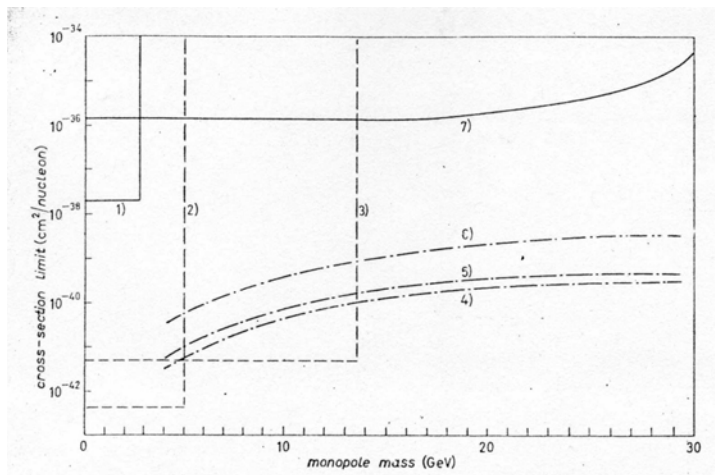


Figure 29. Cross section limit obtained in the ISR experiment [25] (line 7) with other experiments.

Another group [26] performed monopole search experiments at the CERN ISR at the energies of 53.2 and 62.8 GeV. A schematic view of the experimental set-up is shown in Figure 30. The exposure took place in the intersection I1 using the superconducting solenoid magnet with a longitudinal field of  $\sim 1.5$  T. The detectors were placed outside the 2 mm thick steel vacuum tank. The geometrical acceptance was 0.5 % of the total angle, near 0 and 180 degrees to the beam. The magnetic field is expected to accelerate monopoles, allowing them cross the steel wall without significant loss. Four stacks of NTD detectors, each containing 4 200 $\mu$ m thick sheets, were mounted on supports.

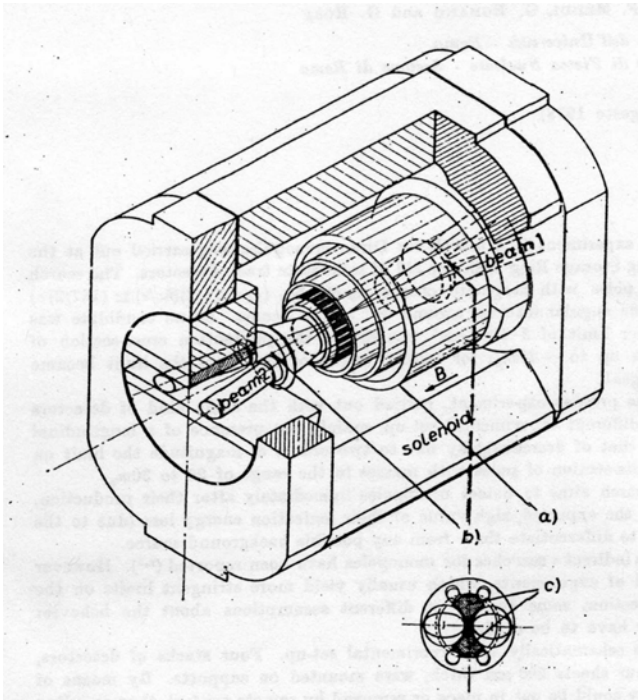


Figure 30. Schematic experimental set-up of CERN ISR experiment [26]. a) detector for another experiment b) vacuum chamber c) plastic detectors

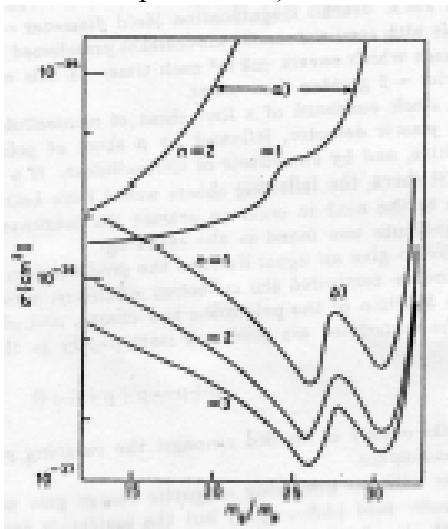


Figure 31. Upper limits on the monopole production cross section (95% cl) as a function of mass and charge. The bump at  $m_g/m_p=28$  GeV arises from the fact that over this limit only the luminosity at 31.4 GeV of the beams can contribute [26].

Each stack consisted of a first sheet of nitrocellulose, most sensitive plastic detector, followed by a sheet of polycarbonate (Makrofol E), less sensitive and by two sheets of nitrocellulose. If a monopole candidate would have been found in the first sheet, the following sheets would have been etched and the track followed from one to the next in order to extract maximum information. Each stack was etched according to the standard technique and scanned with microscopes. No candidates were found during scanning. 95% upper limits were calculated using standard methods and the authors obtained the results shown on Figure 31. The final conclusion was that

for monopole masses up to  $30m_p$  and  $n \leq 3$ , if they exist, they are produced with a cross section lower than  $10^{-37} - 10^{-36} \text{ cm}^2$  in proton-proton interactions.

There were two magnetic monopole search experiments performed at the SLAC  $\sqrt{s} = 29$  GeV  $e^+e^-$  accelerator [27, 28]. Flat stacks of NTDs CR-39 (600  $\mu\text{m}$ ) and Lexan (75  $\mu\text{m}$ ) were used in this experiment. Lexan detects only tracks of very highly ionizing particles ( $Z/\beta > 70$ ) and is able to withstand more than 100 Mrad general radiation damage. CR-39 is sensitive to particles with  $Z/\beta > 6$  but cannot tolerate doses above a few Mrads. In the experiment, Lexan was placed closest to the beams, followed by alternating sheets of CR39 and Lexan. The relative location of sheets in a stack was fixed by drilling several holes through it, which makes possible  $< 100 \mu\text{m}$  localization from sheet to sheet. The system was sensitive to electric charge  $3 < Z < 180$  as well as magnetic charge  $0.3g_0 < g < 3g_0$  and mass approaching the beam energy of 14.5 GeV. The experimental search was performed at two different PEP interaction points, IR-10 and IR-6. At IR-10 detectors were positioned directly downstream from the electron injection point. The detector in this area consisted of two modules, each  $3.2 \times 5.7 \text{ cm}^2$ ,  $\sim 0.3 \text{ g/cm}^2$  thick. The modules were exposed to  $8.4 \times 10^{36} \text{ cm}^{-2}$  integrated luminosity at 5 cm from the interaction point, directly under the beam, covering a solid angle of  $\sim 2.0$  sr. The beam pipe was made off 100  $\mu\text{m}$  thick stainless steel. The second detector at the IR-6 was positioned at the no longer used free quark search detector location. The IR-6 area has an elaborated shielding system and therefore the background level was much lower than in the IR-10 area. Two modules were mounted directly above and below of the 200  $\mu\text{m}$  thick stainless steel beam pipe. The modules, each  $15 \times 46 \text{ cm}^2$  covered  $\sim 4.6$  sr solid angle, with a total thickness of  $\sim 1.3 \text{ g/cm}^2$ . The uncertainty in the position of the interaction point was  $\sim 1$  cm in the longitudinal direction and much less in the radial direction. The total integrated luminosity for this exposition was  $6.1 \times 10^{36} \text{ cm}^{-2}$ . After the exposure, sheets were etched and holes were looked for in microscopes with 15x magnification. No candidates were found for highly ionizing particles. One event was recorded which has a nearly normally incident penetrating track in the first two sheets of CR-39 producing a hole. It was identified as an  $\alpha$  particle with initial energy of  $\sim 56$  GeV. This one event is consistent with the estimated event density from particles produced by interactions of energetic hadrons with the beam pipe. The estimated production rate for lithium ions which might be detected in a similar way is lower by 2 orders of magnitude. To estimate an upper limit for the magnetic monopole production, isotropic monopole production was assumed for the reaction  $e^- + e^+ \rightarrow X^+ + X^-$ . The total particle energy was equal to the beam energy. To be observed particles need sufficient kinetic energy to penetrate sheets the CR-39. The authors calculated a charge-mass combinations accessible to the detectors (See Figure 32). The cross section upper limits calculated at 95% level is presented in the Table VI. The cross section limit around  $1 \times 10^{-36} \text{ cm}^2$  was achieved together with a mass limit of 14.5 GeV.

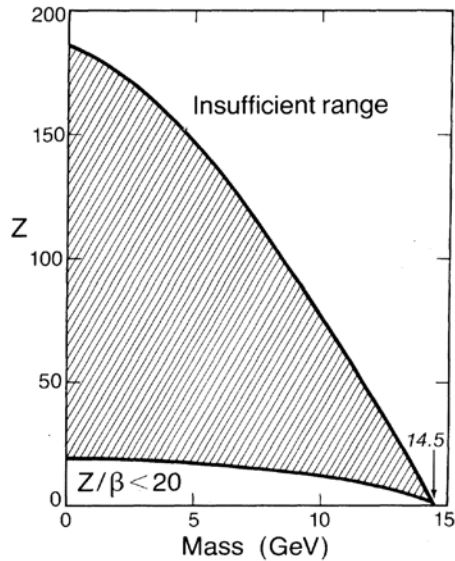


Figure 32. The electric charge and mass combination accessible to the PEP detector [27].

TABLE VI. Experimental parameters and upper limits to production cross sections at 95% CL at  $E_b=14.5$  GeV [27].

	IR-6	IR-10	Combined limit
Integ. Lum. ( $10^{-36}$ cm $^{-2}$ )	6.1	8.4	
Pipe thickness (mm)	200	100	
Magnetic Monopole			
Mass limit (GeV) $g=g_0$	13.7	14.0	
$g=2g_0$	9.5	11.5	
Solid angle (sr)	4.6	2.0	
$\sigma$ ( $10^{-36}$ cm $^{-2}$ )	<1.4	<2.3	<0.85
Electric, $Z/\beta > 20$			
Solid angle (sr)	1.7	1.7	
$\sigma$ ( $10^{-36}$ cm $^{-2}$ )	<3.7	<2.7	<1.6

The experiment at the PEP was done later with increased statistic. Figure 33 shows a schematic view of the detector positioned around the beam pipe for the second PEP monopole search experiment. The data for this experiment was taken only at the IR-10 region at a beam energy of 14.5 GeV, which is the same as in the first PEP experiment. Again Lexan and CR-39 plastic sheets were used. The sheets were 80 and 610-725  $\mu\text{m}$  thick respectively and the array was assembled as shown in Figure 33. A set of holes was drilled in the sheets, which allowed individual sheet alignment to  $\leq 100$   $\mu\text{m}$ . The total solid angle coverage was 5.0 sr. The sheets were 31.8 cm long and had width of 11.8 and 14 cm, as shown in the Figure 33. The 8th side of the octagonally shaped detector was missing and prior to injection and beam tuning, the detector assembly could be rotated away from the beam pipe into a shielded cave located near the floor level. Thus the detector was better shielded from the background in the IR-10 area, due to the neutrons, produced by the uncaptured  $e^-$  injection beam. The data for the analysis were taken using two different loadings of

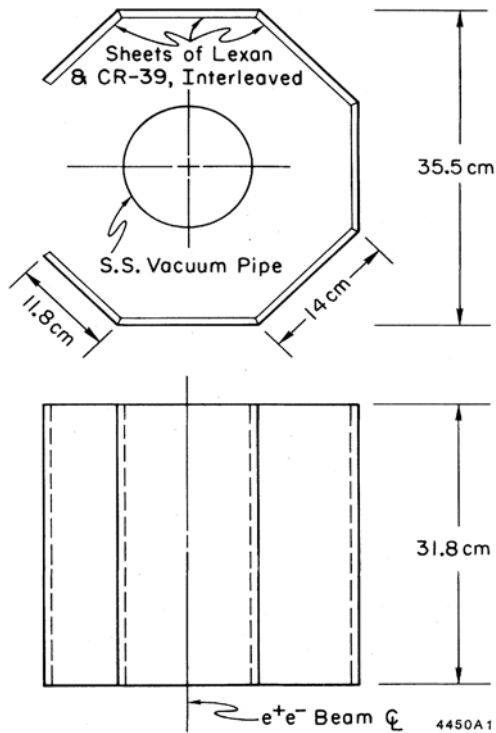


Figure 33. Schematic depiction of Lexan and CR-39 plastic detectors used at the PEP monopole search experiment [28].

the detector assembly. Each loading was exposed during a 9 month period. Integrated luminosities for two runs were  $30.3 \times 10^{36}$  and  $150 \times 10^{36} \text{ cm}^{-2}$ . The data analysis method was the same as in the first PEP experiment. After etching the sheets were inspected with a microscopes for hole observation. The results at the 95% confidence level are presented in a Table VII below, including the previous PEP experiment.

TABLE VII: Summary of experimental parameters and 95% CL upper limits to production cross sections  $E_b=14.5 \text{ GeV}$ ,  $g_0=e/2\alpha=68.5e$ , Dirac charge [28].

	Ref[27]		Run1	Run2	Combined
	IR-6	IR-10	IR-10	IR-10	limit
Int. Lum( $10^{36} \text{ cm}^{-2}$ )	6.1	8.4	30.3	150	
Pipe thickness ( $\mu\text{m}$ )	200	100	200	200	
Magnetic Mass limit (GeV) $g=g_0$	13.7	14.0	13.7	13.7	
Monopole $g=2g_0$	9.5	11.5	9.5	9.5	
Solid angle (sr)	4.6	2.0	6.4	6.4	
$\sigma (10^{-36} \text{ cm}^2)$	<1.4	<2.3	<0.19	<0.039	<0.032
Electric Solid angle (sr)	1.7	1.7	5.0	5.0	
$Z/\beta > 20$ $\sigma (10^{-36} \text{ cm}^2)$	<3.7	<2.7	<1.6	<0.050	<0.041

A search for magnetic monopoles in  $e+e-$  collisions was done at  $\sqrt{s} = 34 \text{ GeV}$  of the PETRA storage rings at DESY[29]. The experimenters realized importance of not having material between the interaction point and the detector. Kapton was used as a detector, which has the ionization threshold, above which tracks can be detected. This threshold is rather high  $dE/dx > 4 \text{ GeV/g cm}^{-2}$

making this material insensitive to the background. Also Kapton has a small degassing rate and it can be exposed inside the vacuum chamber of the storage ring. Monopoles would be detected in these foils by their high ionization rate. After exposure the foils are developed in 15% NaCl solution for 4 hours and any tracks would appear as a holes in the plastic since the etchant preferentially attacks the region of the tracks. The foils are placed between pads soaked with electrolyte and, if a hole were present, electrical contact would be established between the two sides. In order to check that kapton does not lose its detection properties at the conditions inside the storage ring a small piece of kapton, which had previously been exposed to heavy ions, was kept inside the PETRA vacuum chamber for 9 months. No change in its sensitivity was observed. The total integrated luminosity was  $1.9 \text{ pb}^{-1}$ ,  $3.4 \text{ pb}^{-1}$ ,  $89 \text{ pb}^{-1}$ ,  $1.5 \text{ pb}^{-1}$  at CM energies of 14 GeV, 22 GeV, 34.5 GeV and 38 GeV respectively.

After development no hole was found which could be interpreted as being produced by single ionizing particle. In order to compute a limit for the production cross section, the authors assume the following mechanism for the production of a monopole antimonopole pair:  $e^+e^- \rightarrow M^+M^-$ .

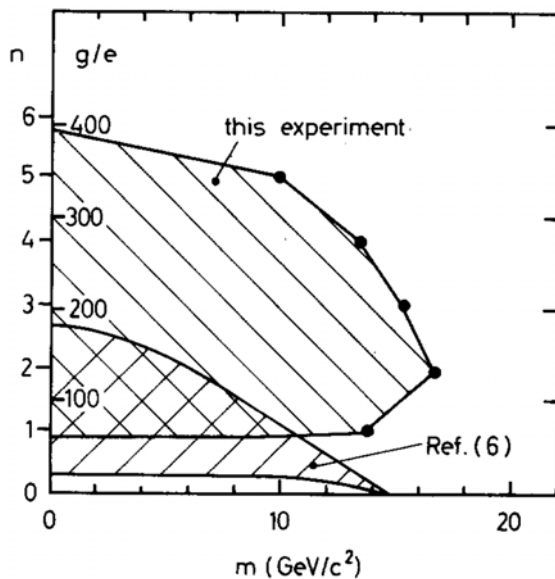


Figure 34. The monopole mass  $m$ , for which this experiment was sensitive, is shown (shaded),  $g$  = magnetic charge of the monopole,  $n$  = magnetic charge of monopole in multiples of the Dirac charge  $(137/2)e$ ; also shown for comparison are the limits obtained by ref. [27].

The energy of the monopole is then equal to the beam energy of the storage ring, and therefore the velocity  $\beta$  of the monopole as function of its mass  $m$  is known. The kapton foils are only sensitive for monopoles above a threshold velocity  $\beta_{th}$ , because the ionization rate is a decreasing function of  $\beta$ . Using the work of ref. [29a] on the ionization rate of monopoles, and a safe value of  $6 \text{ GeV/g cm}^{-2}$  for the sensitivity limit of kapton, one obtains  $\beta_{th} = 0.6$  for  $n = 1$  or  $g = 68.5e$ . For larger values of the magnetic charge, the limit on  $\beta$  is given by the requirement that the monopole should penetrate at least one foil at the largest angle inside the acceptance of the detector. These values of  $\beta_{th}$  were again calculated using ref. [29a]. The values of  $\beta_{th}$ , which depend on the magnetic charge  $g = 68.5en$ , imply upper limits for the mass of a monopole which can be detected. These mass limits are shown in Figure 34 as a function of the magnetic charge. Also

included in fig.34 are the limits obtained in a similar experiment at SLAC [27]. In order to compute an upper limit for the pair production cross section the authors assumed isotropic production of the monopoles. Using only the luminosity above 34 GeV CM energy, one obtains  $\sigma < 4 \times 10^{-38} \text{ cm}^{-2}$  (95% CL). This value can be compared with the limit of  $0.9 \times 10^{-36} \text{ cm}^{-2}$  obtained in a similar experiment at SLAC [27].

A search for highly ionizing particles in  $e^+e^-$  collisions was done at the KEK storage ring TRISTAN [30, 31]. In a first experiment the cms energy was 50 – 52 GeV. In the second experiment the energy was 50 – 60.8 GeV. The detector included two types of etchable solids with well established response, CR-39 plastic and UG-5 glass. The UG-5, formed into a stack of two

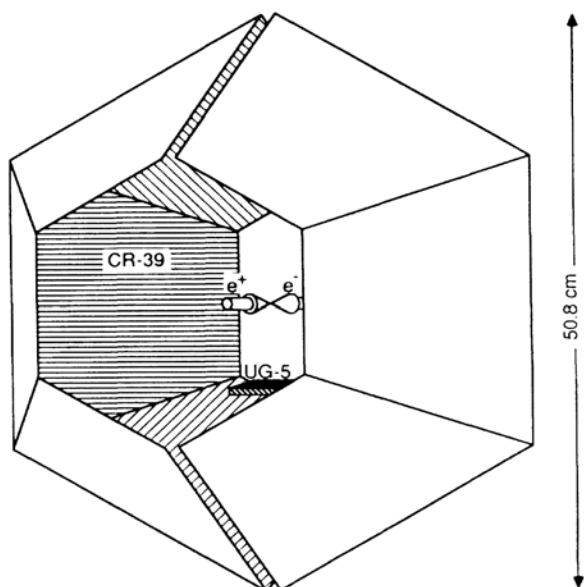


Figure 35. Schematic representation of the CR-39 and UG-5 detector configuration. The UG-5 is inside the vacuum while the CR-39 is outside [30].

Table VIII. Detector parameters, sensitivity, and results for three materials [30].

	CR-39 (A)	CR-39 (B)	UG-5
Initial thickness ( $\mu\text{m}$ )	680	1600	900
(Solid angle)/ $4\pi$	0.40 <sup>a</sup>	0.40 <sup>a</sup>	0.05
Etchant	6.25N NaOH	7N-8N NaOH	49% HBF <sub>4</sub>
Etch temperature ( $^{\circ}\text{C}$ )	50	73-83	70
Etch time (h)	912	30-98	100
Surface removed ( $\mu\text{m}$ )	213	114-1196	35
Scanning technique	Ammonia	Visual, (5-50) $\times$	Visual, 200 $\times$
Minimum $Z/\beta$	25	$\approx 15$	$\approx 85$
$M_c c^2$ (GeV): $g = g_D, 2g_D$	24.1, 13.2	23.3, 7.3	$\dots$ , 22.0
$\sigma_{\text{lim}} (10^{-36} \text{ cm}^2)$ : $g = g_D, 2g_D$	1.6, 1.6	1.6, 2.2	$\dots$ , 13

7.5x7.5 cm<sup>2</sup> sheets, each 0.9 mm thick, placed 7 cm below the interaction point in vacuum. The placement of the detector inside, rather than outside the vacuum chambers expands

significantly the capability to search for particles with short ranges and very high ionization, such as a Dirac monopole with charge  $2g_D$ , which would lose  $\sim 10$  GeV of energy in the 15 mm thick aluminum beam pipe. Outside the vacuum twelve flat stacks of the more sensitive CR-39 were deployed in a polyhedral configuration, to increase a detector acceptance. This shape covers a solid angle of  $\sim 0.9 \times 4\pi$  sr (see Figure 35). Six of the detector faces were populated by 3 sheet stacks of 680  $\mu\text{m}$  thick CR-39 (A) and the other 6 modules consisted of 4-sheet stacks of 1600  $\mu\text{m}$  thick CR-39 (B). The CR-39 stacks were mounted on a movable system, which allows to remove them during beam injection and tuning. Standard methods of etching and looking at sheets via microscopes were implemented. The etching conditions, and scanning techniques together with measured upper limits are summarized in the Table VIII.

No penetrating tracks were found. The 95% confidence upper limit on a cross section for production of highly ionizing particle was calculated taking into account the detection efficiency and the integrated luminosity. Combining the results from the two CR-39 detectors for  $g = g_D$ , authors found a cross section limit of  $8 \times 10^{-37}$   $\text{cm}^2$  for the most accessible masses, which are 24.1 GeV for a charge  $g_D$  and 22.0 GeV for charge  $2g_D$ .

New results were reported from a search for highly ionizing particles at the TRISTAN ring at KEK [31]. The search was sensitive to Dirac monopoles with charge  $g = 68.5e = g_D$  and  $g = 2g_D$ . In subsequent running 25.4  $\text{pb}^{-1}$  of integrated luminosity has been accumulated at  $\sqrt{s} = 55\text{-}60.8$  GeV. Integrated luminosities at the different run energies for all data accumulated are summarized in Table IX. The luminosity in the experiment was measured using a small-angle Bhabha counter based on lead glass calorimeters. A large-angle counter, based also on lead glass and sensitive to scattering angles of  $20^\circ\text{-}50^\circ$ , was used during runs. The ionization produced by magnetic monopoles and the response of track detectors to them is established through calculations analogous to those for electrically charged particles. The ionization rate of magnetically charged particles with velocities  $\beta > 0.1$  is found to be approximately constant and equal to that of a minimum ionizing particle carrying electric charge of the same magnitude. For fast particles carrying greater than  $\sim 0.2g_D$  magnetic charge, solid state track detectors are an effective and inexpensive method of detection. The detectors used in the experiment, the method of etching and the stereo microscope used were the same as in the experiment [30]. No candidates were found in the data collected in this experiment. The authors set a 95%

Table IX. Integrated luminosity, geometrical acceptance  $\Delta\Omega/4\pi$ , and cutoff masses for individual detector sectors at each run energy [31].

Run	$\sqrt{s}$	$\int \mathcal{L} dt$ ( $\text{pb}^{-1}$ )	$\Delta\Omega/4\pi$ , $\mathcal{M}_1 c^2$ (GeV), $\mathcal{M}_2 c^2$ (GeV)		
			CR-39 (A)	CR-39 (B)	UG-5
I	50	0.8	0.40 <sup>a1</sup> , 23.2, 12.1	0.40 <sup>a1</sup> , 22.0, 5.6	0.05, -, 21.0
II	52	4.0	0.40 <sup>a1</sup> , 24.1, 13.2	0.40 <sup>a1</sup> , 23.3, 7.3	0.05, -, 22.0
III	55	4.0	0.43, 25.7, 15.1	0.43, 24.9, 9.9	-
IV	56	7.5	0.43, 26.3, 15.7	0.43, 25.4, 10.6	-
V	57	4.7	0.43, 26.8, 16.4	0.43, 25.9, 11.3	-
VI	58	2.7	0.43, 27.6, 17.2	0.43, 26.7, 12.3	-
VII	60	3.4	0.43, 28.4, 18.1	0.43, 27.5, 13.2	-
VIII	60.8	3.1	0.43, 28.8, 18.5	0.43, 27.9, 13.8	-

confidence limit on magnetic monopole production cross section. The detection efficiency

$\varepsilon$  is a function of particle charge, mass and energy and depends on the geometry of the detector, the sheet thickness, the response of the detector as a function of ionization rate, the scanning method used and the beam pipe thickness. A particle satisfying the ionization criterion is detected with efficiency  $\sim 1$  if it has sufficient energy to penetrate the beam pipe plus two sheets of detector material. Where the efficiency is equal to the geometric acceptance of 0.86, the  $\sigma_{\text{lim}}$  established using all of the data is  $1 \times 10^{-37} \text{ cm}^2$ . The overall efficiency for a particle of a given mass depends on the energy spectrum of the produced particles. In the absence of specific models of production, the authors calculate efficiencies and limits as a function of mass for isotropic, exclusive pair production of Dirac monopoles with charge  $g_D$  and  $2g_D$ . The efficiency is calculated via Monte Carlo simulation as a function of mass and run energy. The cutoff mass  $M_n$  is defined as the mass at which the detector efficiency is half the maximum geometric acceptance, for monopoles with charge  $ng_D$ . The total exposure, geometric acceptance and cutoff masses  $M_{1c^2}$  and  $M_{2c^2}$  for each detector sector are compiled in table above. This search is classified as "direct" in that no assumptions have been made about the properties of the monopole aside from the magnitude and magnetic nature of the charge.

The significance of the limit is depends on the physical process by which the particle is presumed to be produced. For Dirac monopoles the most obvious mechanism is annihilation and pair production via the electromagnetic interaction. If one assumes a single-photon production process, then the amplitude for pair production is proportional to the magnetic charge. Ignoring higher order effects, one can then formulate a naive pair production cross section for monopoles of mass  $m$ ,  $\sigma_D(m)$ , by multiplying the cross section for production of a  $\mu^+ \mu^-$  pair with invariant mass greater than  $2m$  by the square of the charge ratio and making a phase space correction:  $\sigma_D(m) = (g_D/e)^2 \times \sigma_{\mu\mu}(>2m) \times (1-4m^2/s)$ . The phase space term had not been included in previous report. The quantity  $R_D = \sigma(m)/\sigma_D(m)$  then be expected to be of order unity for point-like Dirac monopoles with magnetic charge  $g_D$  (and  $\sim 4$ , for charge  $2g_D$ ), at energies above threshold. In  $e^+e^-$  annihilations the  $\mu$  pair cross section is well approximated by lowest order QED, where they are produced with invariant mass equal to the center of mass energy. In  $pp$  or  $pp^{\bar{}}$  collisions  $\mu$  pairs are produced with a distribution of invariant mass which is well measured for  $pp$  up to  $\sqrt{s} = 60 \text{ GeV}$  and may be extrapolated to higher energies by scaling. Experimental limit on  $R_D$ , accumulated over all runs, is shown in Figure 36 together with other previous searches. From this analysis the authors conclude that point-like Dirac

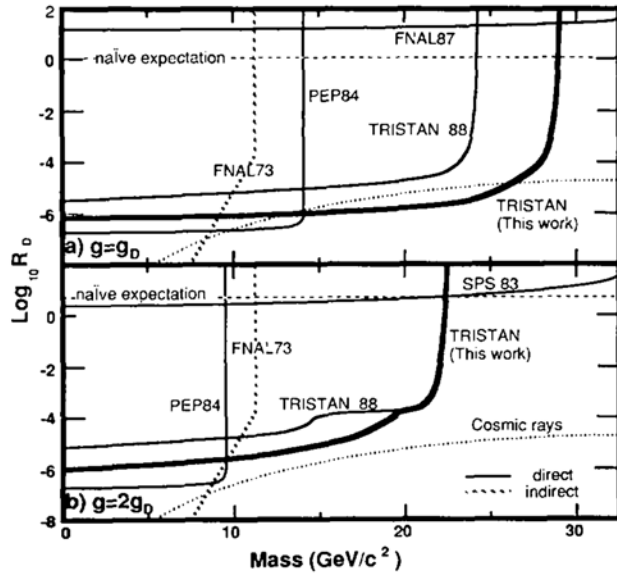


Figure 36. Upper limit at 95% confidence on  $R_D = \sigma(m)/\sigma_D(m)$  for isotropic exclusive production of monopole pairs with charge (a)  $g_D$  and (b)  $2g_D$ . The thick line indicates limit obtained accumulated using all exposures. Both TRISTAN results shown include a phase space correction, as described in the text. Selected limits shown from previous accelerator searches [31a] and from cosmic rays [31b] have not been adjusted for phase space.

monopoles with mass below  $28.8 \text{ GeV}/c^2$  are ruled out.

Two experiments at the CERN LEP  $e^+e^-$  accelerator were performed by the MODAL [32] and OPAL [33] collaborations. The MODAL experiment was run at  $\sqrt{s} = 91.1 \text{ GeV}$  energy. The detector used CR-39 plastic foils covering a  $0.86 \times 4\pi \text{ sr}$  angle surrounding the I5 interaction point at LEP. The polyhedral array was supported by a frame which was mounted on a fixed stand. The aluminum vacuum pipe was a thin of 0.5 mm aluminum. Runs were performed at energies  $\sqrt{s} = 89 - 93 \text{ GeV}$ . The integrated luminosity was accumulated at  $\sqrt{s} = 91.1 \text{ GeV}$  and was  $60 \pm 12 \text{ nb}^{-1}$ . The 12 detector faces were filled with several types of CR-39 material. The thickness were first:  $720 \mu\text{m}$ (A), second:  $1500 \mu\text{m}$  (B), third:  $730 \mu\text{m}$  (C). Detector response of all three plastic detectors were calibrated using heavy ions at the Lawrence Berkeley Laboratory. Table X below shows composition of modules in the two runs of the experiment. In each exposed module the two front sheets, closest to the interaction point, were analyzed.

Table X. Detector compositions and exposure [32].

Run	I		II	
Int. Lum. ( $\text{nb}^{-1}$ )	30 $\pm$ 6		30 $\pm$ 6	
CR-39 type	A	B	C	D
thickness $\mu\text{m}$	720	1500	730	1500
No. modules	3	9	6	6

In all cases at least one of the two front sheets was etched heavily and scanned rapidly, while others were examined if a track passed the scanning criteria. Holes were located by an ammonia technique [32a] or by microscope inspection at low magnification (16x). To calculate general

detection efficiency an isotropic magnetic monopole pair production was simulated with charges  $g_D$  and  $2g_D$ . The acceptance and cutoff mass for each detector is presented in Table XI below.

Table XI. Detector parameters, sensitivity, and results [32].

Module type	I.1	I.2	II.1	I.2	II.2
No. of modules	3	3	6	6	6
NaOH concentration		6.25N		8N/6N	
Etch temperature (°C)		50		80/70	
Etch time (h)	1080	1980	890	150/45	
Surface removed ( $\mu\text{m}$ )	270	560	290	650/50	
Scanning technique		Ammonia		Visual	
$Z/\beta_{\text{thr}}$	20	10	7	10	10
Scanned sheet No.	2	2	1,2	1	1
No. of holes (tracks)	10	1	13	3	1
No. of penetrating tracks	0	1	12	3	1
$\mathcal{M}_1$ ( $\text{GeV}/c^2$ )	44.9	43.8	44.9		43.8
$\mathcal{M}_2$ ( $\text{GeV}/c^2$ )	39.3	32.9	39.2		32.9

During the analysis no candidates for highly ionizing particles were found and the upper limit of the production cross section of such particles at a 95% confidence level was established:  $7 \times 10^{-35} \text{ cm}^2$ . The Dirac magnetic monopoles with masses below  $44.9 \text{ GeV}/c^2$  were ruled out.

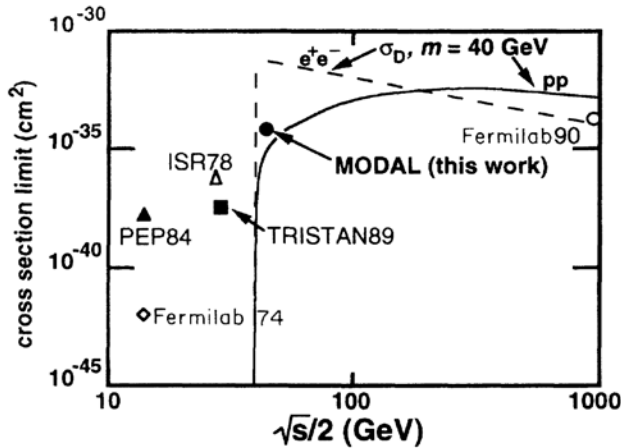


Figure 37. Upper limits at 95% CL on magnetic monopole pair production with a charge  $g$  as a function of  $\sqrt{s}/2$  for MODAL and TRISTAN searches in  $e^+e^-$  collisions. Open symbols are for  $pp$  [17], CERN ISR [26] and  $pp^-$  [23] results.

The magnetic monopole search with the OPAL [33] detector was done at two energy domains of the LEP machine: at LEP1  $\sim 90 \text{ GeV}$  and at LEP2  $\sim 206.3 \text{ GeV}$  [33b]. The OPAL detector was sensitive to Dirac monopoles with magnetic charge in the range  $0.9 g_D < g < 3.6 g_D$ , where  $g_D = 68.5e$ . The OPAL detector, is a general purpose set-up with the main task of  $e^+e^-$  interactions studies at the LEP collider. Monopole detectors based upon plastic track-etch foils, assembled as three sets of three layers of Lexan, were wound around the OPAL beam pipe. Each of the three layered sets of Lexan was spot welded on a mandrel with exactly the same external diameter as the

beam pipe. A set of positioning holes was punched through each three layered Lexan set while it was fixed on the mandrel. In addition, scribe marks were placed on the plastic in order that it could be aligned with positioning marks on the beam pipe. Lastly, surveyor's dots were affixed to allow the CERN surveying team to measure the position of the foils with respect to the beam pipe. In addition, two aluminized Lexan sheets formed the gas seal and the inner HV foil for the OPAL vertex chamber. The lexan sheets deployed were all 0.125 mm in thickness. The geometric acceptance of this configuration was  $\sim 0.99 \times 4\pi$  sr, and its total incremental thickness comprised 0.09% radiation lengths of material. The beam pipe was composed of aluminum and carbon fiber with a total thickness of 1.4 mm.

Lexan was deployed in the OPAL experiment from October 1989 to December 1990. In this interval the detector was exposed to  $8.67 \text{ pb}^{-1}$  of integrated luminosity at the OPAL intersection region. The first three layers of lexan immediately surrounding the beam pipe were then removed, sensitized by exposure to ultraviolet light [32a] and etched. The passage of such a highly ionizing particle through a dielectric track detector, or plastic track-etch detector, is revealed as a cone shaped etch pit when the surface of the plastic is etched in a controlled manner using hot concentrated sodium. The thickness removed from each surface was  $40 \mu\text{m}$  and  $20 \mu\text{m}$  from the first and second sheets, respectively. The sheets were then scanned using an ammonia technique [32a] to locate holes which would be produced by tracks with sufficiently high ionization. Four holes originating from tracks were found in the front sheets, and none were found in the second sheets. The extrapolated track locations in the adjacent sheets were examined for tracks, and none were found.

The detection efficiency calculation was done for magnetic monopoles of charge  $g_D$  and  $2g_D$  assuming isotropic and exclusive pair production, and taking into account the magnetic field and the geometrical acceptance and energy losses in the beam pipe and detector, and etching and scanning criteria. The physical mechanism for Dirac magnetic monopole production assumed annihilation and pair production via the electromagnetic interaction. If a single-photon production process is assumed, then the limit may be compared with a lowest-order cross section  $\sigma_D(m)$  for a point like monopole of mass  $m$  [30,31], which scales with the cross section for unlike-sign dimuons:  $\sigma_D(m) = (g_D/e)^2 \times \sigma_{\mu\mu}(>2m) \times (1-4m^2/s)$ . Obtained limits can then be expressed as limits on the quantity  $R_D = \sigma(m)/\sigma_D(m)$  which would be expected to be of order unity for point like Dirac monopoles with magnetic charge  $g$ , at energies above threshold. Obtained limits on  $R_n$  are shown in fig. 36 along with the most stringent limits from previous searches. The point like cross-section used here is a  $\sigma_{\mu\mu}^{\text{QED}} = 86.8/E_{\text{cm}}^2 \text{ nb}$ , where  $E_{\text{cm}}$  is the centre of mass energy. The 1989-1990 energy scan of the  $Z^0$  resonance covered the energy range:  $88.23 \text{ GeV} < E_{\text{cm}} < 94.28 \text{ GeV}$ . The corresponding variation in point like cross-section is  $11.2 \text{ pb} < \sigma_{\mu\mu} < 9.8 \text{ pb}$ : approximately 50% of the luminosity taken with  $91.2 \text{ GeV} < E_{\text{cm}} < 91.3 \text{ GeV}$ . The luminosity weighted average point like cross section of  $10.4 \text{ pb}$  is taken to be the characteristic cross section  $\sigma_D(m)$ . From this analysis, the authors conclude that monopoles with mass below  $45.0 \text{ GeV}/c^2$  are ruled out. However, it has been speculated that monopoles may have non point like structure, resulting in a suppression of the production cross-section by many orders of magnitude by form factor effects [33a]. This result is able to rule out suppression factors of less than  $5 \times 10^4$  at 95% confidence. As there are no candidates for highly ionizing elementary particles, the upper limit on the cross section for production of such particles at 95% confidence level is  $\sigma < 3/(\epsilon L t)$  where  $L t$  is the integrated luminosity and  $\epsilon$  the detector efficiency. Where the efficiency is equal to the maximum acceptance, and cross section limit is  $3 \times 10^{-37} \text{ cm}^2$  and mass limit  $< 45 \text{ GeV}/c^2$ .

The magnetic monopole search was done at the LEP2 accelerator at  $\sqrt{s} = 203.6$  GeV energy [33b]. Figure 38 shows the OPAL detector, which used a cylindrical jet chamber for the magnetic monopole detection. The Jet Chamber (CJ) used for tracking in OPAL, was able also

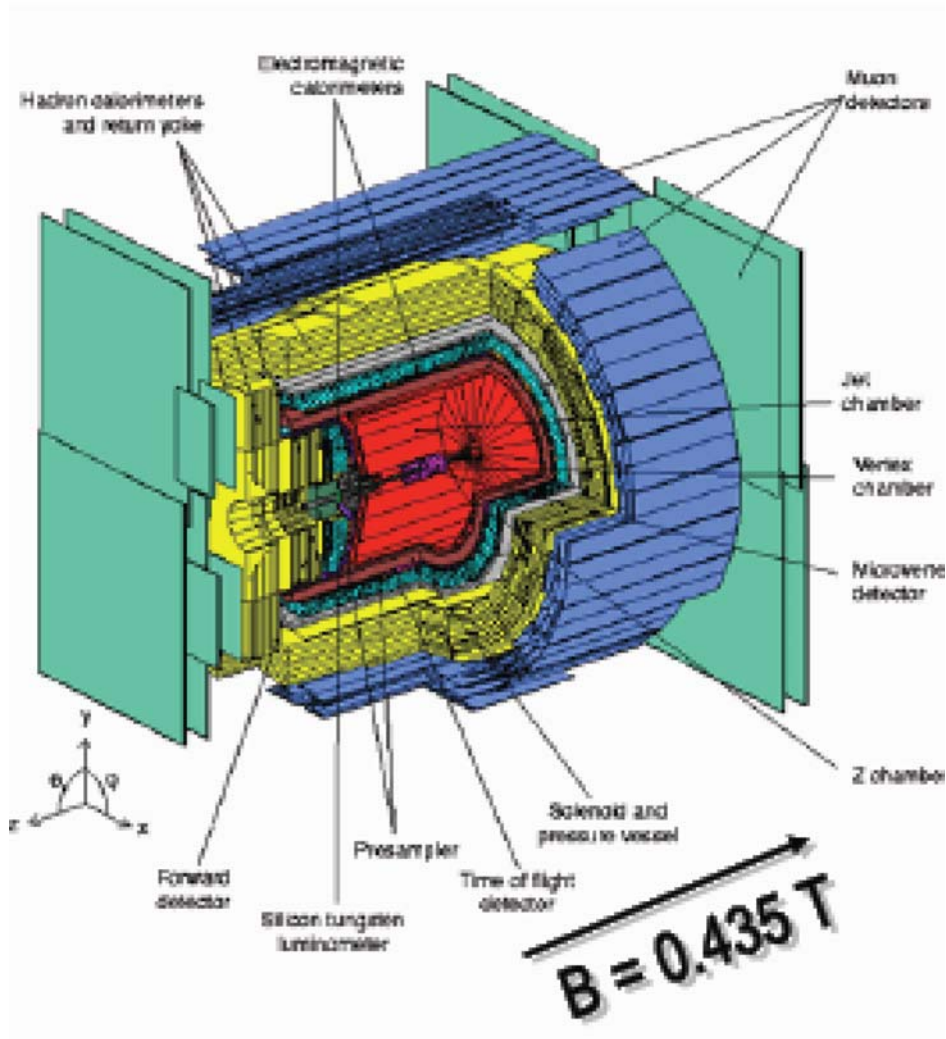


Figure 38 OPAL detector at CERN LEP2 experiment.

to measure particle momentum and  $dE/x$  as well. Back to back tracks with high energy release were searched for in opposite CJ. No corresponding signals were found in data of  $63 \text{ pb}^{-1}$  integrated luminosity. Figure 39 shows simulated charge per hit in the OPAL Jet Chamber produced by usual particles (blue histogram) and measured (black points), and a simulation of the signal from magnetic monopoles (pink histogram). Detector simulation was done for efficiency determination. The obtained upper limit on the magnetic monopole production cross section is shown in figure 40. A cross section limit of  $5 \times 10^{-39} \text{ cm}^2$  was achieved for monopole masses in the  $45 - 100 \text{ GeV}/c^2$  region.

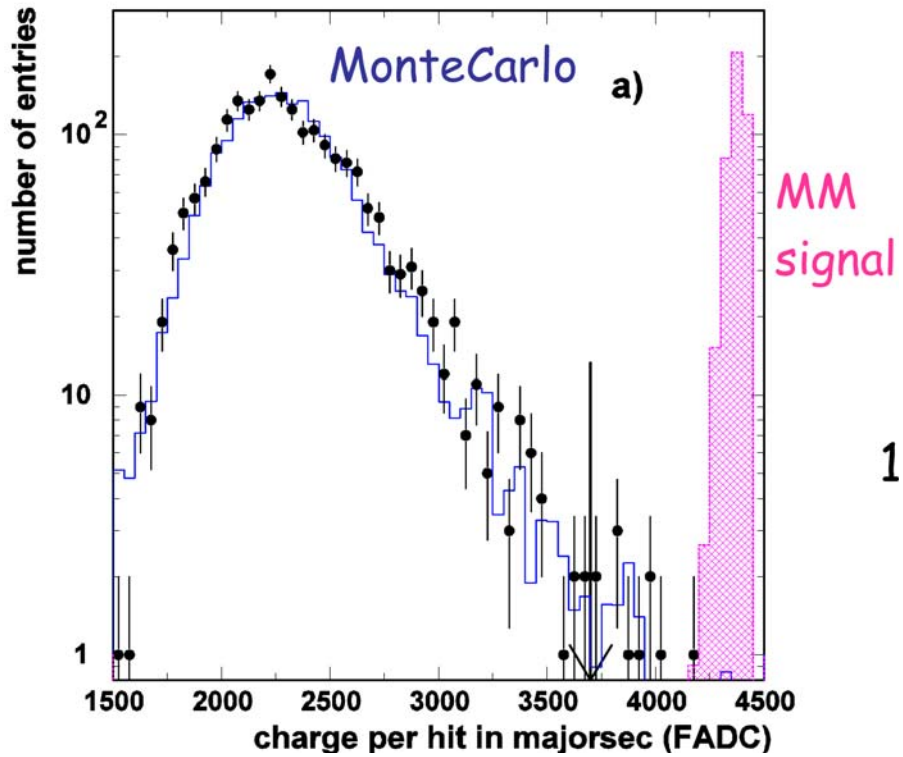


Figure 39. OPAL Jet Chamber signals for simulated magnetic monopoles (pink), standard particles (blue histogram) and data (black points) [33b].

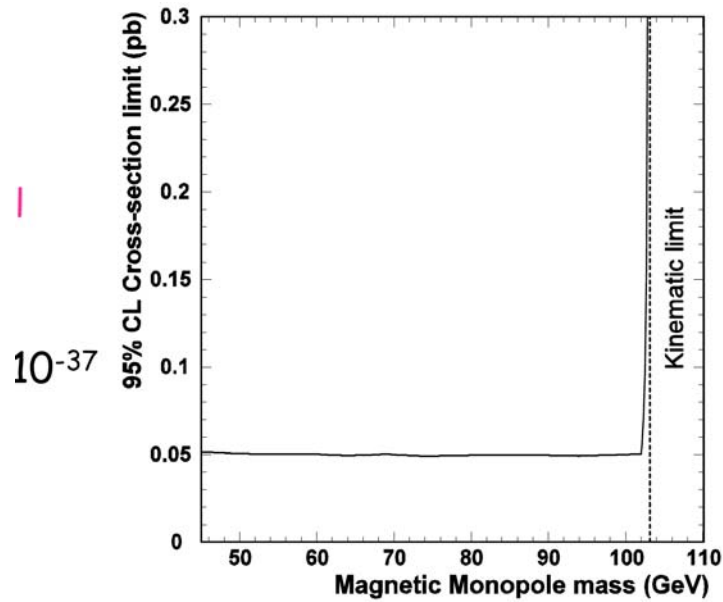


Figure 40. Monopole production cross section limit obtained at the LEP2 OPAL detector at  $\sqrt{s} = 203.6$  GeV energy [33b].

The last direct magnetic monopole search experiment was published in 2006 [34]. This search uses a  $35.7 \text{ pb}^{-1}$  sample of  $pp^{-}$  collisions at  $\sqrt{s} = 1.96 \text{ TeV}$  produced by the Fermilab Tevatron and collected by the CDF II detector during 2003 using a special trigger. The detector (see Figure 41) consists of a magnetic spectrometer including silicon strip and drift-chamber tracking detectors and a scintillator time-of-flight system, surrounded by electromagnetic and hadronic calorimeters and muon detectors. CDF uses a superconducting solenoid to produce a 1.4 T magnetic field. The field is parallel to the beam direction, which is taken as the  $z$  direction, with  $\theta$  the azimuthal angle, and  $r$  the radial distance in the transverse plane. The important detector components for this search are the central outer tracker (COT) and the time-of-flight (TOF) detector, both positioned inside the solenoid. The coverage of the cylindrical COT extends from a radius of 40 to 137 cm and to pseudorapidity  $|\eta| \sim 1$ . The COT consists of eight super layers, each containing 12 layers of sense wires. The COT makes position measurements for track reconstruction as well as integrated charge measurements for determining a particle's ionization energy loss  $dE/dx$ . The COT is surrounded by 216 TOF scintillator bars, which run parallel to the beam line and form a cylinder of radius 140 cm. Each TOF bar is instrumented with a photomultiplier tube (PMT) on each end. The TOF measures both the time and height of PMT pulses; the pulse height is typically used to correct for discriminator threshold time slewing. Due to their large ionization and production of  $\delta$  rays, monopoles in scintillator with velocity  $\beta > 0.2$  are expected to produce more than 500 times the light in the scintillator as produced by a minimum ionizing particle (MIP).

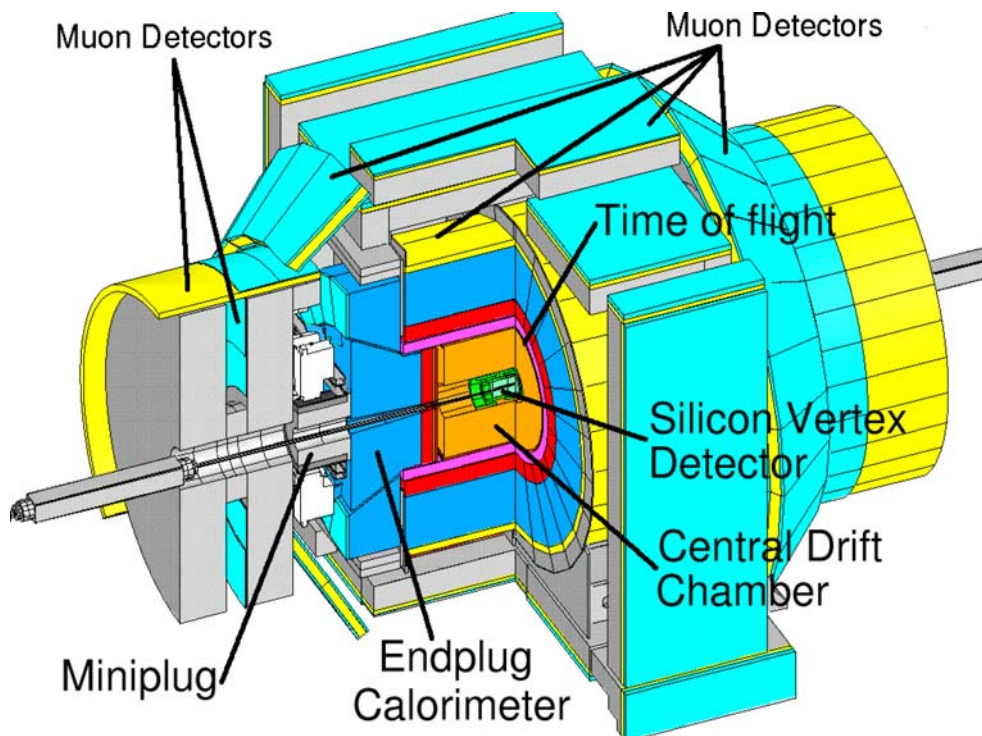


Figure 41. Schematic view of the FermiLab CDF experimental set-up.

The experiment used a highly ionizing particle trigger that requires large light pulses at both ends of a TOF scintillator bar. The trigger was designed to detect monopoles efficiently while consuming less than 1 Hz of the CDF data acquisition bandwidth. The continuous low rate

operation allowed the authors to validate the trigger performance for the entire data sample. The electronics response of the TOF was calibrated to account for nonlinearities and channel-to-channel differences. The trigger thresholds of about 30 MIPs are well below the expected response to a monopole and have a negligible effect on the trigger efficiency.

In the CDF detector, a monopole is accelerated along the uniform solenoidal magnetic field in a parabola slightly distorted by relativistic effects. Because no other particle mimics this behavior, the TOF acceptance must be estimated from Monte Carlo simulations. The authors extended the GEANT3 simulation [34a] to handle magnetic monopoles, including the acceleration by the magnetic field, energy loss, and multiple scattering [34b]. Bremsstrahlung is not simulated as this is a negligible effect for monopoles in the mass range of interest.

The TOF acceptance for monopole pairs simulated with GEANT is shown in Figure 42. Light monopoles, accelerated strongly by the magnetic field, tend to be swept out of the detector before reaching the TOF. Heavy monopoles, produced near threshold, suffer the same fate.

13000 events were selected which passed trigger requirements. Detailed analysis of these events doesn't show a single case that can be considered as a magnetic monopole candidate. Therefore the authors reported a limit of the cross section as a function of the magnetic monopole mass. The expected number of events  $N$  from a process with cross section  $\sigma$  and detector

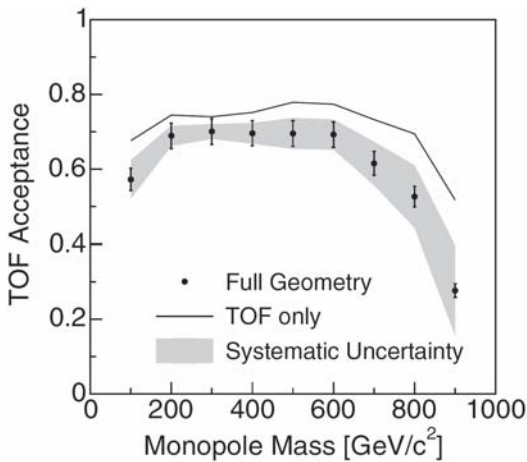


Figure 42. The acceptance of the TOF for monopole pairs, as a function of monopole mass, for Drell-Yan monopole pair production. The band indicates the total systematic uncertainty [34].

efficiency with acceptance  $\epsilon$  after integrated luminosity  $L$  is given by  $N = L\epsilon\sigma$ . The authors calculated the cross-section limit for zero observed events, based on the efficiency summarized in Table XII below and a 6% uncertainty in the luminosity measurement [34c]. The cross-section exclusion limit is shown in Figure 43. The measured limit excludes monopole pair production for cross sections greater than 0.2 pb at the 95% confidence level for monopole masses between 200 and 700 GeV/c<sup>2</sup>. For the Drell-Yan mechanism, this implies a mass limit of  $m > 360$  GeV/c<sup>2</sup> at the 95% confidence level. This is currently the best limit from a direct search.

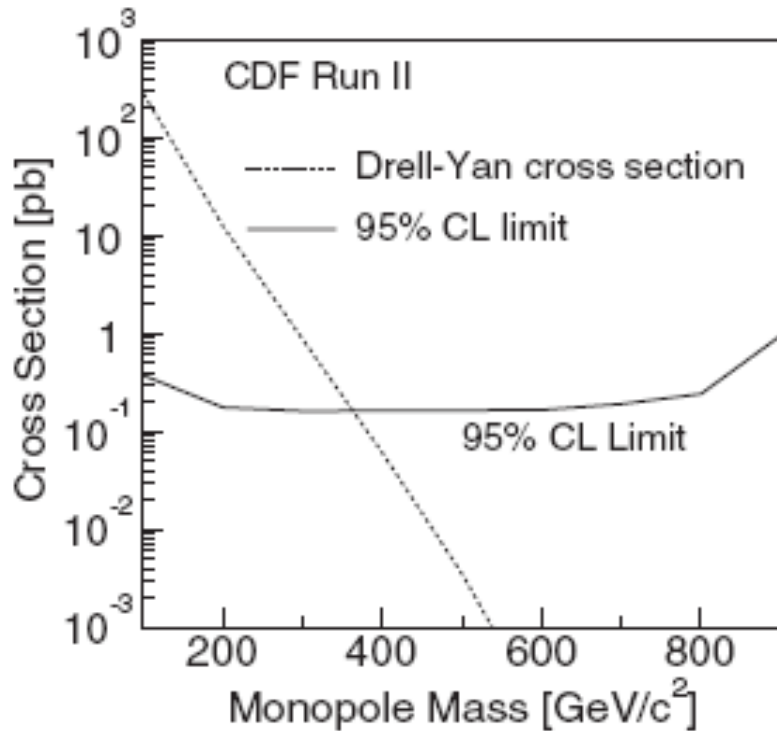


Figure 43. The 95% CL cross-section upper limit versus magnetic-monopole mass. The theory curve for Drell-Yan monopole pair production intersects at the mass limit  $m > 360 \text{ GeV}/c^2$  [34]. The cross-section limit is 2 orders of magnitude more stringent than the results of a previous direct search in this energy range [23].

Table XII. Efficiency of the monopole search with statistical and systematic uncertainties for monopole mass of  $400 \text{ GeV}/c^2$ . The full mass dependence was accounted in the limit.

Effect	Efficiency
TOF geometric (MC)	$70\% \pm 3\% \pm 3\%$
TOF response	100%
TOF spoilers	$98\% \pm 1\% \pm 3\%$
TOF timing (MC)	$99\% \pm 1\% \pm 1\%$
COT width cut	100%
COT segment finding	$94\% \pm 1\% \pm 3\%$

#### 4. Magnetic monopoles in virtual process

We will now consider experiments where magnetic monopoles are created as virtual particles in calculations of the appropriate processes. Those process are  $g-2$ ,  $Z \rightarrow \gamma\gamma$  and the process of production of two photons with high transverse momenta by the collision of two photons produced either from  $e^+e^-$  or  $q\bar{q}$  collisions.

A lower mass limit of 120 GeV for a Dirac monopole has been set in reference [35], based on the monopole contribution to the vacuum polarization correction to the muon anomalous magnetic moment, (see Figure 44), where higher order muon-monopole interaction and monopole anti-monopole interaction diagrams are shown. Actually, the correct mass limit is 60 GeV (see for example [43]). This result is based on a measurement of the muon anomalous magnetic moment performed at CERN [35a, 35b], with  $a_\mu^{\text{exp}} = 11659240(85)10^{-10}$ . The latest result obtained at the BNL AGS experiment [36], is  $a_\mu^{\text{exp}} = 11659208.0(5.4)10^{-10}$ . Based on this result, calculations of the magnetic monopole mass give a lower limit of  $m > 240 \text{ GeV}/c^2$ .

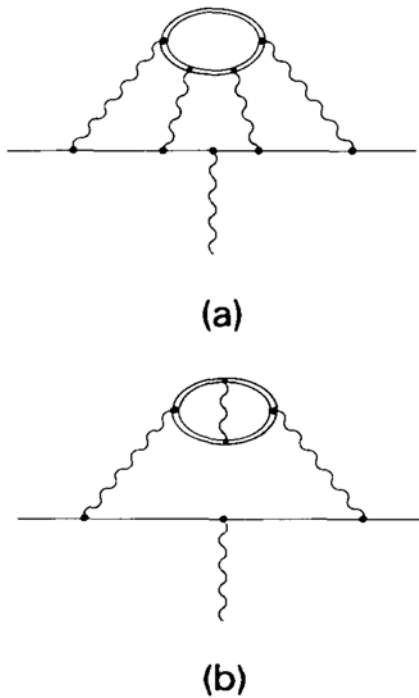


Figure 44. (a) Higher order muon-monopole interaction. (b) Higher order monopole-anti-monopole interaction [35].

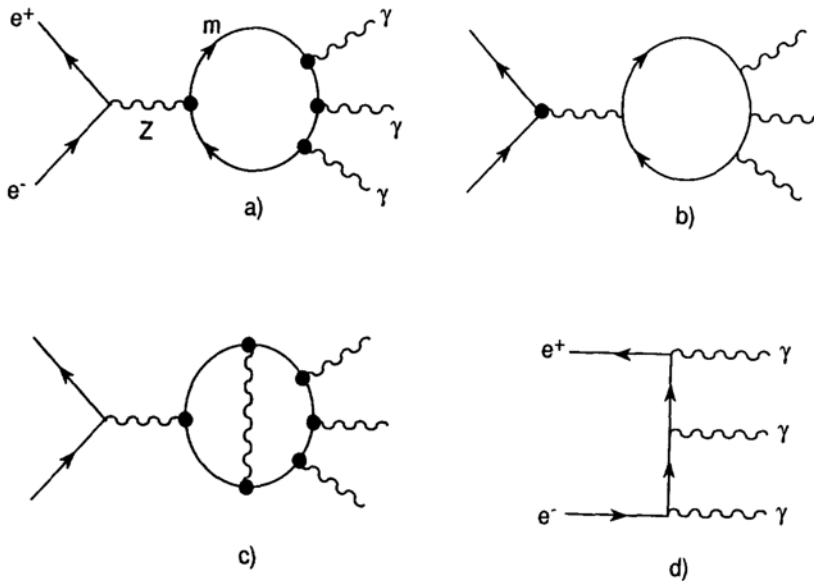


Figure 45. Z-production in  $e^+e^-$  annihilation and monopole-induced  $Z \rightarrow 3\gamma$  decay. (a) With the dual photon vertices (denoted by a heavy dot) hooked to the monopole line and the standard vertex on the electron line. (b) A dual vice versa. (c) A higher-order correction to (a). (d) The QED background [38].

The experiment L3 at the LEP CERN [37] searched for Z decaying directly into three photons. This process was not found, but 95% CL limit of  $1 \times 10^{-5}$  was obtained. The calculations of this process in references [38, 43] (see Figure 45), rule out the magnetic monopole mass up to around  $400 \text{ GeV}/c^2$ .

Another virtual process where monopoles are involved was studied by Ginzburg and Panfil in 1982 [39] and Ginzburg and Schiller in 1999 [40, 41] (see Figure 46). The production was considered of two photons with high transverse momenta by the collision of two photons produced either from  $e^+e^-$  or  $q\bar{q}$  collisions. A virtual heavy point like Dirac magnetic monopoles could re-scatter pairs of nearly real photons into the final state via a box monopole diagram as shown in Figure 46.

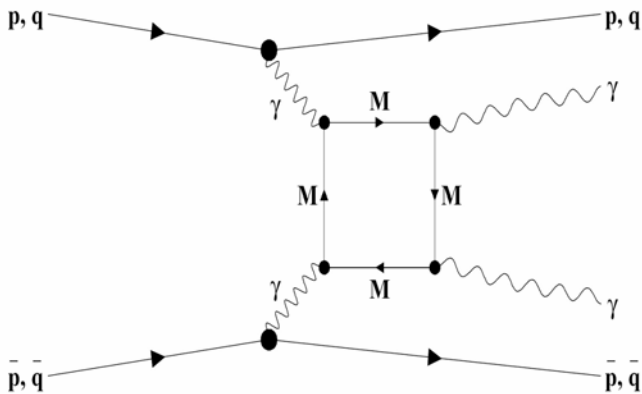


Figure 46. Feynman diagram for  $\gamma\gamma$  production via a virtual monopole loop [41].

Based on this theoretical scheme, an experimental limit was given by the D0 collaboration [42],

which sets the following bounds on the monopole mass  $M$ :  $M/2|m'| > 610$  GeV for  $S=0$ ,  $> 870$  GeV for  $S = \frac{1}{2}$  and  $> 1580$  GeV for  $S = 1$ , where  $S$  is the spin of the monopole, and  $m' = eg$  is the magnetic charge quantization number.

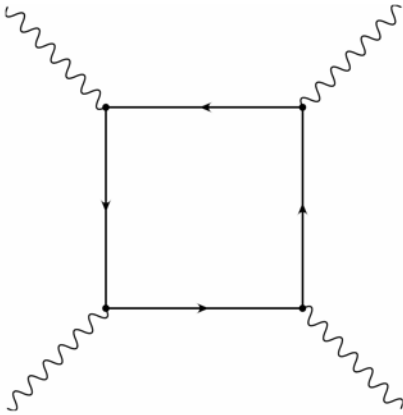


Figure 47. The light-by-light scattering graph for either an electron or a monopole loop [43].

The three processes we considered above rely on the Feynman diagram shown in figure 47. If the particle in the loop is an ordinary electrically charged electron, this process is well known. If, further, the photons involved are of very low momentum compared with mass of the electron, then the result may be simply derived from the well-known Euler-Heisenberg Lagrangian [44-46], which for a spin-1/2 charged-particle loop in the presence of weak homogeneous electric and magnetic fields is:  $L = -F^2/16\pi + \alpha^2/360 \times 1/m^4 \times 1/(4\pi)^2 \times [4(F^2)^2 + 7(F*F)^2]$  where  $m$  is the mass of the particle in the loop. The Lagrangian for a spin-0 and spin-1 charged particle in the loop is given by a similar formula, which is derived in references [46, 47]. Given this homogeneous-field effective Lagrangian, it is a simple matter to derive the cross section for the  $\gamma\gamma \rightarrow \gamma\gamma$  process in the low energy limit. Explicit results for the differential cross section are given in [43]:  $ds/d\Omega = 139/32400 \pi^2 \times \alpha^4 \times \omega^6/m^8 \times (3 + \cos^2 \theta)^2$  and the total cross section for a spin-1/2 charged particle in the loop is  $\sigma = 973/10125 \pi \times \alpha^4 \times \omega^6/m^8$ ;  $\omega/m \ll 1$ ,  $s = 4\omega^2$ . The numerical coefficients in the total cross section are 0.00187, 0.0306 and 3.50 for spin 0, spin 1/2, and spin 1 particles in the loop, respectively. The applicability of the above calculations of the photon scattering through a monopole loop seems impossible because of the existence of the string, which renders perturbation theory meaningless. This box diagram was calculated by A. De Rujula [38] and Ginzburg [40] appealing to duality, which is the dual symmetry of Maxwell equation with respect to the transformations  $E \rightarrow M$ ,  $M \rightarrow -E$ . The introduction of magnetic charge brings in Maxwell equation symmetry with respect to the  $E \rightarrow B$ ,  $B \rightarrow -E$  transformations, as for charges and currents too. For low energy  $\gamma$  processes it is enough to calculate the fermion loop graph in the presence of zero-energy photons, in the presence of static, constant fields. Since the Euler-Heisenberg Lagrangian is invariant under the duality substitution on the fields alone, this means we obtain the low energy cross section  $\sigma_{\gamma\gamma \rightarrow \gamma\gamma}$  through the monopole loop from the equation for the QED cross section by the substitution  $e \rightarrow g$ , or  $\alpha \rightarrow \alpha_g = 137 m'$ .  $2|m'| = 1, 2, 3, \dots$

It is critical to emphasize that the Euler-Heisenberg Lagrangian is an effective Lagrangian for calculations at the one fermion loop level for low energy, i.e.  $\omega/m \ll 1$ . However, it becomes unreliable if radiative corrections are large. The same has been noted in another

context in other works [48-52]. The internal radiative correction to the box diagram have been computed by [50] and [51,52] in QED. In the  $O(\alpha^2)$  term in the expansion of the Euler Heisenberg Lagrangian (see above), the coefficients of  $(F^2)^2$  and  $(F^*F)^2$  terms are multiplied by  $(1 + 40/9 \times \alpha/\pi + O(\alpha^2))$  and  $(1+1315/252 \times \alpha/\pi + O(\alpha^2))$ , respectively. The corrections become meaningless when we replace  $\alpha \rightarrow \alpha_g$ .

In Ref. [43] it was emphasized that there is a problem arising with the unitarity bound. The results given in [40, 41] and used in the analysis [42] seem incorrect. If higher order effects are involved, it seems that the mass limits quoted are inconsistent. If one takes the cross section given by  $\sigma = 973/10125\pi \times \alpha^4 \times \omega^6/m^8$  and makes the duality substitution, one obtains  $\sigma_{\gamma\gamma \rightarrow \gamma\gamma} = 973/10125\pi \times \alpha^4 \times \omega^6/m^8 = 1.08 \times 10^7 \times m^8 \times 1/M^2 \times (\omega/m)^6$  for the low energy light-by-light scattering cross section in the presence of a monopole loop (M is the monopole mass). If the cross section were dominated by a single partial wave of angular momentum J, the cross section would be bounded by  $\sigma < \pi(2J+1)/s \sim 3\pi/s$ , at  $J \sim 1$ . Comparing this with the cross section given above, one obtains the following inequality for the cross section to be consistent with unitarity:  $M/\omega > 6|m'|$ . At the same time the limits quoted by D0 for the monopole mass are less than this:  $M/2|m'| > 870 \text{ GeV}$ , spin  $1/2$ , because, at best, a minimum estimate is  $\langle \omega \rangle \sim 300 \text{ GeV}$ , so the theory cannot sensibly be applied below a monopole mass of about 1 TeV. (Note that changing the value of J in the unitarity limits has very little effect on the bound since an 8th root is taken: replacing J by 50 reduces the limit only by 50%.)

Similar remarks can be directed towards the limits in reference [38]. The author, however, notes the “perilous use of a perturbative expansion in g”. However, although he writes down the correct vertex, he does not, in fact, use it, instead appealing to duality, and even so author admittedly omits enormous radiative corrections of  $O(\alpha g)$  without any justification other than what is believed, is a specious reference to the use of effective Lagrangian techniques for these processes.

The Table XIII below summarizes obtained magnetic monopole mass limits in the processes where monopoles are considered as virtual particles. Experimental results [36, 37] and [42] are excluding monopole masses below 610 GeV, 870 GeV and 1580 GeV depending on spin of the magnetic monopole. Nevertheless, all above mentioned processes are suffering from a problem of higher order corrections, and additional experimental verifications of these results are required.

Table XIII. Magnetic monopole mass limits in g-2, Z  $\rightarrow \gamma\gamma\gamma$  and High Pt  $\gamma$ 's measured in different experiments [36, 37 and 42].

Process	Mass Limit, GeV	Reference
g-2	> 240	35, 36, 43
Z $\rightarrow \gamma\gamma\gamma$	> 400	37, 38, 43
High Pt $\gamma$	> 610 S=0	39 – 43
High Pt $\gamma$	> 870 S=1/2	39 – 43
High Pt $\gamma$	> 1580 S=1	39 - 43

## 5. Future magnetic monopole search experiments

Now we will consider future magnetic monopole search experiments. We will start with the MOEDAL experiment [53] at the CERN LHC accelerator complex [54]. CERN LHC – a large hadron collider - will operate an energy of  $\sqrt{s} = 14$  TeV in the proton-proton mode and will accelerate Lead heavy Ions to  $\sqrt{s} = 5.5$  TeV energy per nucleon. The proton-proton expected luminosity will reach  $1 \times 10^{34} \text{ cm}^2 \text{ s}^{-1}$  and there is an LHC upgrade project with tenfold luminosity increase. With this unprecedented energy and luminosity scale there is a big challenge to look for the magnetic monopoles to cover higher mass regions of a few TeV. Figure 48 gives

### LHC MOEDAL Monopole Search experiment

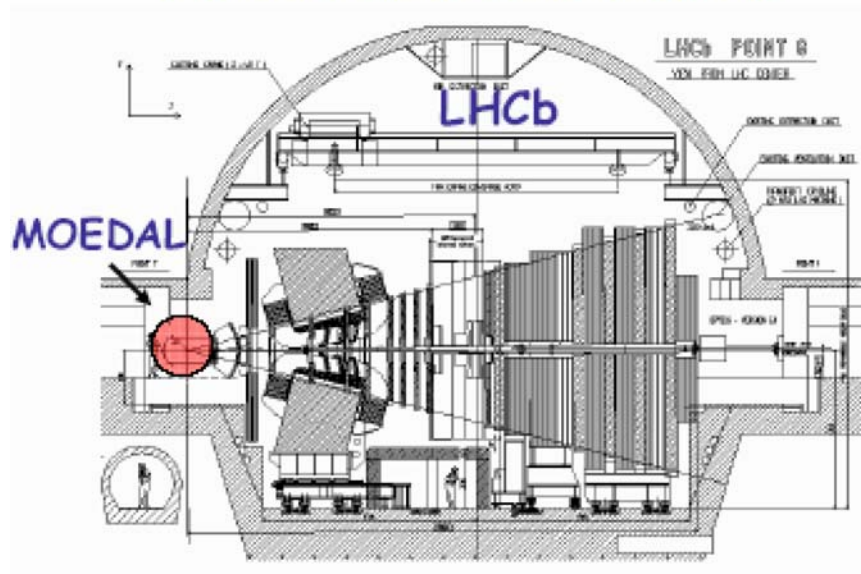


Figure 48. The LHCb experiment with MOEDAL detector at the CERN LHC accelerator [53].

a schematic view of the LHCb experimental set-up, where the MOEDAL experiment will run. The MOEDAL detector consists of NTDs, which will be mounted on a light aluminum frame. It will contain five plastic sheets per triangle element (Lexan – CR-39 – Lexan – CR-39 – CR-39 – Lexan), with a total thickness  $\sim 5$ mm (see Figure 49). Alignment of the monopole track

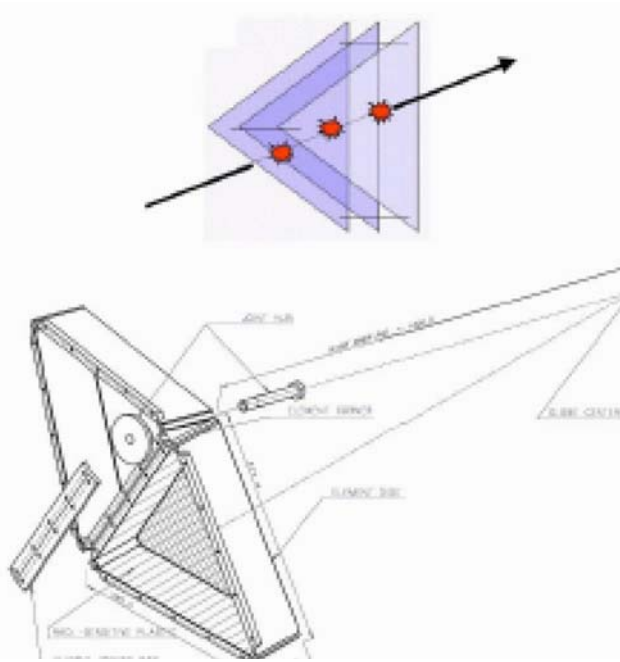


Figure 49. Schematic view of the MOEDAL Nuclear Track Detector construction [53].

within the module will be done by dowel pins and will be good to  $\sim 20 \mu\text{m}$ . All triangular elements do not have to be installed. The design allows for access panels to reach the LHVb vertex vacuum region.

The frame holds plastic, so that tracks are as normal as possible to the plastic and reconstructed tracks can be pointed to the detector. In addition the authors are planning on using high radiation resistant glass detector UG-5, successfully used in TRISTAN and Fermilab experiments, to be use in MOEDAL project. This depends on available space dictated by the main LHCb setup and will be decided later. The authors have calculated the sensitivity of their detector to magnetic monopoles. They used a Drell-Yan mechanism for monopole pair production. They used lower energy results on the Drell-Yan process and extrapolated to the LHC energies. The extrapolation expression is:  $d\sigma/dm dy|_{y=0} = 44 \times 10^{-30}/s^{3/2} \times e^{-25.3m/\sqrt{s}} \text{ cm}^2/\text{GeV}/c^2$ . To obtain the cross section for monopole pair production with mass  $M = x (s/2)^{1/2}$ , the authors integrated the above expression above  $m=2M$ . Assuming no phase space suppression:  $\sigma(M) = (68.5)2 \times 1.74/s \times e^{-25.3m/\sqrt{s}} \times 10^{-30} = 4.2 \times 10^{-35} \times e^{-25.3m/\sqrt{s}}$ . Running for one year ( $10^7 \text{ s}$ ) at a luminosity  $5 \times 10^{32} \text{ cm}^2 \text{ s}^{-1}$  the search sensitivity is  $\sim 1 \times 10^{-40} \text{ cm}^2$  which corresponds to single event production with a mass of 3.5 TeV.

Now we present an experiment, which intends to search for magnetic monopoles at the Relativistic Heavy Ion Collider (RHIC) [55]. We use the one property of the magnetic monopole that defines it, its quantized magnetic charge, to detect it. Hence we make no assumptions, as all previous accelerator based searches have done, about either the mass, binding energy to nuclei, velocity, or the magnitude of the charge of the monopole in designing our detector. We accomplish this by having no material between the point of production of monopoles and the magnetic detector. Our detector uses a superconducting inductive loop, arranged in a gradiometer geometry, which is coupled to a superconducting quantum interference device (SQUID). The SQUID responds to the current induced by the magnetic charge of a monopole and measures directly its magnitude. Pairs or more of these detectors provide for coincident

detection schemes to rule out spurious magnetic signals. In addition, a silicon detector is placed behind the gradiometers and is used to monitor and measure the energy loss of particles produced by collisions. Figure 50 shows the detector which will be installed at the RHIC.

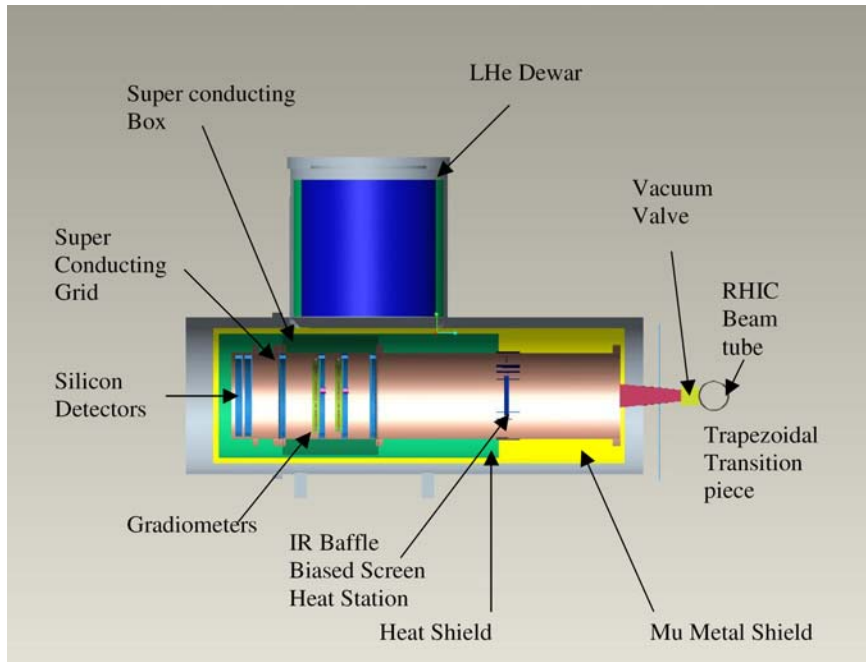


Figure 50. Cross Section of the monopole detector cryostat [55].

The RHIC has two operation modes: Heavy Ions, mainly Gold-Gold (Au-Au) and polarized protons at the energy 100 GeV/nucleon and 100 GeV, respectively. The following integrated luminosities are expected at the RHIC collider [56] in the years 2007 and 2008: (see Table XIV).

Table XIV: Maximum luminosities that can be reached after a sufficiently long running period.

Mode	No of bunches	Ions/bunch [ $10^9$ ]	$\beta^*$ [m]	Emittance [ $\mu\text{m}$ ]	$\mathcal{L}_{\text{peak}}$ [ $\text{cm}^{-2}\text{s}^{-1}$ ]	$\mathcal{L}_{\text{store avg}}$ [ $\text{cm}^{-2}\text{s}^{-1}$ ]	$L_{\text{week}}$
Au-Au	111	1.1	0.9	15-40	$36 \times 10^{26}$	$8 \times 10^{26}$	$290 \mu\text{b}^{-1}$
Cu-Cu	111	6	0.9	15-30	$12 \times 10^{28}$	$4 \times 10^{28}$	$14 \text{nb}^{-1}$
Si-Si	111	12.5	0.9	15-30	$50 \times 10^{28}$	$17 \times 10^{28}$	$60 \text{nb}^{-1}$
d-Au	111	140d/1.1Au	1.5	15-30	$30 \times 10^{28}$	$7.5 \times 10^{28}$	$25 \text{nb}^{-1}$
$p\uparrow-p\uparrow^*$	111	175	1.0	20-25	$60 \times 10^{30}$	$40 \times 10^{30}$	$14 \text{pb}^{-1}$

All numbers are given for operation at an energy of 100 GeV/n.

The RHIC also aims to run at  $\sqrt{s} = 500 \text{ GeV}$  polarized pp interactions. The luminosities quoted above are planned to be enhance to the following values:

$L_{\text{store avg}} = 8 \times 10^{26} \text{ cm}^{-2}\text{s}^{-1}$  for Au-Au at 100 GeV/n ( $4 \times$  design)

$L_{\text{store avg}} = 6 \times 10^{31} \text{ cm}^{-2}\text{s}^{-1}$  for p-p at 100 GeV,

Lstore avg =  $1.5 \times 10^{32} \text{ cm}^{-2} \text{ s}^{-1}$  for p-p at 250 GeV (16× design) both with 70% polarization

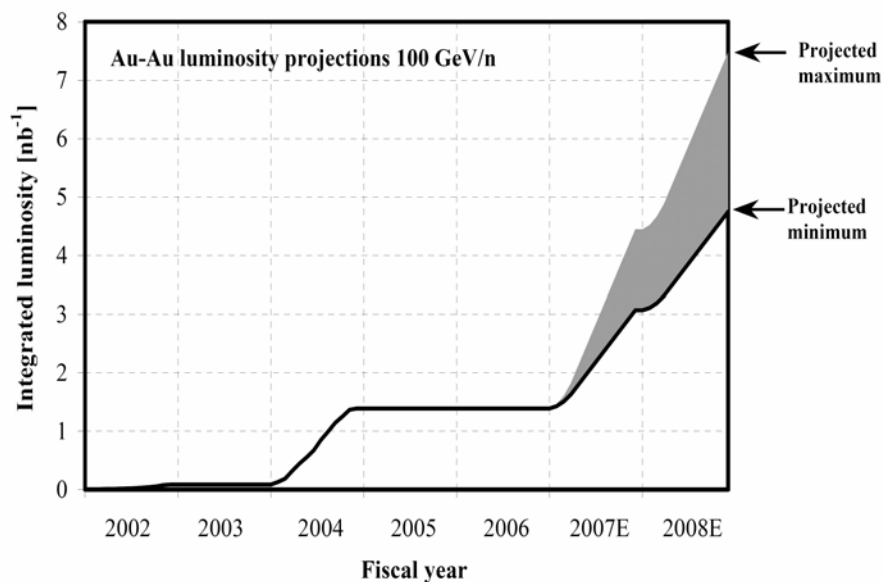


Figure 51 Minimum and maximum projected integrated luminosity for Au-Au collisions [56].

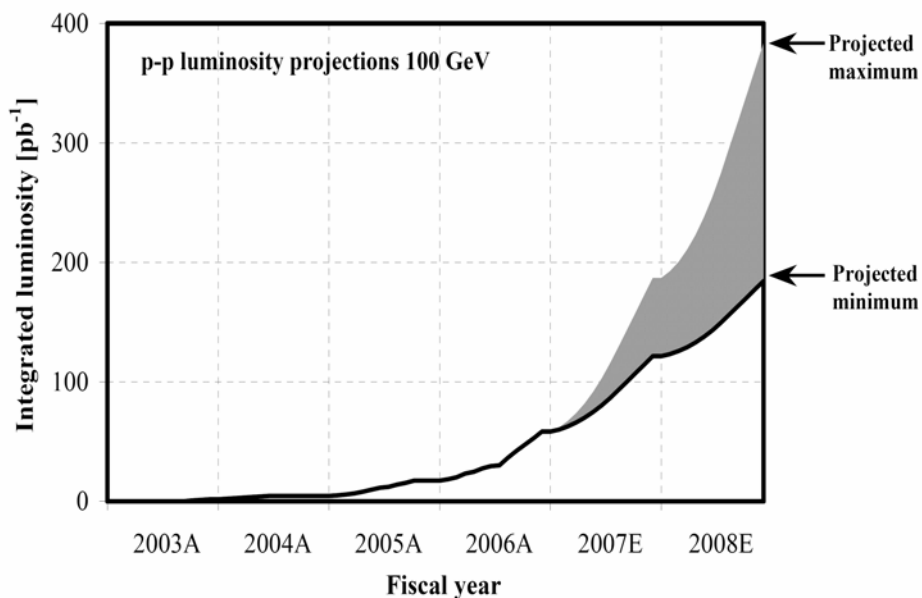


Figure 52 Minimum and maximum projected integrated luminosity for p-p collisions [56].

Figure 51 and 52 show expected minimum and maximum projected integrated luminosities at RHIC for AuAu and pp interactions, respectively. Our detector has a geometrical efficiency of 0.5%. We have calculated upper limits for magnetic monopole production with this efficiency and also with maximum efficiency (after detector upgrade), which we consider to be 50%, using the expected RHIC luminosities.

The cross section limit at 95% confidence level, when no magnetic monopole candidates is expressed as  $\sigma < 3.0/(\epsilon \text{ Ldt})$ , where  $\epsilon$  is the detection efficiency and Ldt the integrated luminosity. According to Figure 52 the projected minimum of delivered pp integrated luminosity is  $\sim 180 \text{ pb}^{-1}$  and the projected maximum is  $380 \text{ pb}^{-1}$ . We used in our calculations the average between those two values which is  $280 \text{ pb}^{-1}$ . The limit for the cross section in pp interactions that can be obtained with 250 GeV energy option is based on following numbers: luminosity of  $1.5 \times 10^{32} \text{ cm}^{-2}\text{s}^{-1}$ , one year ( $10^7 \text{ s}$ ) RHIC operation. This will correspond to :  $1.5 \times 10^{32} \text{ cm}^{-2}\text{s}^{-1} \times 10^7 \text{ s} = 1500 \text{ pb}^{-1}$ . The Table XV below presents expected magnetic monopole production cross section limits with different efficiencies and integrated luminosities in pp interactions at RHIC. We also included LHC expected limits for 0.5 efficiencies with 3 expected LHC luminosities:  $5 \times 10^{32} \text{ cm}^{-2}\text{s}^{-1}$  (At the beginning of the LHC operation),  $1 \times 10^{34} \text{ cm}^{-2}\text{s}^{-1}$  (normal LHC operation) and  $1 \times 10^{35} \text{ cm}^{-2}\text{s}^{-1}$  (LHC Upgrade plan). We are assuming one year ( $10^7 \text{ s}$ ) operation for each luminosity.

Table XV. Expected production cross section limits for the magnetic monopole at RHIC and LHC in pp interactions.

Energy	Ldt ( pb <sup>-1</sup> )	$\epsilon$	$\sigma$ (pb)	$\sigma$ (pb)
100	280	0.005	2.1	
100	280	0.5	0.021	
250	1500	0.005	0.4	
250	1500	0.5	0.004	
14000	1500	0.5	0.0012	$1.2 \times 10^{-39} \text{ cm}^2$
1400	1500	0.5	0.00006	$6.0 \times 10^{-41} \text{ cm}^2$
1400	1500	0.5	0.00006	$6.0 \times 10^{-42} \text{ cm}^2$

We can also estimate the same numbers for the AuAu interactions at RHIC (100 GeV/nucleon) and at LHC (Lead-Lead at 5.5 TeV/nucleon). For RHIC we assumed a projected luminosity of  $6 \times 10^{26} \text{ cm}^{-2}\text{s}^{-1}$  (average between maximum and minimum values see Figure 51) and for LHC, a luminosity of  $1 \times 10^{27} \text{ cm}^{-2}\text{s}^{-1}$  [57] and one year operation time. To calculate these numbers for heavy ions we use the expected  $Z^4$  enhancement [58] of the cross sections in heavy ion interactions. This enhancement in case of AuAu is  $79^4 = 3.895 \times 10^7$  and for PbPb  $82^4 = 4.521 \times 10^7$ .

Table XVI. Expected production cross section limits for the magnetic monopole at RHIC AuAu and LHC in PbPb interactions.

Energy	Ldt ( pb <sup>-1</sup> )	$\epsilon$	$\sigma$ (pb)	$\sigma$ (pb)
100	6	0.005	100000	
100	6	0.5	1000	
100	6	0.005	0.0026	$2.6 \times 10^{-39} \text{ cm}^2$
100	6	0.5	0.000026	$2.6 \times 10^{-41} \text{ cm}^2$
5500	10	0.5	0.00013	$1.3 \times 10^{-41} \text{ cm}^2$

We should point out that in the case of heavy ion collisions with  $Z^4$  enhancement, the obtained cross sections rise rapidly with the monopole mass, because the intensity of the  $\gamma\gamma$  interactions, which are responsible for monopole production, falls rapidly with the produced particle mass [59].

Figures 53 and 54 shows  $\gamma\gamma$  luminosity functions [59a], with the a number of  $\gamma\gamma$  interactions dependent on the mass of the produced system for RHIC AuAu interactions at 100 GeV per nucleon and for LHC PbPb interactions at 5.5 TeV per nucleon, respectively.

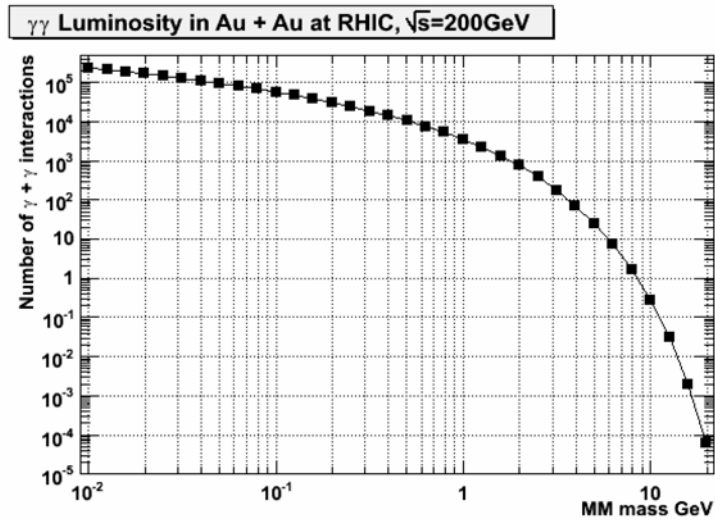


Figure 53. The luminosity function at RHIC for Gold-Gold interactions [59a].

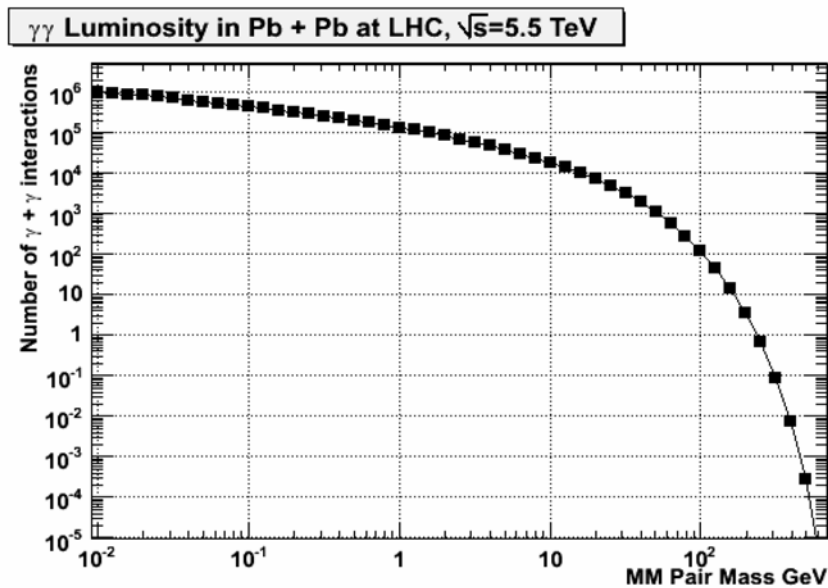


Figure 54. The luminosity function at LHC for Lead-Lead interactions [59a].

We will return to the monopole production cross section in heavy ion collisions. Now we will discuss the monopole production in pp interactions. As we mentioned earlier in our overview, due to the high coupling constant of the magnetic monopole, there is no way

for perturbative calculations to work for magnetic monopole cross section estimates. Instead a Drell-Yan mechanism [60] is used for the cross section calculation. Figure 55 shows a Feynman diagram of the Drell-Yan mechanism for dimuons and monopole-antimonopole production.

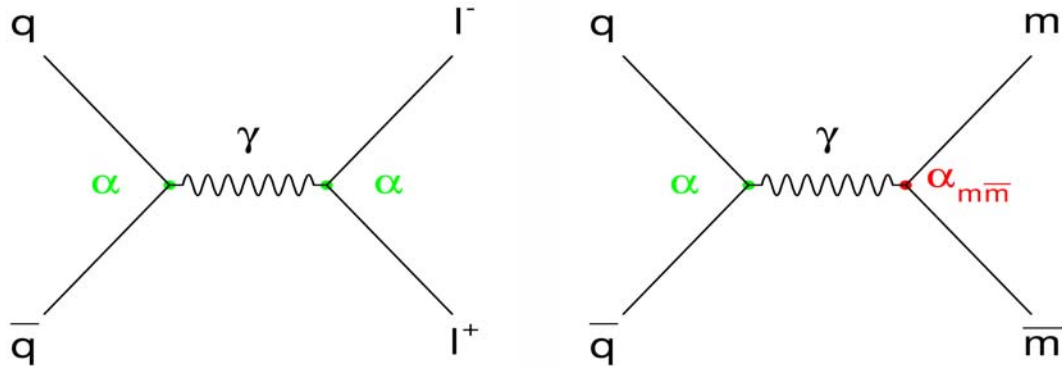


Figure 55. Drell-Yan process for dimuons (left) and monopole-antimonopole pair (right).

These two diagrams show annihilation of the quark-antiquark via the intermediate virtual photon and later photon decay into the two leptons (left) and monopole-antimonopole pair (right). This simple production mechanism allows qualitative cross section estimates in the absence of a reasonable field formulation of monopole production. The Drell-Yan cross section depends on strong interaction between the initial pair of quarks. In the high energy limit, the quarks are treated like free charged particles and their interaction is purely electromagnetic. This is a very good approximation for reasonably high energies  $E \gg m_q$ , where  $E$  is the total energy of the incident particles in the center of mass system. The cross section  $\sigma(q\bar{q} \rightarrow l^+l^-)$  is related to  $\sigma(e^+e^- \rightarrow \mu^+\mu^-)$ , which is given by:  $\sigma(e^+e^- \rightarrow \mu^+\mu^-) = 4\pi\alpha^2/3E_{cm}^2$ ,  $E \gg m_\mu$ . The electron charge  $e$  is replaced by the quark charge  $Q|e|$  and all possible color orientations of the quark are averaged  $\sigma(q\bar{q} \rightarrow l^+l^-) = Q^2/3 \times 4\pi\alpha^2/3E_{cm}^2$ . This is the underlying interaction for the process  $p\bar{p} \rightarrow l^+l^-$ . The complete cross section calculation takes into account the quark structure of the proton and antiproton [61], but we are not presenting it here. The last equation requires some corrections but will have the same dependence on the coupling constant  $\alpha$ . We can use this equation to calculate the production of magnetic monopoles. The proper coupling of the magnetic charge to the electromagnetic field has to be incorporated. It is derived by combining the Dirac Quantization Condition with the definition of the coupling constant  $\alpha \sim e^2$ :  $\alpha_{mm} = ng/e \times \alpha$ , which gives for the cross section  $\sigma(q\bar{q} \rightarrow m^+m^-) = (ng/e)^2 \times \sigma(q\bar{q} \rightarrow l^+l^-)$ . This means that Drell-Yan process cross sections are scaled by a factor  $(g/e)^2 = 4692$  at  $n = 1$  in order to get the monopole pair production cross section. The Drell-Yan pair production cross section for the RHIC and LHC energies were studied in Ref [62]. The authors give cross section versus dilepton mass plots and tables. The mass range which they studied is limited to 20 – 80 GeV for different processes. We in our study are projecting wider mass regions, and therefore we searched alternative information in the literature and found interesting prediction in Moedal Project [53]. The authors expressed expected magnetic monopole production cross sections by the formula:

$\sigma(M) = (68.5)2 \times 1.74/s \times e^{-25.3m/\sqrt{s}} \times 10^{-30}$ , where  $M$  is the monopole mass and  $s$  the available cms energy. We plotted this formula for RHIC energies at 200 GeV and 500 GeV, FNAL energy of 1.96 TeV and LHC energy of 14 TeV for  $p\bar{p}$  or  $p\bar{p}$  interactions and the results are shown in Figure 56.

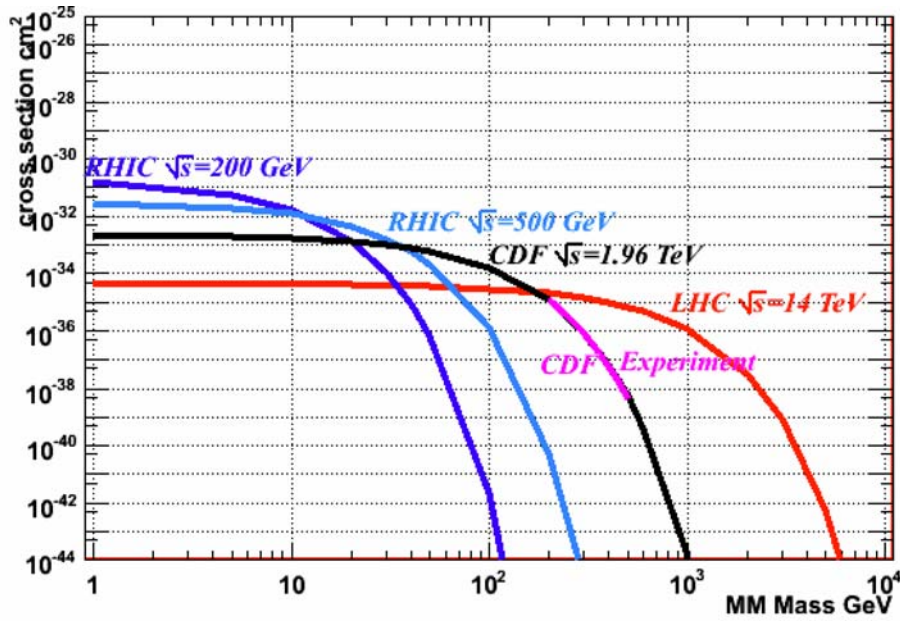


Figure 56. Drell-Yan cross section versus mass for magnetic monopoles for RHIC energies of 200 GeV and 500 GeV, FNAL energy of 1.96 GeV and LHC energy of 14 GeV.

In Figure 56 the dark blue curve corresponds to the Drell-Yan production cross section versus the monopole mass for the RHIC energy of 200 GeV, the light blue for RHIC 500 GeV, the black curve for FNAL energy of 1.96 GeV and the red curve for LHC energy of 14 TeV. The mass interval for which we are plotting the curves is between 1 GeV 10 TeV. We find excellent agreement with the Drell-Yan curve for the mass interval of 200 to 600 GeV (see Figure 43) published by the authors of the FNAL CDF experiment [34]. This curve is presented on the Figure 56 in pink color. The above mentioned formula fits very well with the FNAL data [34]. The Moedal Project estimates their expected performance based on that curve. After having such curves for each energy domain, one can compare the obtained cross section limits with the Drell-Yan mechanism.

Figure 57 shows such a comparison for RHIC energies of 200 GeV and 500 GeV (blue and black curve respectively). The lines correspond to the calculations performed above for 200 GeV and 500 GeV energies for two efficiencies: 0.005 (current Project value for the detector efficiency) and 0.5 – efficiency which might be achievable in case of detector upgrade. The lines for 200 GeV are in red and for 500 GeV in blue. For 200 GeV a theoretical curve is crossed at 50 GeV/c<sup>2</sup> monopole mass when efficiency is 0.005 and at 70 GeV/c<sup>2</sup> when the efficiency is 0.5. This means that at the cross section limit of  $2.1 \times 10^{-36} \text{ cm}^2$  ( $\epsilon=0.005$ ) we would see at least 1 Monopole up to mass 50 GeV (and more if the magnetic monopole mass is lower). For the ( $\epsilon=0.5$ ) efficiency this limit goes up to the 70 GeV for the cross section limit of  $2.1 \times 10^{-36} \text{ cm}^2$ . In case of 500 GeV energy the corresponding limits are 110 and 160 GeV with the efficiencies of 0.005 and 0.5 and cross sections  $4 \times 10^{-37} \text{ cm}^2$  and  $4 \times 10^{-39} \text{ cm}^2$ , respectively.

**RHIC pp DY and  $\sigma$  limits**

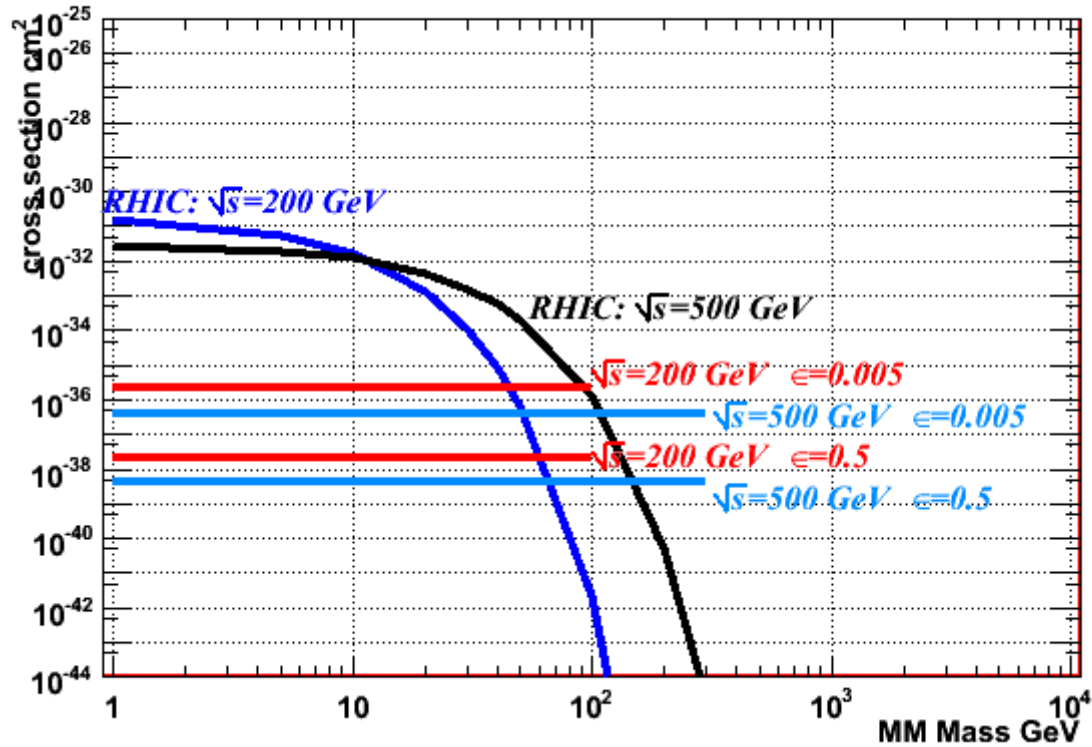


Figure 57. Drell-Yan cross section curves for pp interactions at RHIC 200 GeV, 500 GeV, FNAL 1.96 GeV and LHC 14 TeV.

Figure 58 shows same plot as Figure 57 for the pp interactions at the LHC energy of 14 TeV. The red curve corresponds to the predicted Drell Yan process cross sections and the three lines are our calculated cross sections for the detector efficiency of 0.5 and three expected LHC luminosities of  $5 \times 10^{32} \text{ cm}^{-2}\text{s}^{-1}$  (At the beginning of the LHC operation),  $1 \times 10^{34} \text{ cm}^{-2}\text{s}^{-1}$  (normal LHC operation) and  $1 \times 10^{35} \text{ cm}^{-2}\text{s}^{-1}$  (LHC Upgrade plan). With the LHC normal operation mode we would be able to see one magnetic monopole of 4 TeV mass with a production cross section of  $6.0 \times 10^{-42} \text{ cm}^2$ .

Figure 59 shows similar plots as above Figure 57 and 58, but for RHIC energies of 100 GeV/nucleon in gold gold interactions. Predicted curve of the Drell-Yann process was modified by a factor of 231 taking into account the number collisions in Au+Au interactions predicted in Ref [62]. We plotted expected cross sections the same way as we did before. Corresponding cross section limits are at the  $1.0 \times 10^{-31} \text{ cm}^2$  and  $1.0 \times 10^{-33} \text{ cm}^2$  level. If we take into account the  $Z^4$  enhancement of the production cross section we mentioned above and also the luminosity function for RHIC (see figure 53), we will have two curves for the two detection efficiencies – a black curve for efficiency=0.005 and blue curve for efficiency = 0.5.

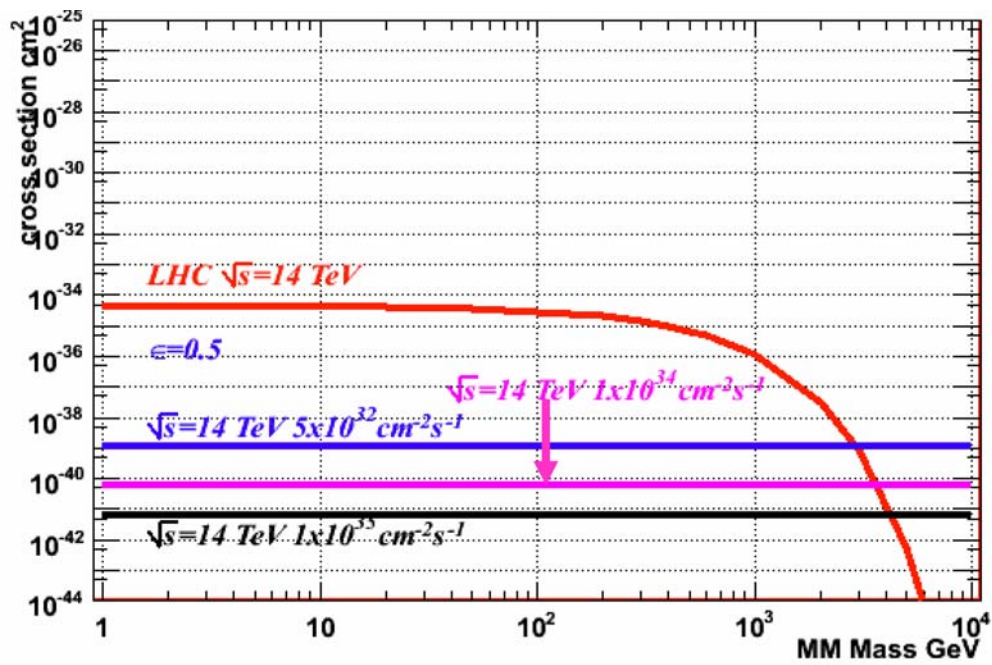


Figure 58. Drell-Yan cross section curves for LHC at 14 TeV and corresponding predicted cross sections in pp interactions.

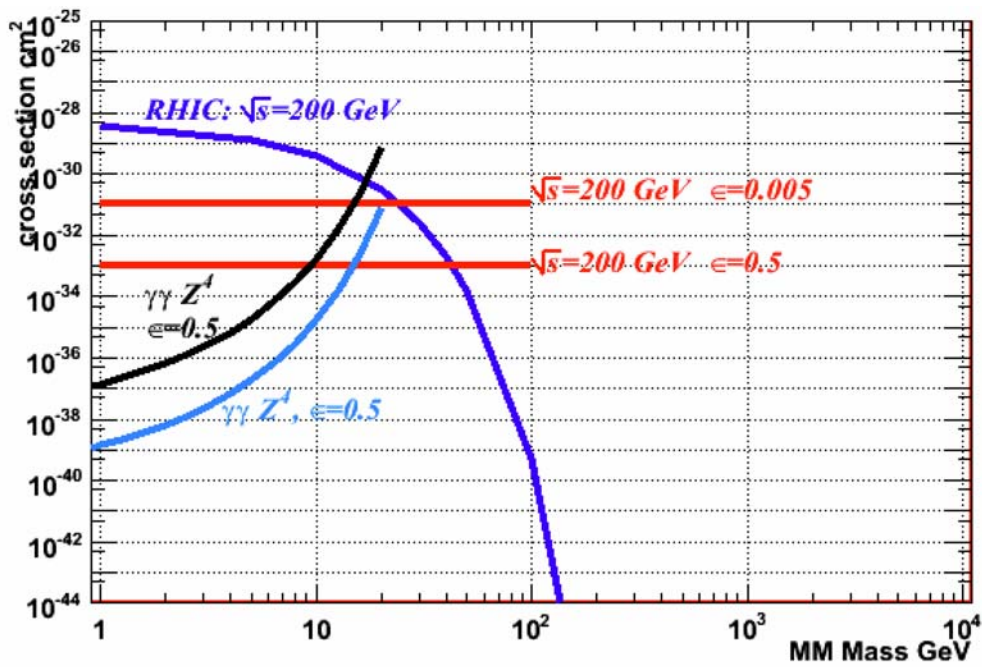


Figure 59. Drell-Yan cross section curves for RHIC at 100 GeV/nucleon energy and corresponding predicted cross sections in AuAu interactions.

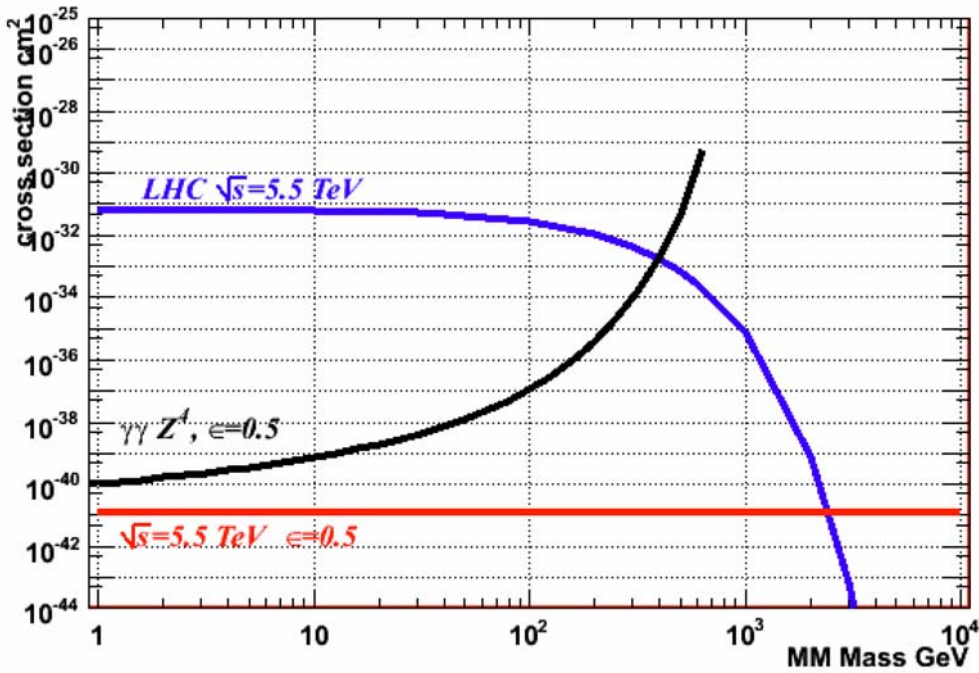


Figure 60. Drell-Yan cross section curves for LHC at 5.5 TeV/nucleon energy and corresponding predicted cross sections in PbPb interactions.

Figure 60 shows similar plots for the expected Drell-Yan Process at LHC energies for the PbPb interactions. The corresponding modification factor was calculated based on results provided in Ref. [63] and [64]. Here only the 0.5 efficiency was considered. The blue curve is a Drell-Yan curve, the red line corresponds to the expected cross section, and the black curve shows the  $Z^4$  enhancement of the production cross section. The cross section limit of  $6 \times 10^{-34} \text{ cm}^2$  could be achieved. For the  $\gamma\gamma$  interactions cross sections ranges between  $1 \times 10^{-40} \text{ cm}^2$  and  $1 \times 10^{-39} \text{ cm}^2$ , and reach  $1 \times 10^{-37} \text{ cm}^2$  at 100 GeV.

Figure 61 shows again a plot which was presented on Figure 7, a classical Dirac magnetic monopole cross section upper limits versus magnetic monopole mass obtained in different experiments we discussed in this article. We added expected cross sections at RHIC in pp interactions at 500 GeV center of mass energy for one efficiency: 0.5 ( $\sigma \sim 4 \times 10^{-39} \text{ cm}^2$ ), red line, and also expected cross section in AuAu interaction with the  $Z^4$  enhancement of the heavy ion interactions (pink curve). Expected RHIC result for 250 GeV energy proton beam experiment with 0.5 efficiency can reach a limit which is at the level or better than direct search experiments and mass coverage up to  $\sim 250 \text{ GeV}/c^2$ . Same time in the AuAu interactions monopole production cross section can be achieved better or compatible with direct search experiments in the mass region up to  $5 \text{ GeV}/c^2$ .

In conclusion we would like to thank Drs. A. Baltz, D. Kharzeev and W. Marciano, of BNL for fruitful discussions and Dr. A. Baltz for calculation  $\gamma\gamma$  luminosity functions for heavy ion interactions at RHIC (AuAu) and LHC (PbPb) energies.

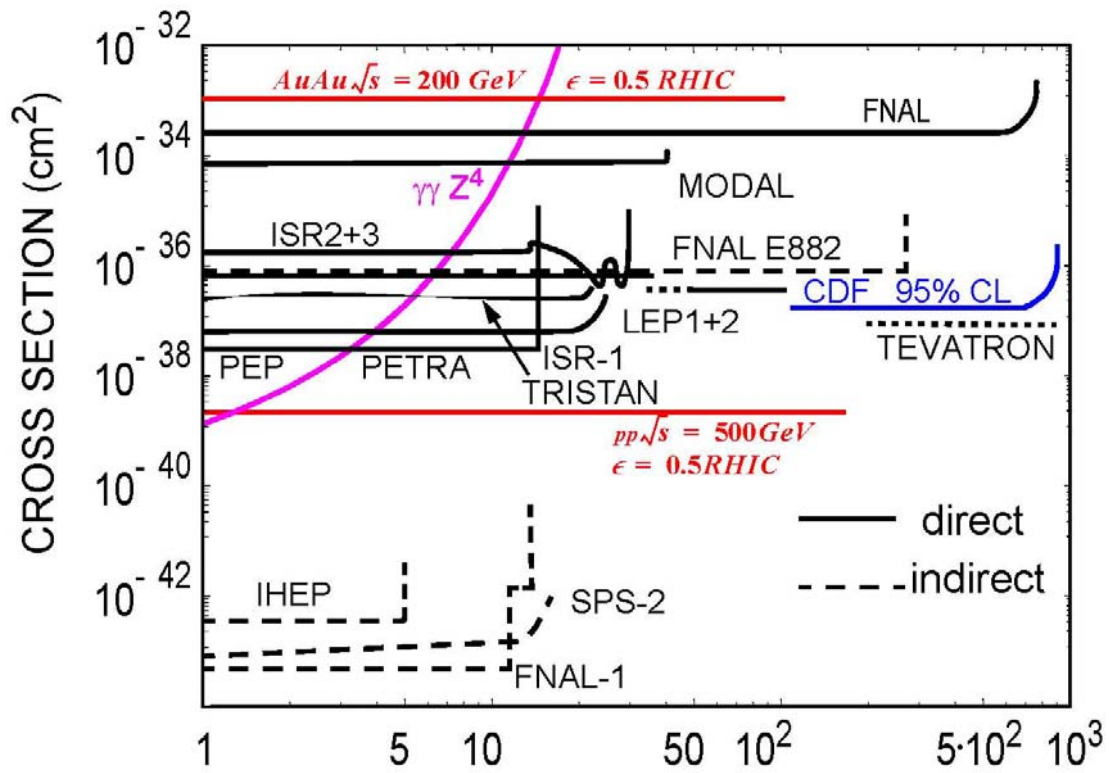


Figure 61. Classical Dirac magnetic monopole cross section upper limits versus magnetic monopole mass obtained from direct accelerator searches (solid lines) and indirect searches (dashed lines) with RHIC projected cross sections.

## References

- [1] Pierre de Maricourt, On the Magnet, letter to Siger de Foucaucourt, (1269). In The Letter of Petrus Peregrinus on the Magnet, New York, 1904. McGraw-Hill. Translated by Brother Arnold.
- [2] P. Curie, On the possible existence of magnetic conductivity and free magnetism. Seances Soc. Phys. (Paris), 76 (1894).
- [3] P.L.M. Dirac, Proc. Roy. Soc. A133, 60 (1934).
- [4] J. C. Maxwell "A Treatise on Electricity and Magnetism", Oxford Classic Text in Physical Sciences (1873)
- [5] S. Eidelman et al. (PDG Collab.), Phys. Lett. B 592, 33, 67 (2004)
- [6] L.J. Schwinger, Phys. Rev. D12, 3105 (1975)
- [7] G. 't Hooft, Nucl. Phys. B 79, 276 (1974).
- [8] M. Polyakov, JETP Letters 20, 430 (1974).
- [9] K.R. Gienes, E. Dudas and T. Gherghetta Phys. Rev. B 436, 55 (1998).
- [10] V.A. Rubakov, UFN 171, 913 (2001)[in Russian].
- [11] T. Banks et al., Phys. Lett. B212, 45 (1988)
- [12] G. Giacomelli and L. Patrizi, hep-ex/0506014 and hep-ex/0302011
- [13] S. Manzoor et al., e-Print Archive: physics/0611278
- [14] H. Bradner and W. M. Isbell, Phys. Rev. 114, 603 (1959)
- [15] E.M. Purcel et al, Phys. Rev.129, 2326 (1963)
- [15a] M. Fidecaro et al, Il Nuovo Cim., XXII, 657, (1961)
- [15b] E. Amaldi et al, Il Nuovo Cim., XXVIII, 773, (1963)
- [16] I.I. Gurevich . et al., Phys. Lett. 38B, 549 (1972)
- [16a] I.I. Gurevich et al., Phys. Lett., 31B, 394 (1970)
- [16b] E. Goto et al., Phys. Rev. 132, 387 (1963)
- [16c] E. Amaldi et al., CERN 63-13 (preprint) 1963
- [17] P.H. Eberhard et al., Phys. Rev.D11, 3099 (1975)
- [17a] R.A. Carrigan et al., Phys. Rev.D11, 3867 (1974)
- [17b] D.L. Burke et al., Phys. Lett. 60B, 113 (1975)
- [17c] V.P. Zrelov et al., Phys. Cz. Jour. Phys., B26, 1306 (1976)
- [17d] R.A. Carrigan et al., Phys. Rev.D17, 1754 (1978)
- [18] J.M. Barkov et al., CERN/EP83-194 (preprint) (1983)
- [18a] P.B. Price et al., Phys.Rev.Lett., 59, 2523 (1987)
- [18b] T. Gentile et al., Phys. Rev. D, 35, 1081 (1987)
- [18c] K. Kinoshita et al., Phys. Rev. Lett., 60, 1610(1988)
- [18d] Y.D. He., Phys. Rev. Lett, 79, 3134 (1997)
- [19] G.R. Kalbfleisch. et al., Phys. Rev. Lett. 85, 5292 (2000)
- [19a] F. Abe *et al.*, Phys. Rev. D 49, R1 (1994)
- [19b] B. Abbott *et al.*, Phys. Rev. Lett. 82, 4769 (1999).
- [20] G.R. Kalbfleisch. et al., Phys. Rev. D.69 (2004)
- [20a] W. Luo, Ph.D. thesis, University of Oklahoma, 2002, UMI-30-56946 (AAT 3056946)
- [20b] S. Abachi *et al.*, Nucl. Instrum. Methods Phys. Res. A 338, 185 (1994).
- [20c] F. Bedeachi *et al.*, Nucl. Instrum. Methods Phys. Res. A 268,50 (1988)
- [20d] R.R. Ross, P.H. Eberhard, L.W. Alvarez, and R.D. Watt, Phys.Rev. D 8, 698 (1973)

- [21] L.Gamberg, G.R.Kalbfleisch, K.A.Milton, *Found.Phys*, 30,543 (2000)
- [22] A. Aktas et al., *The European Physics Journal*, C 41, 133 (2005)
- [22a] URL: <http://www.2genterprises.com>
- [22b] A. Pukhov et al., arXiv:hep-ph/9908288
- [23] M. Bertani et al, *Europhys. Lett.* 12, 613 (1990)
- [24] M.J Price., in *Monopole '83* edited by J.L. Stone, NATO Advanced Study Institute Series B, Physics, Vol. 111, Plenum, New York, 1983, p.621]
- [25] G. Giacomelli. et al, *Il Nuovo Cimento* 28, 212 (1975)
- [26] M. Hoffmann et al, *Letter Al Nuovo Cimento* 23, 357 (1978)
- [27] K. Kinoshita et al, *Phy. Rev. Lett.* 48, 77 (1982)
- [28] D. Fryberger et al., *Phy. Rev. D* 29, 1524 (1984)
- [29] P. Musset et al., *Phy. Lett.* 128B, 333 (1983)
- [29a] S.P. Ahlen, *Phys. Rev. D* 17, 229 (1978); S. P. Ahlen and K. Kinoshita, *Phys. Rev. D* 26, 2342 (1982)
- [30] K. Kinoshita et al., *Phy. Rev. Lett.* 60, 1610 (1988)
- [31] K. Kinoshita et al., *Phy. Lett. B*, 228, 543 (1989)
- [31a] R.A. Carrigan Jr., F.A. Nezrick and B.P. Strauss, *Phys. Rev. D* 8, 3717 (1973); D. Fryberger, T. Coan, K. Kinoshita and P.B. Price, *Phys. Rev. D* 29, 1524 (1984); B. Aubert, P. Musset, M. Price and J.P. Vialle, *Phys. Lett. B* 120, 465 (1983)
- [31b] R.R. Ross, P.H. Eberhard, L.W. Alvarez and R.D. Watt, *Phys. Rev. D* 8, 698 (1973)
- [32] K. Kinoshita et al., *Phy. Rev. D* 46, R881 (1992)
- [32a] R.L. Fleischer Et al., *Nuclear Tracks in Solid* (University of California Press, Berkeley, (1975)
- [33] J.L. Pinfold et al., *Phys. Lett. B*, 316, 407 (1993)
- [33a] A.K. Drukier and S. Nussinov, *Phys. Rev. Lett.* 49, 102 (1982)
- [33b] G. Giacomelli, Talk at the University of Bologna (2006)
- [34] A. Abulencia et al., *Phys. Rev. Lett.* 96, 201801 (2006)
- [34a] G. Bauer *et al.*, *Nucl. Instrum. Methods Phys. Res., Sect. A* 545, 503 (2005).
- [34b] S. P. Ahlen, *Phys. Rev. D* 17, 229 (1978)
- [35] Graf S et al, *Physics Letters*, 262B, 463 (1991)
- [35a] A.I. Studenkin. *Sov. J. Part. Nucl.* 21, 259 (1990)
- [35b] E. Picasso NATO Advanced Study Institute, Dr. B, Physics, 80, 441 (1981).
- [36] G.W. Bennett Et al., *Physics review*, D, 73, 072003-1 (2006)
- [37] M. Acciarri *et al Phys. Lett. B* 345 609 (1995)
- [38] A. De Rujula *Nuclear Physics*, B435 257 (1995)
- [39] I.F. Ginzburg and S.L. Panfil *Sov. J. Nucl. Phys.* 36 850 (1982)
- [40] I.F. Ginzburg and A. Schiller *Phys. Rev. D* 57 6599–603 (1998)
- [41] I.F. Ginzburg and A. Schiller *Phys. Rev. D* 60 075016 (1999)
- [42] B. Abbott et al., *Phys. Rev. Lett.* 81 524 (1998)
- [43] K.A. Milton *Rep. Prog. Phys.* 69 1637–1711 (2006)
- [44] W. Heisenberg W and H.Z. Euler *Phys.* 98 714–32 (1936)
- [45] V. Weisskopf, *Mat. Fys. Medd* 14 no.6 (1936)
- [46] J. Schwinger *Phys. Rev.* 82 664(1951)
- [47] J. Schwinger *Particles, Sources, and Fields* vol 2 (New York: Addison-Wesley, republished by Perseus Books) (1973)
- [48] M. Bordag and Lindig *J. Phys. Rev. D* 58 045003 (1998)
- [49] M. Bordag and Robaschik *D. Ann. Phys. (N.Y.)* 165 192 (1985)
- [50] V.I. Ritus, *Pisma Zh. Eksp. Teor. Fiz.* 69 1517–36 (1975);

- Sov. Phys.—JETP* 42 774 (1975)
- [51] M. Reuter Schmidt M.G. and Schubert C *Ann. Phys. (N.Y.)* 259 313–65 (1997)
  - [52] D. Fliegner et al., *Theor. Math. Phys.* 113 289–300 (1997);  
Fiegner D. et al., *Theor. Math. Phys.* 113 1442 (1997)
  - [53] J.L Pinfeld et al., <http://moedal.web.cern.ch/moedal>
  - [54] <http://lhc.web.cern.ch/lhc/>
  - [55] [http://www.bnl.gov/npp/docs/pac0906/chaudhari\\_Monopole-RHIC-PAC.pdf](http://www.bnl.gov/npp/docs/pac0906/chaudhari_Monopole-RHIC-PAC.pdf)
  - [56] <http://www.agrhichome.bnl.gov/RHIC/Runs/RhicProjections.pdf>
  - [57] J. Jowett, [http://paf.web.cern.ch/paf/Presentations/Hi\\_in\\_LHC\\_JJowett\\_Oct2006\\_v2.pdf](http://paf.web.cern.ch/paf/Presentations/Hi_in_LHC_JJowett_Oct2006_v2.pdf)
  - [58] G. Baur, e-Print Archive: hep-ph/0112239 (2001)
  - [59] A.J. Baltz and M. Strikman, *Phys.Rev. D*, 57, 548 (1998)
  - [59a] A.J. Baltz, private communication.
  - [60] I.R. Kenyon, *Rep. Prog. Phys.*, Vol. 45, 1982.
  - [61] M.E. Peskin, D.V. Schroder, *An introduction to Quantum Field theory*, Reading, MA: Perseus Books (1995)
  - [62] S. Gavin et al., *Int.J.Mod.Phys.A*10:2961-2998, (1995)
  - [63] D. Kharzeev et al., *nucl-th/0012025*, (2000)
  - [64] D. Kharzeev et al., *Nuclear Physics A* 747, 609 (2005)